Final Report
of
Experimental and Theoretical Investigations
on
Ocean Sonic Boom Propagation

Prepared for:

Missile Defense Agency (MDA)
Office of Secretary of Defense
Pentagon

Headquarters Space and Missile System Center (SMC)
Los Angeles Air Force Base, CA

Institute for Environment, Safety and Occupational Health Risk Analysis (IERA)
Brooks Air Force Base, TX

PARSONS
Pasadena, CA

Under Parsons Subcontract to HKC Research
738249, 3000-02

September 2001

By

HKC Research
2335 Westridge Road
Los Angeles, CA90049-1228
(310) 472-3619/ (213) 740-5365
Fax: (213) 740-7774
<e-mail: cheng@spock.usc.edu>

Principal Investigator
Hsien K. Cheng

Date: April. 30, 2002

Firm Proprietor
Hsien K. Cheng

Date: April. 30, 2002

Executive Summary

The draft Final Report in its original form has received various comments and recommendations from colleagues and program sponsors since its completion on September 11, 2001. Except the very few comments which may have based on some concept inapplicable to the problem considered, most suggestions are accepted and proven to be helpful in eradicating numerous typographical and transcribing errors, as well as clarifying several important statements in the report. Among sponsors' specific recommendations are the additions of an Executive Summary and also statements for each section indicating the need for the subject research towards reducing the environmental impact of the space-launch and other flight operations. Brief statements in small-italics font are thus added at the beginning of most sub-sections, where expositions of analyses and examples detailed in the text may appear to be lengthy and confusing to a non-specialist. Summary statements are not added, however, to each of the five main sections, since the significance of the collective research to marine impact study have already been high-lighted by the head of each main section. Together with an Executive Summary written for the less technically-oriented readers, it is concurred that these brief statements or descriptions may help reaching a wider circle of audience.

Recent analysis by Cheng and Lee has shown that disturbances from acoustic sources produced by interaction of a surface wave train with an incident sonic boom wave will attenuate in deep water at a rate much lower (slower) than those predicted by Sawyers' theory for a flat (non-wavy) ocean, and will accordingly overwhelm the latter at large depth. Experimental and theoretical research on underwater impact from sonic booms are performed to ascertain the significant influence of wavy ocean surface on sonic boom's penetration power, and to determine, through application of the validated model to aircraft and space-launch examples, if predicted signal intensity and characteristics at depth belong to the ranges and types that may allow meaningful impact assessment in marine mammal study.

To ascertain the important difference in underwater sonic boom response between wavy and non-wavy surfaces and the cylindrical-spreading rule underlying deep-water attenuation rate in the Cheng-Lee theory, laboratory experiment was set up to record over-pressure in a small, 3-meter long, water-filled tank during overflight of a supersonic projectile. Microphone driven wave makers were used to generate trains of surface gravity waves; sensor arrays utilizing Kistler piezotrons with electronics and computer-interface support were employed to record wave-form at different depth levels; the laboratory set-up and procedures are detailed in Sec. 4 and Attachment II. A number of obstacles in measurement encountered, including the effect of the muzzle blast, persistent anomalous signals, and the non-uniformity in the surface wave train, were overcome and resolved. In spite of limitations in the laboratory set-up, the significant wavy-surface effects on underwater response to sonic boom, and the cylindrical-spreading rule are well confirmed in accord to the theory; in addition, the extensively collected wave-forms reveals wave-packet behavior and their dependence on surface wave length and surface wave slope, which are again in agreement with the theory.

Having validated the surface-wave interaction model, the method was applied to determine over-pressure wave-forms underwater for generic examples of aircraft supersonic over-flight at different depth levels, Mach numbers, surface wave numbers, and conditions corresponding to surface wave trains propagating in directions oblique to the flight track. The method was similarly applied to an example of

rocket space launch, using the Focus-Boom type sea-level signature (recorded during a Titan IV ascent) as an input, assuming two distinctly different surface-wave numbers. These examples, discussed in detail in Sec.3.6-3.8 and 3.10, broadly indicate that infra-sound of frequency 10-40 Hz originated from the transmitted sonic boom can reach down to 50-500 meters below sea surface at sound pressure level of 100-130 dB (re 1 μPa), corresponding to 0.002-0.209 pound per square foot depending on specific depth levels. Infrasound at these sound pressure levels is common in records of baleen whale calls and can be expected to be audible or perceived by these marine mammals. Another noticeable feature of the predicted waveforms is the frequency down-shift in the tonal pitch that reduces towards the end of the signal, which is also commonly found with the individual pulse in call records. Unlike the repetitive short pulses in the records, however, the duration of the underwater wave packet produced by a sonic boom will be rather long, according to results of the study. At one km below the surface, or deeper, this duration can be 3-5 seconds for an aircraft supersonic flight and will be 20-40 seconds in the case of a rocket space launch. (The 20-40 seconds in the latter case presents an area underwater affected by the sound pulse extending over a distance 7-14 km horizontally.) Understanding submarine animals' response to infrasound of this nature must therefore be central to the next phase of studies on impact to marine mammals.

Furthermore, results at the 50 m depth examined indicate that the wavy-surface interaction effects on amplitude and wave-form may not be altogether ignored even at locations not far from the surface; therefore, analysis of wave field near the surface may yield vital data to help assessing potential harassment at the physiological level to a broader class of marine animals. Presence of the sea floor must be an important consideration in analyses for the shallow coastal water where the sonic boom impact is expected to be the most severe. A shallow-water model with a flat (non-wavy) surface under an incident N-wave is adopted to investigate its response to sonic booms; cases with rigid and elastic bottom surfaces are both analyzed. Whereas, in the presence of a rigid bottom, the over-pressure is expected to increase by an amount as large as the surface value in the case of a very shallow depth, calculations show that the sea-floor effect will remain small until the channel depth becomes as small as a half of the sea-level sonic-boom signature length. For a sea-floor with sediment properties resulting in a very low (slow) compressive-wave speed, examples studied confirm the existence of sonic-boom excited sediment-boundary waves.

Two unresolved discrepancies remain in current prediction methods of sonic booms above the water; they will significantly affect the reliability of underwater impact analyses. The first is the failure in predicting the surface signatures of Focus-Boom type from space-launch operations (except for the peak over-pressure). Extensive studies with current sonic boom codes as well as a CFD Euler program confirm the culprit to be the inadequate provision of near-field data corresponding to a lack of accurate description of the rocket plume shape. Resolving the latter is thus one of the specific tasks in future study. The second discrepancy is concerned with the propagation code break-down when and where a "super-boom" occurs. The latter can occur near the ground or sea level where the ambient sound speed becomes the same as, and higher than, the horizontal propagation speed of the incident sonic boom wave field. This type of wave field has been known to yield wave intensity much stronger than the typical sonic-boom strength elsewhere, and is thus called the Super-Boom. A CFD program based on the nonlinear Tricomi equation governing this type of wave problem was used to test its adequacy as a program amendment to the standard method and to study super-boom's wave intensification power. Applications to examples with incident waves of the Focus-Boom (Titan IV) type and the N-wave type confirm super-boom's intensification power for both types, and reveal also the feasibility for a new, linear approach to the problem as well as important features unrecognized by standard propagation methods.

Table of Contents

*Note: Hard copies of the original figures and appendices are available upon request at the Space and Missile Systems Center, Los Angeles Air Force Base, (310) 363-0934 /-0935, or HKC Research, 2335 Westridge Road, Los Angeles, CA 90049-1228, (213) 740-5365 / (310) 472-3619, email: cheg@spock.usc.edu

Summary

Theoretical and experimental research on sonic boom noise penetration into water was conducted under the Ocean Sonic Boom (OSB) Program to establish the hydro-acoustic model for underwater sound pressure predication in order to ascertain the importance of audibility and other issues on impact to marine animals in deep and shallow water. Under this program, laboratory experiment was set up to measure sonic boom generated underwater wave-field. In spite of limitations of the experimental design and moderate laboratory set-up, significant differences between wavy and non-wavy surface models and the dominance of the wavy-surface influence in deep water. are confirmed. Within the significant parameter ranges of the theory, the measurements substantiate the cylindrical-spreading rule governing the submarine sonic-boom pressure attenuation. In the parallel theoretical development, the analysis of sonic boom interaction with a sinusoidal surface-wave train is extended to non-aligned, non-sinusoidal and multiple surface-wave trains; their salient features and importance to the deepwater sound field are ascertained by examples in both computational and laboratory studies. Whereas, significant differences between sonic booms from aircraft and from rocket space launch have been identified, results have broadly indicated that the predicted infrasound at sound levels of 100-130 dB (re 1 uPa) can reach depths of 50-1000 m and should be audible to many baleen whale species. The tonal structure and the relatively long signal duration found among other wave-form properties have provided specific aspects for marine bio-acoustics research to follow. The inadequacy of current sonic boom propagation codes in predicting focus-boom signature is found to have resulted mainly from the incomplete prescription of near-field data over the rocket plume, and represent an aspect in need of amendment essential to underwater impact studies. As a CFD investigation supporting the OSB program, the problem of a “super-boom” occurring during a rocket space launch is analyzed numerically with in-put data inferred from a field-recorded signature of a focus boom; the results reveal how a focused sonic boom may be further amplified and modified before it reaches the sea level. Sonic boom impact under water of shallow depth is also investigated as a problem which may severely affect the coastal water environment. Included is an analysis of sediment boundary waves on the sea floor; the study confirms that, with suitable combination of flight Mach number and sediment elastic properties, these waves can be excited by a sonic boom.

Among the major computer soft-wares produced in the course of this investigation are the complete program listings in four files developed for the most general (non-N waves) case in deepwater and the superboom CFD programs, included in Appendices I and II, respectively.

Attached are two major documents: (1) Technical report on the theory extension and applications (USC AME report 4-4-2001), and (2) Technical report on laboratory underwater experiment (USC AME Report 9-11-2001), in which much detailed descriptions, analyses and records are documented.

1. Introduction

This report presents results of experimental and theoretical investigations of sonic boom noise penetration into a wavy ocean and related problems under the support of a program initiated by US Air Force Material Command, Space & Missile Systems Center for Ballistic Missile Defense Organization, through Parsons Engineering Sciences Subcontract 738249, 3000-02 to HKC Research.

The following five sections of the main text present an overview on the basic and specific issues (Sec. 2)[*], model, code extensions and applications (Sec. 3), laboratory set-up and experiment (Sec. 4), space-launch related superboom problem (Sec. 5), and conclusions (Sec. 6). The main text is followed by figures and sketches referred to in the presentation, and two appendices of major computer program files (Appendices I, II). The content of this report is supplemented by Attachments I and II in which important technical details of the model and computational development and in the laboratory measurements and results are documented.

Two modifications in the research plan have been made in the course of the program development. One was replacing a part of laboratory study on sediment interaction by additional analyses on the theoretical models of sonic boom excited sediment waves in shallow water. This change results from realizing the lack of a definitive model and its dependence on sediment materials, which may not promise fruitful laboratory study within the allotted program resource. The other plan modification made more recently is re-directing laboratory effort to measurements in the original smaller tank, using the improved, new sensors, wave-makers and set-up, instead of the large (wider) tank. The decision was made upon the recognition that a great deal of knowledge and experience has been gained with the older tank with regard to maximizing the signal-to-noise ratio and other considerations. Most test objectives scheduled for the larger tank, such as the study of non-aligned wave trains, are being accomplished in the older tank. Tests in the larger tank will be conducted at the very end of the program to ascertain its usefulness and function for subsequent studies. These two program plan changes are reflected in the works reported in Sections 3 and 4.

[*] Portions of Sec. 2 on the overview and problem background are adopted from the original program proposal.

2. Overview: Basic and Specific Issues

Sonic boom noise has been recognized as an outstanding environmental impact issue of supersonic aircraft as well as space-launch operations [1-4]. Methods of predicting sonic-boom overpressure have evolved from classical ray-acoustics theory [5-7] and have been extensively used for sonic-boom impact assessment in many design and planning studies. [8-13] While several aspects of these predication methods/codes still require improvement, an important research development in recent years has been concerned with the potential effects of sonic booms on marine mammals and other forms of sea life [14-19]. Apart from studies of sonic boom effects on pinnipeds and turtles which were the focuses of laboratory and field experiments in Ref. [20-22], an adequate model for predicting sonic-boom generated disturbances underwater is yet to be ascertained and further improved before it can adequately serve as a scientific base for impact assessment on sea life.

Attention in this research area has focused mainly on the potential of causing physiological harm to the animals [20-22]. In this regard, it is important to quantify the propagation in air and water of sonic booms and to compare predictions and empirical measurements with established risk criteria for physiological and behavioral effects on animals. Even where risk of these effects are low or non-existent, such comparisons with clear explanation are necessary to forestall challenges based on speculation or conjecture of worst-case scenarios. Very mild physiological effects (such as that which causes temporary auditory threshold shift) are not considered to be injuries in the sense of tissue destruction or physiological threat, but may have detrimental behavioral consequences to animals in short and long terms. The legal definition of what constitutes a significant behavioral disruption—its degree and duration—is still in debate at this time. Regardless of the outcome, animal response to anthropogenic noise, including sonic booms, as well as acoustic communication in ambient and anthropogenic noise are issues that will play a part in that debate. Mild and intense man-made noise may impact adversely on their habitat preference, migration route choice and other ways of life as well as group behavior.[22-26]. Of relevance to the present study is the heightened concern about issues related to man-made hydro-acoustic disturbances. This increased concern stems partly from recent incidences with intense and long duration sonar sources and has led to a significant program-focus change in ATOC/NPAL project. [27-28]

Of special significance is the suggestion from examples of recent calculations based on the PI's theory [29] that sonic boom (SB) disturbances underwater at the overpressure level of 100-130 dB (re 1 μPa) and in the 10-40 Hz frequency range are expected to be audible by some marine mammals at a depth of one-half (1/2) km[*]. It is noted that the examples studied assume a signature length of 90 m typical of a supersonic transport; for a larger craft or rocket space-launch vehicle, the noise penetration depth can far exceed 1/2 km. Interestingly, these sound level and frequency range have been considered significant for Blue and Fin whales [23, 25, 26, 31, 32], expected to be audible also by deep-diving cetaceans, such as Sperm Whale, Bottle-Nosed Whales and Harbor Seals. [33, 34] The predicted *waveform* should then be important for its use in comparing with, or distinguishing from, the whale-call signals. Equally important to the audibility issue is how ambient ocean noise [23, 35, 36] may affect the underwater acoustic signals in question. In this regard, the duration of the predicted signals in deepwater should also be an important consideration, since the effective noise level affecting the perceived audible event is expected to increase with its duration. In the following, we shall review several problem areas and the specific issues which are the focuses of the current program.

[*] The results of those examples of applications and the methods of computations are documented in Ref. [30] which was included as Attachment I to this report. We note that the 120 dB often referred to in Refs. [23-32] falls well within the 116-126 dB (re 1 μPa) audible to a power-mower operator, or the passenger inside a light plane cockpit [69]; however, the dominant frequencies of these data were far above the infrasound range of interest.

2.1 Wavy vs. Non-Wavy Ocean Models

Existing methods based on the flat-ocean model fail to predict sonic-boom noise field underwater in the presence of surface waves, which proves to be very significant in determining the perceivable disturbances for impact study/assessment for large as well as small depth levels.

Most studies of SB noise underwater have been based on Sawyers' model [14] which stipulates a flat air-water interface. Among these are analytical development elucidating the original theory [17] and experiments validating the flat-ocean model [15, 16]. Compared to the earlier experimental studies of Ref. [15], the experiment by Intrierer & Malcolm [16] was more definitive in the validation of the Prandtl-Glauert (PG) rule applied to the maximum overpressure, but stopped short in confirming Sawyers' waveform prediction. Sawyers' model has been extensively used to study the effects of aircraft flight Mach numbers and input waveforms by Sparrow [18] and Sparrow and Ferguson [19]; the penetration depth of the SB disturbances was found to be rather limited, according to examples shown. An omission in Sawyer's theory is the important sea-floor influence which is expected to intensify the SB noise in the shallow coastal water where the impact is likely to be the most severe.

The investigation of Cheng and Lee [29, 29a, 37, 38, 39] recognizes, however, that a time-dependent effect arising from the interaction of an incident SB with a wavy ocean, though being a secondary effect near the surface, can significantly alter the sound level and tonal content predicted by the flat-ocean model and overwhelm the SB wave field at large depth. The significant influence of surface-waviness on SB noise penetration should not be too surprising in light of an early study on sound transmission from air to water by Medwin and coworkers [40, 41] who found that rough (ocean) surfaces generally augment transmission in accord with their theory and experiment.

The wavy-surface interaction problem in question has been studied numerically by Rochat and Sparrow [42], who employed a finite-difference procedure [43] which allows time-dependent computation of the acoustic fields in air and water simultaneously in a continuous calculation. The non-planar interface was simplified however in the computation model by assuming only a finite number of wave crests. Regrettably, the computed overpressure data were obtained (only) at depth rather close to the surface and no conclusion can be made with regard to surface-wave influence in the deeper part of the water. Their result did exhibit, nevertheless, the second-order oscillatory effect expected at small depth level in accord with Cheng & Lee's analysis.

2.2 Laboratory and Field Measurements

Existing underwater measurements in a ballistic range and at sea have not furnished data at depths sufficiently large (and/or for flight Mach number sufficiently high) to unambiguously support or dispute the wavy-surface influence; hence, their results and conclusions can not be applied to ocean sonic boom impact study.

There have been three documented underwater measurements of relevance to the present program which were described in some detail in the original program proposal. One is the water tank experiment in a ballistic range by Intrierer and Malcolm [16] to test the flat-ocean model mentioned earlier. Similar laboratory set-up implemented with a wave-maker can be used to ascertain the relative importance of Sawyers' model and Cheng and Lee's wavy-ocean models, as well as the latter's physical validity; this is in fact the basic feature underlying the design of T. Maxworthy and A. Fincham's laboratory experiment (Sec. 4).

A second document of interest is the study by Desharnais and Chapman [44] of overpressure waveforms recorded by hydrophone array which was identified with a Concorde airliner overflight. Quite

good agreement with Sawyers' theory was found in waveforms recorded on the upper part of the array; a prolong, monotone ringing feature departing from Sawyers' waveform was also noted, which Desharnais and Chapman explained as excited sediment boundary waves of the sea bed. While similar *ringing* features may also be attributed to the effect of interaction of sonic boon with surface waves (see Sec.3), the excitation of *sediment boundary wave* is indeed a topic of concern in the context of shallow-water sonic boom impact (see Sec.3.9).

The third document, which addressed more closely to the problem of undersea measurements with planned supersonic over-flights, is the work by Sohn *et al*. [45]. Reasonably good agreement with Sawyers' waveform was found at depth level down to one signature length ~ 40 m, beyond (deeper than) which conclusive results were unavailable[*]. The ambient noise level was determined to be too high at these depth levels; measurements at the deeper levels were not pursued in the belief that ambient noise level would not change with depth levels. This belief is contrary to the classic studies by Wenz [35] and Urick [36a] on ambient ocean noise, according to which underwater sound stronger than 100 dB (i.e. 1μPa) in the 5-30 Hz frequency range is not expected to be overwhelmed by ambient ocean noise. The authors surmised in their conclusion that the wavy-surface interaction effect will not be found in a real ocean. The lack of consistency among recorded waveform data and the limited time interval shown in the paper would suggest, however, that either the recording system or/and the signal analyzing procedure in Ref. [45] has ceased to function properly at the deeper levels. There is also an important factor that may have significantly limited the capability of this over-flight experiment with regard to detecting the surface-wave interaction effect. Namely, the flight Mach numbers of the experiment in the range of M_A=1.05-1.25 is too low to readily capture the effect in deep water of interest. For, according to the (Λ,Ψ) domain established in Part I (reproduced in Fig. 3.3 below), the significant effect in question is not expected to be found for M_A<1.25, except for those surface-wave trains aligned rather closely with the flight direction with (non-alignment) angle Ψ less than 15 degrees.

[*] Signature length is taken here to be the physical length scale characterizing the length of the sonic-boom overpressure waveform at the sea level. Cf. Fig. 3.1.

3. Model and Code Improvement, Extension and Applications

Specific task objectives under this category have been listed in the original program proposal (p.12) under three versions in the order of increasing effort and resource. We report that these task objectives have been fully achieved, with few exceptions, of which the problem are partly/fully resolved by research in related tasks and not of central importance to the value of the program product. These works of analytical and computational support to experiment (listed under I. A in Version I of the proposal), and of the super/focal boom model computation (listed under II. B in proposal Version II) are reported and discussed in Sec. 4 and 5.

Under the current program, signification improvement in the analysis and computer program of the surface-wave interaction effects have been made; worthy of note is the completion of a general code which is applicable to non-N waves and allows a number of new applications. The Sawyers' model has also been extended to shallow water and applied to studying sonic boom excited sediment boundary waves on the sea floor.

Equally important is the completion of the report by Cheng, Lee and Edwards [30], submitted as Attachment I, which documents examples of applications elucidating the distinct difference in noise fields characteristics between a wavy-surface model and a flat (non-wavy) model, and their dependence on the depth level, the surface-wave number and the Mach number. These studies and comparisons allow common features and trends to be inferred. Results of new applications and studies are also documented and examined in Cheng, Lee and Edwards report, including the sediment boundary wave analysis and generalization to non-sinusoidal surface-wave trains.

An improvement in the theory has been made in the removal of several unwarranted singularities in the deep water (far-field) analysis, which led to resolving an issue of Mach-number anomaly raised in the original program proposal[*]. Another issue resolved is the problem of uniformity of the approximation related to the theory's breakdown near shock jumps; the details in resolving this issue were given in Ref. [29]. The water-surface depression under the impact of the incident and reflected sonic-boom waves was an earlier concern; but it has been determined after a thorough analysis to be unimportant owing to the extremely short transit time and the high water-to-air density ratio, even under the more severe condition in our laboratory (where the overpressure may reach 100psf). The principal finding and results of the analytical and computational investigations will be presented in Sec 3.4-3.10, which are preceded by preliminary remarks on the theoretical model and the essence of the theory in Sec.3.1-3.3.

3.1. Model, Assumptions, Notations and Remarks

The theory adopts a model of two adjoining in viscid, compressible media, separated by an interface, across which the pressure and normal velocity (in the absence of surface tension) are continuous. The water-to-air density ratio ρ_w/ρ_A is assumed to be much high than unity (773.4 under standard condition). Its high density is expected to cause the water to behave very stiffly in response to the incident sonic boom wave, with little changes in fluid velocities and the interface geometry (to the level of approximation considered); whereas, the overpressure underwater must vary in response to that above water. The overpressure of interest, to be sure, is the pressure change from the local equilibrium value which increases with depth z (Refer to Figs. 3.1 and 3.2 for sign conventions and meanings for the depth, horizontal variables z and x, the sea-level signature length L', the surface-wave length λ, the

[*] This improvement was incorporated in the up-dated version of a USC AME Report 11-11-2000 by H. K. Cheng and C. J. Lee. [29] The results presented in Cheng, Lee & Edwards [Attachment I] and in this report were computed from updated codes consistent with the improved version of the theory.

horizontal velocity of the wave field trailing the space/aircraft U, the surface-wave velocity c, the swept angle of the impact zone Λ and the non-alignment angle Ψ.) As shown, the surface-wave depression is represented by $Z_w(x,y,t)$; for the sinusoidal surface-wave train considered, the maximum Z_w (which is one-half of the wave height) is $\delta\lambda$, and the maximum slope is $2\pi\delta$. An important quantity in the following analysis is the surface wave number $k=2\pi/\lambda$. Following Refs. 29 and 30 (see Attachment I), all length scales (such as x, y, z; λ) will be made dimensionless in the out set with the signature length L'. therefore, in physical units, the depth level is zL', the surface wave length is $\lambda L'$ and the maximum surface depression is $\delta\lambda L'$. The velocity U is assumed to be constant, or nearly uniform in time, and much larger in magnitude than c; the latter will be omitted in most applications. We will be concerned with problems in which the horizontal speed of the wave field movement U does not exceed the sound speed underwater a_w. This amounts to the requirement $M_A=U/a_w<4.53$ under the standard condition and corresponds to the condition on the ray entry angle in ray-acoustics theory, $\theta_i>12.75^o$.

3.2. Essence of Theory

Owing to its relatively slow attenuation rate governed by the cylindrical spreading rule, the time-dependent disturbances generated from sonic boom interacting with a surface-wave train can overwhelm the otherwise flat-surface wave field in deep water.

The significance of the surface-wave influence on deepwater wave field is made more apparent by a comparison in the spatial attenuation rate between the primary sonic-boom disturbances under a flat ocean and the time-dependent disturbances generated by the interaction with a surface-wave train. Whereas the former diminish with increasing depth level as the inverse square of the depth, i.e. $1/z^2$ for an N-like incident waveform, the interaction with wavy surface produces a continuous distribution of time-dependent, acoustic source that results in a much lower attenuation rate, namely, the inverse square – root of the depth level, i.e. $1/\sqrt{z}$. This behavior is in accord with the cylindrical spreading rule which is familiar from acoustics for a monochromatic point source in two dimensions (see, for example, Landau & Liftshitz [48])*. This cylindrical spreading rule is borne out by the 3-D theory in Refs. 29 and 30, and is a result of the extremely high aspect ratio of the sonic-boom impact zone. Hence, this time-dependent interaction effect, though being a secondary one at and near the surface, can exceed Sawyers' prediction in magnitude and overwhelm the otherwise primary wave field at large z.

3.3. The cylindrical-spreading domain

The parameter domain where the cylindrical spreading feature manifests is identified and will serve as a guide for its identification in field measurement and underwater impact study.

As shown in the theory [29, 29a, 30], there exists parameter domains of the normal Mach number $M_n=M_A\cos\Lambda$, the swept angle of the impact zone Λ, and the alignment angle of the surface-wave train Ψ, in which the effervescent, downward-propagating wave components are generated by interaction of sonic boom interaction with surface waves and results in the *cylindrical-spreading* (inverse square-root) behavior in deepwater sound field.

Owing to its importance to the designs of laboratory and field experiment, the boundaries delimiting these parameter domains are reproduced in Fig. 3.3 from Ref. [29, 30] for four flight Mach

* The cylindrical-spreading rate, as well as the mono-chromaticity (single-frequency) property of the wave-field at large depth level, are the result of interference among neighboring effervescent (non-attenuating) wave components detailed in Refs. [29, 29a and 30]. The latter were also called downward-propagating waves in Ref. 29a.

numbers based on the sound speed above water: M_A=1.05, 1.50, 2.00 and 3.00. They are determined by the requirements

$$M_w^2 \cos^2 \Lambda - \sin^2(\Lambda + \Psi) = 0 \tag{3.1a}$$

$$\Lambda = 90^\circ - \sin^{-1}\left(\frac{1}{M_A}\right) \tag{3.1b}$$

where the subscripts "w" and "A" refer to underwater and above water, respectively. The domain of interest for each surface Mach number M_A resides in the Λ-Ψ region interior of those bounded by (3.1a,b). (Note in this connection that for over-flight Mach number less than 1.25, such as those in Ref. [45], the underwater event of concern could not be easily detected, unless the surface-wave propagation direction is aligned closely enough with the flight path to within $\Psi \leq 15^\circ$, refer to Fig. 3.3).

The following presents the highlight from studies responding to the task objectives listed under Versions I-III in the original proposal, including the important flight Mach number and surface-wave number influence on waveform, sound level and frequency, code and theory extension to shallow water and sediment-boundary wave excitation. Most these results were obtained from an improved calculation programs based on more recent analyses in which the issues of non-uniformity and singularities (raised in the proposal) have been resolved.

For its application as a tool to help answering the audibility issue concerning marine mammals, we selected for our model calculations surface-wave train models of maximum surface slope δ=0.02-0.025 and surface-wave number k=4-16 for aircraft examples, and k=16-64 for rocket space-launch examples. With reference signature length scales L'=100 m and L'=1 km for aircraft and rocket space-launch, respectively, these δ-k combinations correspond to waves at sea states under moderate and fresh breezes [63, 64]. Whereas distant whale calls from baleen whales in/near the *infrasound* range can commonly be recorded at levels down to 100 dB (re 1 μPa) sound pressure level [31,32], and may have been considered critical for potential effect on behavior at 120 dB SPL (re 1 μPa), [23-25, 26, 27]. It has not been clear how deep down the infrasound signals from the surface-wave interaction may penetrate—with realistic length, time and pressure scales. This and other questions are answered by the examples studied below[*]. Another concern in applications is the ambient ocean noise in the frequency range of interest, which could mask the signals in question. Proper conclusion on these issues must take into consideration of the (passage) duration of the sound pulse, with which the noise effect on the sound-pressure level must increase. This point will be addressed in later discussions. More thorough studies of the analytical details and related issues are documented in Attachment I [30].

3.4 Example of a Basic Model: $M_A = 1.83$, k=4

> *An example for an incident N-wave is used to illustrate the several important solution stages, while showing a number of common solution features to be found in later discussions. The solution procedure used in this example was developed under the assumption of an N-shape, incident sonic-boom wave.*

We consider the wave field directly under the flight track (Λ=0) generated by interaction of an incident N-wave with a surface wave of wave number k=4, aligned closely with the flight direction (ψ=0)

[*] There is actually no ruling to date declaring the 120 dB SPL to be a harassment level, which must fall into the MMPA definition of Level B harassment and include degree and duration of masking effects [23,25]. There were instances where the interpretation of its legal definition was dismissed by regulatory agency.

(cf. Sec. 3.1 for definitions of Λ, ψ, k and other parameters). This example may be considered basic in that it illustrates a number of common features to be found in most other cases with otherwise vastly different properties. The examination will also illustrate how well the far-field formula for high $k\bar{z}$ may work for a moderately large $|k\bar{z}|$. Figures 3.4, 3.5 show in normalized form the complex amplitude of the overpressure on the wavy interface generated by the interaction $\hat{p}_2(x',0)$ and its Fourier transform (with respect to x'), $\hat{A}(\xi)$*. The latter is an important function in the deepwater (high-$k\bar{z}$) analysis; it controls directly the envelope of the deepwater wave packet; its absolute magnitude $|\hat{A}(\xi)|$ at high $k\bar{z}$ can be identified with the *acoustic exposure spectral density* [65]. Of interest is the successive "zero-crossings" where $\hat{A}$ vanishes.

The underwater solution to $\hat{p}_2(x',\bar{z})$ is obtained from the inverse Fourier transform of the product $\hat{A}(\xi)$ and a another known function of ξ and $\bar{z}$. The distribution of real and imaginary parts of $\hat{p}_2$ at two different depth levels z = 0.5 and z = 2.5 are shown in Figs. 3.6, 3.7. In Fig. 3.6 for z = 0.5, where the depth is only a *half* of the signature length L', the far-field formula derived for large $k\bar{z}$ (light dashes) works surprisingly well over the whole x'-range except near x'=0, where the formula still provides the right behavior and order of magnitude. The light dashes computed from the far-field formula is seen from Fig. 3.7 to closely capture the oscillatory features calculated by the intensive numerical integration (solid curve) at a moderate depth level which is two and a half of the signature length L'(z=2.5). Note that $k\bar{z} = 2.5$ is equivalent to $\bar{z}/\lambda \approx 0.40$.

To see how these results from the wavy-ocean model can be meaningfully compared with one based on the Sawyers' model; we must assign a value for the slope parameter δ. For the present purpose, we assume δ=0.02, and will present the results in terms of a normalized overpressure and the normalized time Ut/L'. Three graphs comparing the overpressure waveforms (in the time domain) predicted by the flat-ocean model (dashes), the time-dependent part of the wavy-ocean model (dash dots) and the sum (total) of the two (solid curve) are presented in Figs. 3.8, 3.9, and 3.10 for the three depth levels z=0, 0.5, and 2.5, respectively. As is apparent form Fig. 3.8, the reference overpressure is chosen such that the normalized maximum surface pressure is equal to 2. The persistent ringing feature is the response of the supersonic wave field above water to the sinusoidal surface-wave train and is clearly a *secondary* effect in the presence of the towering N-wave signature over the segment $0<x<1$. In Fig. 3.9 where the overpressure waveform at depth level of one-half the signature length (z=0.50) is presented, the wavy-surface effect begins to markedly alter the otherwise smoothly degenerated N-wave profile (in dashes); the peak over/under-pressure is seen to increase by nearly 45%. At z=2.5, Fig. 3.10 shows that even at this moderate depth level corresponding to only two and a half of the signature length, the expected dominance of the surface-wave interaction effect is fully realized. Here, the persistent ringing feature next to the surface transform itself into a *packet of wavelets* (dash-dot and solid curves) and overwhelms the otherwise primary (Sawyers) wave-field (in dashes). The waveform indicates a (slow) frequency downshift/sweep in the course of its passage, in accord with Doppler's principle. We note, in passing, that, this graph could be applied directly to an example with a 2 psf (pounds per square foot) maximum surface overpressure and a signature length L'=100 m. In this case, the peak overpressure would reach 0.06 psf at z=2.5 (well above the 120 dB (re 1 μPa) or 1 Pa mark mentioned earlier), and pulse duration more than 6 seconds.

* In accord with the analysis of Refs. 29 and 30, the overpressure generated by the interaction is given by the real part of the synchronous pressure $\delta\,\hat{p}_2\exp(-i\Omega t)$, with $\Omega = Uk\cos\Psi$, whereas the overpressure corresponding to Sawyer' solution is p_1.

3.5 Test of a General Computer Code: M_A=1.5, k=4

The computer code based on a more general solution procedure developed for non-N, incident waves is examined for accuracy/adequacy, using an example of incident N-wave as a test case, of which exact and accurate solution properties are known. This more general code allows applications to examples of incident focus/super booms and other non-N incident waves.

Results obtained for most our earlier studies were obtained by a computer program made strictly for incident N-waves. Usefulness of the program for space-launch applications requires consideration of non-N waveforms, and a program is developed for this purpose. Adequacy of this more general program in generating the surface velocity potential and the boundary-transfer term were of concern in view of the anticipated solution singularities [29, 30]. Detail comparison with the N-wave results in various solution stages has provided a crucial test for the general program. The unquestionable agreement in the comparison far Â and $\hat{p}_2$ is evident from Figs. 3.11, 3.12 made for the case M_A=1.5, k=4. The comparison for the normalized $\hat{p}_2(x', \bar{z})$ in Fig. 3.12 was made at the depth z=2.5.

3.6 Underwater Waveform Properties: M_A and k Dependence

Of interest to marine-mammal impact study are the over-pressure amplitude, frequency range, pulse duration and other waveform characteristics perceivable at depth, as well as their significant dependence on Mach number, surface wave number and depth level. These properties are examined for an incident N-wave of signature length and maximum over-pressure typical of aircraft supersonic flight, and for a moderate wav height. Results at depth levels near and far from the surface are obtained for combinations of three Mach numbers and two surface wave numbers. These data, together with corresponding examination on sonic booms from rocket space launch in Sec 3.10, establish the benchmarks needed for subsequent marine-mammal impact study.

The wave interaction effects are seen to depend linearly on the slope parameter δ, but are more critically (and nonlinearly) dependent on the surface wave number k and Mach number M_A. These dependencies have been studied for wide ranges of M_A and k for N-waves. The results for M_A=1.5, 1.88, 2.38, and k=4, 16 are shown and examined below.

Signal Duration and Ambient Ocean Noise

In an attempt to make the results more pertinent, we have assumed in the calculations a surface signature length L'=300 ft., a surface-wave slope parameter δ=0.025, and a maximum surface over-pressure of 2 psf. This allows the description of sound-pressure waveform in units of psf and second. As seen below, the sound-pressure of interest are found to be well above 0.002 psf corresponding to the 100 dB (re 1 μPa) level over a signature duration 4-6 seconds. From the viewpoint of signal's audibility, this observation is helpful in recalling that the maximum sound-pressure level (averaged over one second) of the ambient noise in deep as well as shallow water, contributed primarily by ocean traffic, were estimated by Wenz [35] and Urick [36] to be 80 dB (re 1 μPa/$\sqrt{\text{Hz}}$). According to the scaling rule based on the inverse $\sqrt{\text{Hz}}$, the effect of this ambient noise level on the perceived signal should remain well below the 100 dB (re 1 μPa) mark, as long as the signal duration does not exceed 100 seconds*.

Comparison With Flat-Ocean Model

* For a duration of 100 sec, the sound-pressure noise level in this case will be exactly 100 dB (re 1μPa).

The results obtained for the deep water at z=5 corresponding to the depth level zL'=1500 ft are presented in Figs. 3.13a, 3.13b, 14b, and 15b, showing unquestionably the dominance of the surface wave train effect p_2' over the corresponding signals of the flat-ocean model, p_1'. Data computed for the latter are plotted in solid diamond symbols but are so densely packed that they appear as a thick solid curve. Even at a depth level as close to the surface as z=0.50 (corresponding to 150 ft. below the surface), apart from the distinct ringing feature absent from the flat-ocean analysis, a peak overpressures 40% higher than Sawyer's prediction are found in most cases studied.

Effects of Surface-Wave Number Change

The effects of increasing k can be studied with Fig. 3.13a for k=4, M_A=1.5, and Fig. 3.13b for k=16, M_A=1.5, where results computed for the small and large depth levels (z=150ft, 1500ft) are presented. The results are in accord with the $1/\sqrt{kz}$ rule from the theory noted earlier. Similar comparisons with same conclusion have been made for M_A=1.88 and M_A=2.38. The instantaneous frequency pertaining to the individual carrier wave (wavelet) of the wave package is obviously controlled by the surface wave number k. Increasing k is expected to cause the wave packet more densely packed.

Mach-Number Influence on Wave-field Characteristics

(i) Overpressure peak. The wave-packet features are made more distinct by increasing the Mach number M_A. The peak overpressure in the large depth level (z=1500ft.) is seen from Figs. 3.13b, 3.14, and 3.15 to increase successively from 0.035 through 0.05 to 0.09 psf, as M_A increases from 1.5 through 1.88 to 2.35. A lesser peak increase trend with Mach number is also seen at the smaller depth level (z=150 ft.), with the peak overpressure reaching 0.25, 0.30, and 0.35 psf for M_A=1.5, 1.88, and 2.38, respectively.

(ii) Carrier-wave frequency. The number of wavelets seen earlier in the waveforms at M_A=1.5 are now seen to give a more densely packed waveform at the higher Mach numbers, M_A=1.88 and 2.38. Counting the number of peaks in the waveform (or the half of the zero-crossing number) within a given time interval should give a fair estimate of the *carrier-wave frequency*. Since the wave form in the forward part is more densely packed than in the real, the estimates must be made for the forward and real parts separately. Applying the counting to the forward and real portions of the waveform at depth level z=1500ft. yields two sets of frequency estimates:

M_A	1.5	1.88	2.38
t <0	19 Hz	26 Hz	43 Hz
t >0	14 Hz	19 Hz	24 Hz

Similar estimates with slightly less values are found with waveforms at the small depth levels (z=150ft.). The frequency downshift/sweep shown is expected from the Doppler principle*. This (carrier) frequency variation, however, indicates a (time-wise) build-up process of the acoustic power spectrum, namely, as the sound sources pass by, only a portion of the spectrum near the higher frequency end will first be built up; the remainders of the spectrum in the mid and lower frequency end are completed later (in time). The examples confirm the

* Frequency down-sweep is commonly reported in works on whale calls [31a,b, 32a,b].

conclusion from the theory that, in deepwater, frequency range of this spectrum is limited to a finite interval as in a band-pass filter. The frequency downshifts revealed by the waveform (observed in the rest frame) signifies that, forward, backward (as well as downward) propagating waves will be observed in a frame moving with the sonic-boom waves, as the result demanded by an acoustics model satisfying the correct radiation condition in the deepwater far field.

In passing, we note that as these carrier waves spread and move away, the propagation speed observed in the moving frame (identified with that of the crests and troughs) is shown in Ref. [29] to be none but the *group* velocity.

3.7 Non-aligned Wave Trains

The conclusions drawn on the sound level, frequency range and waveform characteristics studied in the preceding section are expected to remain applicable at locations far from the flight track and to more general sea conditions involving oblique waves and their combination. A series of calculation was made with examples in this and the next subsections to ascertain the degree to which this expectation can be realized.

As observed earlier, significant effects of the surface-wave interaction can be found only inside the (Λ, Ψ) domain for each Mach number M_A [Cf. Fig. 3.3]. To see how the underwater wave field within this domain holds up for non-vanishing Λ and/or Ψ is the main objective for the study comparing solutions for various combination of Λ and Ψ. Several examples in ranges of $|\Lambda|<30°$, $|\Psi|<30°$ are examined below for a fixed Mach number $M_A=2.38$.

As will be seen, while the waveforms can be noticeably altered, the magnitude of he peak overpressure and the general characteristics of the wave-packet are not significantly changed from those with $\Lambda=\Psi=0$ studied earlier.

Only representative results for three (Λ, Ψ) combinations are shown in Figs. 3.16a,b,c, in which the overpressure waveforms at depth level z=2.5 in the three cases

$$(\Lambda, \Psi) = (0, 0),\ (0, 30°),\ (-30°, 30°)$$

are compared, assuming $M_A=2.38$ and k=16. From these examinations, the peak overpressure and waveform characteristics are seen not being significantly different from the perfectly aligned case $\Lambda=\Psi=0$.

3.8 Multiple Trains Interference: "Cross Sea"

Chaotic-like waveforms could be generated with two or three trains running in different directions, aptly called "cross sea" [63] in such cases. In the following, undersea results from two of the several cases studied will be examined.

(i) *Example of Obliquely Crossing Trains*

We consider the wavy surface directly under the flight track (Λ=0) made up of an aligned (Ψ=0) and a non-aligned (Ψ=30°) train. For simplicity, we assume k=16, δ=0.02 for both trains. The sum of the two yields the p_2' waveform of interest and the result in total overpressure $(p_1' + p_2')$ is shown in Fig. 3.17a for the depth level z=2.5. Evidently seen are

the amplified overpressure peaks and the asymmetrical features in the waveform envelope caused by the mutual interference of the two crossing surface trains.

(ii) *Example of a Special Case: (0, 30˚) & (-30˚, 0)*
Since the entire water column under the flight track is a symmetry plane in this case, the overpressure perceived at any point therein is none other than *twice* the waveform value obtained earlier for $(\Lambda, \psi)=(0, 30^{\circ})$. The result is shown for the depth level z=2.5 in Fig. 3.17b.

3.9 Sonic boom over shallow water

Existing analyses of sonic boom penetration into water do not account for the presence of a sea floor and are not strictly applicable to the shallow coastal water where reflection and reverberation within the narrow channel will make the submarine impact much more severe. Additionally and depending on the elastic properties of the sea-floor sediment, the latter may resonate in response to hydro-acoustic disturbances generated from a sonic boom. A shallow-water model with a non-wavy surface is used to investigate its response to sonic boom; rigid and elastic bottoms are both considered, Examples studied confirm that sonic boom can excite sediment boundary waves under suitable sediment conditions.

The theory of Part I and the foregoing studies do not allow the presence of a sea floor. The potential sonic-boom impact is expected to be much more severe in the shallow coastal water than in the deep open sea. Here, the adjectives "deep" and "shallow" refer to the ratio of ocean depth to the (sea-level) sonic-boom signature length, h/L', being much larger and much smaller than unity, respectively. The theory extension to shallow water can be readily made, and lends itself to a study of the sediment-boundary waves. Occurrence of the latter phenomenon depends critically on the sediment shear-wave speed, C_s, which can be very low near the interface of certain sediments. There have been considerably different opinions with regards to modeling the vanishing magnitude of C_s next to the sediment interference and its importance [41a, 66, 67]. In the following we shall examine examples with the simplest sediment model to illustrate the potential of sediment wave excitation by sonic boom, proposed originally in Desharnais and Chapman's paper [44].

Flat-Ocean Bottom Effect

The sea-floor effect on the wave field below a non-wavy ocean under sonic boom can be studied as an extension of Sawyers' theory. For M_A<4.53 (under standard conditions), the elliptic underwater problem was solved in Cheng & Lee [39] paper through conformal mapping to a half-plane. As an example for demonstrating the bottom effect and the relative insensitivity of the wave field to the bottom's presence with the exception for its *vicinity* (and unless h/L'=1/2), we consider a model of an *open* water channel with a variable/adjustable (channel) depth h. We would like to predict the sonic boom generated overpressure at a *fixed* distance below the water surface, which is taken to be one half of the signature length, z=1/2, while the channel depths changes successively from h=8 to h=1/2. The result of the calculations made for an incident N wave at M_A=1.5 are shown in Fig. 3.18 together with a sketch identifying h, L' and the coordinates, where the (negative of twice of the) overpressure ratio

$$-2\,p'/\max p'$$

(measured in a frame moving with the sonic boom wave) is plotted as functions of x/L' for five channel depths in the range $0.5< h/L' <8$. The explicit integral form of the solution for $u' = -p'/\rho U$ is also reproduced in the figure.

Of interest in these plots is the relatively small departure from the Sawyers' waveform (which is valid for an infinite h/L') as the floor is raised, i.e., as the channel depth reduces, until the fixed (monitoring) station/level $z' = 1/2$ is reached, where an 80% peak-value increase is found on the sea floor. Accordingly, bottom effect may not appear to significantly affect the overpressure field under a flat ocean, except next to the sea floor and unless the open channel becoming shallower than h/L'=0.5.

The markedly amplified signal next to the bottom is nevertheless a significant feature to be recognized, concerning effects on the sea floor environment. The likely-hood and issues of exciting sediment boundary waves by sonic booms over shallow coastal water will next be briefly examined.

Sediment-Boundary Waves Under a Shallow Sea

The 2-D model

To allow interaction of an elastic, solid bottom wall with the hydro-acoustic medium, a 2-D shallow-ocean model is assumed. For this model three potential functions will be considered. Namely, in addition to the ϕ in water, a scalar potential Φ and a component of the vector potential Ψ for the sediment median, will be simultaneously solved. Each of these potentials satisfies their respective acoustics equations pertaining to the three characteristic propagation speed of the media C_1, C_p, and C_s with the subscripts "1" referring to the water, "*p*" and "*s*" referring to the compressive waves and the shear waves of the elastic medium, respectively. The speeds C_p and C_s can be related to λ and μ and density ρ, of the elasticity theory as

$$C_\rho^2 = \frac{\lambda + 2\mu}{\rho},$$

$$C_s^2 = \frac{\mu}{\rho}$$

Three compatibility conditions across the interface at (z=0) must be satisfied, which express the continuity in displacement, normal stress and shear stress.

Wave-train mode

For an infinitely extended elastic medium in half space, the three conditions at the water-solid interface at z=0, and the prescribed overpressure at the air-water interface z=-h together with a radiation condition or evanescent behavior at z→ ∞ (cf. sketches in Figs. 3.19, 3.20, 3.21), suffice for the determination of a *free-mode (resonance)* solution in the *wave train* form.

This equation system, with the implicit assumption of the two *homogeneous* media, is no more or less than that for a homogeneous wave guide with an elastic wall modeling ocean's sedimentary layer (see Ref. [60], pp.134-134), and is in common with the mathematical models of submarine earthquake, mud slides and large underwater explosion. The *finite* depth of the water layer/channel h, or its product with the wave train wave number, αh, is an important parameter that distinguishes the system from the

Stoneley wave (recoverable from the limit $\alpha h \to \infty$)*, and from the Rayleigh wave corresponding a vanishing water layer (recovered in the limit $\alpha k \to 0$). Unlike the latter two which are non-dispersive, the *dispersive* property rendered by the finite water depth provides (an infinitely) wider range of over-flight speed/Mach-number for resonance excitation.

Of interest is the *free* propagation mode, susceptible to excitation. Unlike wave guide studies concerning mainly with signal transmission along the wave guide (in the *x*-direction), our interest is how a traveling acoustic source, such as the sonic-boom wave field over water surface, may excite and maintain a sediment boundary wave. In Desharnais and Chapman's model [44], a more realistic multi-layer model representing *variable* C_p and C_s was employed. Whereas, the homogeneous elastic model adopted here offers greater simplicity in the analysis and perhaps more clarity.

The boundary conditions satisfying the interface compatibility requirements, the radiation condition far down the elastic sediment medium, and the free-surface condition yield the condition for the existence/occurrence of the *free (resonance) mode.* The latter condition determines the propagation speed or Mach number (of the mode) as a function of the depth-to-wave length ratio, or a function of αh. Its physical occurrence is restricted, however, to a finite range of propagation speed. This free mode has sinusoidal propagating wave along the water-sediment interface and, to be sure, a zero overpressure over the air-water interface. Its wave-field is recognizable as the one produced by a *concentrated*, moving surface force, with which the solution to the wave-field generated by the forcing with an arbitrarily distributed surface-pressure under the resonance condition can be constructed.

Sediment elastic properties selected

We shall select for this study the type of sediment materials with a shear-wave speed *low enough* to allow resonance to occur at an over-flight Mach number M_A under 4.53. From the list of sand and mud with (averaged) measured and computed elastic constants, North Pacific sediment, on Table 8.2.1 in Clay & Medwin [41a], p. 258:

		ρ/ρ_1	$C_p(m/\sec)$	$C_s(m/\sec)$
I.	Very fine sand (continental terrace)	1.91	1711	503
II.	Clay (Abyssal hill)	1.42	1491	195
		(1.91)	(1711)	(1.92)

In above, C_s was computed from data of Young's modules and other (measured) elastic constants. In both examples, the sound speed in air and water are taken to be C_a=331 m/sec and C_1=1500 m/sec, respectively.

The shear-wave speed in the second sediment model (clay) is so low that sediment wave can be excited even by a subsonic over-flight. The following will highlight the result of the first model with shear speed 503 m/sec.

Two examples with supersonic flight Mach number: M_A=1.5 and 1.36

With the set of constants assumed for data set I, and the assumption that the water-layer depth is twice the signature length, i.e. h=2, the resonance condition gives the admissible Mach number range in this case

* Stoneley's model treats two-adjoining elastic media.

$$1.35 < M_A < 1.44 \qquad (3.2)$$

Two Mach numbers M_A will be considered, one is outside the above range for the free mode, M_A=1.5, and the other is inside of it, M_A=1.36. Overpressure waveform at the sea level for an incident N-wave is shown in Fig. 3.19a where the normalized maximum overpressure was set equal to 0.33. The underwater waveform at mid tank (i.e. z=-1) computed for M_A=1.5 is shown in Fig. 3.19b. As expected, no evidence of interaction involving sediment medium can be found. In fact, the result differs little from that of a rigid, flat wall and compares closely with the result for h=1, z=1/2 examined earlier in Fig. 3.18.

Next, we examine the results for M_A=1.36 falling in the M_A-range of (3.2) with otherwise the same data set. The overpressure waveforms at the water surface z=-h=-2, at mid tank z=-h/2=-1, and on the bottom z=0, are shown in Figs. 20a,b,c. Unlike the underwater wave field for a rigid, inelastic lower wall as well as the elastic wall at M_A=1.5 in the preceding figures, undiminished sinusoidal oscillations at large distances in the anticipated form occur at both two lower depths levels. The oscillation on the sediment floor (z=0) is seen to be *twice* as strong as that at mid channel (z=-h/2=-1), indicating clearly that disturbances are generated from the multi-media interaction and radiated upward from the new acoustic sources on the bottom. Examples with other Mach numbers falling within the range of (3.2) have also been studied with similar conclusions.

A noticeable feature common to both mid-tank waveform in Figs. 3.20b is the lowering in amplitudes and shortening of oscillation periods in the vicinity of the center, x=0(1); the same feature is not found, however, at the floor level (z=0). This feature seems to support a finding reported in Desharnais & Chapman's [44] model study in that spectrum density in certain higher frequency band appear to increase with distance from the sediment interface. According to the present model, an explanation at a more elementary level can be made: the feature in question represents the *near-field* effect of the surface N-wave that attenuates and becomes indistinguishable at the bottom but remains detectable at mid channel.

Also of interest are the comparable values of the C_s, C_p, and ρ/ρ_1 selected for our model study that results in resonance in the M_A range $1.35<M_A<1.44$ and the representative values C_s=517 m/sec, C_p=1600 m/sec, and ρ/ρ_1=1.8 estimated in Desharnais & Chapman's model. The above estimate of C_s was made from the power law in Desharnais & Chapman's

$$C_s = 160(z)^{0.3} \qquad (3.3)$$

with z in meter, assuming z=50m. The Concord flight Mach number reported in the study was estimated at 1.75, equivalent roughly to be M_A~1.5, being not far from the upper M_A limit 1.44 of (3.2). (For diverging opinions on the shear-speed model, see Refs. [66, 67, 70, 71]).

3.10 Application to Rocket Space Launch

Sea level sonic boom signatures generated during the ascent phase of a rocket space launch differ drastically from those from aircraft supersonic over-flight not only in shock strength and signature length, but also in the wave-form. Their underwater impact is expected to be very different from, and much stronger than, that from aircraft over-flight examined earlier. In order to ascertain these differences and to establish bench marks for

subsequent impact studies, the wavy-ocean model is applied to an example with surface over-pressure of the Focus-Boom type taken from a Titan IV launch record for two sea states corresponding to a higher and a lower surface wave number. Apart from establishing the over-pressure range and waveform in the ultrasound domain at small and large depth levels, several underwater signal features unique to space-launch sonic booms are found.

Underwater penetration of sonic-boom noise from rocket space launch has been shown by Cheng & Lee [39] using a flat ocean model. It differs significantly from that of aircraft sonic booms not only for the much longer sea-level signature length, but also in the signature waveform resulting mainly from the rocket plume. The latter gives rise to underwater field characteristics distinctly different from that anticipated for a balanced *N* wave. In the following, we examine from the available records the distinct features of the sea-level sonic boom waveform produced during the ascent phase of a space launch, and their impact on the underwater acoustic field. Examples will be analyzed with both flat and wavy-surface models. The issues and studies on sonic boom *above* water related to rocket space launch and superboom are discussed in Section 5.

Known and Anticipated Features

Three overpressure waveforms representing the more severe sea-level sonic booms recorded during a typical space launch ascent are shown in Figs. 3.21a,b,c. The overpressure (in psf) shown in Fig. 3.21a at the sea level was inferred from data recorded during the ascent of Apollo 17 [49] when the launch vehicle reached an altitude of 100,00 ft., where the ambient Mach number was about 3.55. The speed of the wave-field movement at the sea level inferred from the calculated wave fronts is estimated to be 1,150 ft/sec, which corresponds to a Mach number above water M_A = 1.03 and a *subsonic* underwater Mach number M_w = 0.23. The peak of the sea-level overpressure exceeds 8 psf, while the signature length extends over an *x*-range of $L' = 6{,}500\,ft$ (nearly 2 *km*).

Similar sea-level signature waveforms were recorded during the ascent of a Titan IV launch, shown in Fig.3.21b with a peak overpressure also exceeding 8 psf and a signature length estimated to be 1 km long. Figure 3.21c reproduced from Hilton & Henderson [68] gives variants of sea-level overpressure wave forms recorded during Apollo 15 launch at different locations from launch site, among which is one with U-like double peaks along with the overpressure undershoot, much like the rabbit-ear or U-like feature characteristics of the overpressure distributions commonly found with focus booms.

With the sea-level signature of Fig. 3.22a (same as Fig. 3.21a) as input, the corresponding overpressure underwater was computed in Cheng & Lee [39] for a flat-ocean model to depth levels down to z = 1.5 *L'*. The overpressure at z = 1000 ft and z = 5000 ft corresponding 0.156 L' and 0.776 L' are shown in Fig. 3.22b and Fig. 3.22c, respectively. Included also in Fig. 3.22c is a (negative) source-like representation for Sawyer's solution at large depth levels (in dashes), signifying the dominance of a sink-like behavior resulting from the non-vanishing, negative impulse from the extensive real part of the sea-level signature. The latter has been attributed to the divergence effect of the rocket plume. Similar underwater features are expected of most space-launch examples in Figs. 3.21a,b,c. The subsequent study on a model utilizing the distribution from Titan IV (Fig. 3.21b) as input confirms the foregoing observations for the flat ocean and will reveal several unique physical as well as analytical properties of the wave field under a wavy surface.

Simple reasoning would suggest that owing to the large penetration depth made possible by the long signature length L', the wavy-surface influence could not play a significant role, as it has been with the *N*-waves. As a significant source of infrasound production, however, this influence cannot be ignored as will be made apparent below.

Rocket Space Launch: Infrasound under a Wavy Ocean

The similarity in shape of 3.21b with Fig. 3.21a (except for the one with double-spike feature), suggests that the horizontal Mach number for this data set must be in a supersonic M_A-range rather close to one, not fallen in the superboom domain. In the absence of concrete data on M_A, we took M_A = 1.08 for this numerical study. Assuming a surface sound speed above water as a_A = 331 m/sec, this M_A-value gives a surface speed for the sonic-boom wave as U = 357 m/sec, hence a signature length corresponding to the 3 second duration is $L' = 357 \times 3 = 1072m$. Note that the precise M_A is immaterial for the present purpose since the Prandtl-Glauert factor is

$$\beta_w = \sqrt{1 - M_w^2} = \sqrt{1 - (M_A / 4.53)^2}$$

which makes little difference from the values for M_A = 1, as long as M_A is close enough to one.

We shall first examine the case with k = 64. The latter corresponds to a surface-wave length $2\pi L'/k = 0.098L' \approx 100m$. Consider for the present purpose the wave field directly under the flight track $(\Lambda = 0)$ and a wave train well aligns with the flight track $(\psi = 0)$. As in the analysis for the N-waves, the Fourier transform of the surface overpressure in this case was computed. The inverse Fourier transform of the product $\hat{A}(\xi)$ with another known function of ξ and $\bar{z}$ were then be computed to obtain for the complex amplitude of the synchronous pressure at different depth level z. Results obtained from these intermediate steps will not be presented here but are documents in Attachment I, Ref. [30], in Figs 37a,b,c,d. The detailed examinations in Ref. [30] show good agreement of the far-field formula with the more exact numerical evaluation at $z = 0.125$ (for the same k) ought not come as a total surprise, since the far-field formula for large $k\bar{z}$ is of the form $k\hat{A}(\xi_*)/\sqrt{k\bar{z}}$. With k=64, the product $k\bar{z}$ is large indeed even at a rather small z like $z = 1/8$.

To see how the presence of a surface wave train may affect the underwater overpressure waveform in the time domain, one must assign a value to δ and a realistic scale to the overpressure, for which we take

$$\delta = 0.025 \qquad \max p' = 8.6\,psf$$

The latter was adopted in accord with the Titan IV launch record in Fig. 3.21b. The results are presented in Figs. 3.23a,b,c,d for four depth levels z=1/8, 1/4, 1/2 and 1, where the overpressure waveforms of the Sawyers flat-ocean model p_1' (in light dashes), the wavy-surface contribution p_2' (dash-dot curve), and their sum (solid curve) are plotted against time in seconds. Labeled along the ordinates for the overpressure in psf are the corresponding units in dB (re 1 μPa). The smooth, sink-like waveform from the flat-ocean model reaches down to a (negative) peak as low as $-0.4\,psf$ at $z = 1/8$ $(0.125km)$ and $-0.14\,psf$ at $z = 1$ $(1km)$, comparable to those found earlier for the Apollo 17 launch (Cheng & Lee 1998). While the wavy-surface effects (dash-dot curves) may not seem to contribute noticeably to the overpressure magnitude, there is a significant difference from results of the flat-ocean model with regard to *infrasound* production: whereas, the signal durations of $10 - 30$ seconds of these plots yield extremely low frequency in the range of $1/30 - 1/10\,Hz$ for the flat-ocean model, the wavy-surface interaction generates a wave-packet with frequency in the range of $3 - 5Hz$ (estimated by counting peaks) and a peak sound pressure well above $0.02\,psf$ or $120dB$ (re 1 μPa). To be sure, at the deepest level considered $z = 1$, the frequency is in the range of $5 - 6Hz$ with the wave-packet overpressure $114 - 126dB$ (re 1 μPa). Accordingly, these infrasound signals at depth level $1/2 - 1$ km underwater have durations lasting

$20-30\,\text{sec}\,onds$, depending on the chosen cut-off amplitude. Noteworthy is the *frequency downshift* characteristics, which is typically $3-4Hz$ downshifting to $1-2Hz$ for depth levels $1/8-1/4\,km$, and $5Hz$ downshifting to $3Hz$ at the larger depth levels $1/2-1\ km$. Even though the peaks of the wavelets are relatively small, the wave-surface effect does add markedly to the total overpressure. All results shown can be closely reproduced by the semi-analytic procedures based on the far-field formula described earlier.

To see how a reduction in the surface-wave number *k* may affect the underwater signal waveform and intensity, we examine the case of $k=16$, with M_A, δ and other parameters unchanged. The results for $k=16$ are presented in Figs. 3.24a,b,c,d in an order corresponding to results presented earlier for $k=64$. Of the time-domain overpressure waveforms, a common feature noticeably different from those in Figs. 3.23a, b, c, d for the higher *k* is the lower carrier-wave (wavelet) frequency of the wave packet (cf. dash-dot curves); this is made evidenced by the increased spacing between the neighboring wavelets, expected as a result of the four-fold reduction in *k*.

A more significant property upon examining closely these two data sets is, however, a significant departure from the large-k behavior observed for the N-wave and other similar signatures in the analysis for large kz (Appendix IV). The peak $|p_2'|$ from the foregoing calculations for the space launch reveals, instead, a slight reduction from that for $k=64$. Owing to the importance of this issue, a computer program re-run was made for the case of $k=64$ with the $\xi-$range extending much further to $-300<\xi<300$; the results change little however from those of the earlier runs.

In the more general case, the far field formulas for high $k\bar{z}$

$$\hat{p}_2 \propto \frac{k\hat{A}(\xi_*,k)}{\sqrt{k\bar{z}}} \tag{3.4}$$

still holds, as it has been substantiated by the foregoing examples for a *fixed k*. Unlike the expectation from the N-wave, examination of the computed results in Figs. 3.23 and 3.24 indicate that $|\hat{A}|$ may no longer reduce with large *k* simply as the reciprocal of *k*'s. *T*herefore the inverse $\sqrt{k}$ rule for $\hat{p}_2$ may not apply in these cases involving large and different *k*'s.

The foregoing examinations and comparisons have brought out not only several distinct underwater wave field feature unique to the rocket space launch, but also the importance of the function $\hat{A}(\xi;k)$; its analytical structure and its relations to physical nature of the wave field deserve more thorough investigation in future work.

4. Laboratory Study of Sonic Boom Penetration under a Wavy Air-water Interface

4.1 Primary Objective

Based on the theory of Cheng & Lee [29,30] a relatively rapid program of experimental validation was initiated. The primary objective is to find the theorized effects in the laboratory and subsequently map the appropriate parameter space.

4.2 Laboratory Facility

Design consideration and specification of laboratory facility, test tank, surface wave generator, pressure senor array, electronic and computer supports.

Due to the implicitly noisy and disruptive nature of the experiments, they were carried out in a specially constructed acoustically damped room inside a larger experimental facility. This laboratory was specifically constructed for hypersonic projectile experiments in the late 50's and is located in a basement room with 28 inches (91.9 cm)thick concrete walls. The acoustical chamber measures 16 x 12 x 8 feet (52 x 39 x 26 cm)and has lead sheet foam sandwich walls and roof. Its effectiveness permitted testing with no significant noise disturbance outside of the laboratory. The inside walls of the chamber were lined with acoustic absorbing/diffusing foam that reduces any extraneous shock reflections that could interfere with the measurements.

A Plexiglas tank of 96 x 17 x 22 inches (315 x 56 x 72 cm) was lined with open-cell acoustical absorbing foam and mounted onto an optical table equipped with pneumatic vibration absorbing supports. A wider tank of 96 x 42 x 24 inches (315 x 138 x 79 cm) was also constructed, the larger tank would allow duel wave-generators to be installed and show the independence of the measurements on the tank geometry. The tank is housed in the acoustical chamber and is separated from the launch device by a thick foam-filled wooden wall. A small projectile sized hole in the separating wall permits passage of the projectile while restricting the blast associated with each launch from contaminating the measurements. The distance between the launcher and the wall was chosen so as to ensure that the projectile had already escaped from the launch associated blast wave before it entered the hole in the wall. A fast Darlington type phototransistor/photodiode combination fitted inside the wall provided consistent accurate triggering capabilities for each run. Pointed tip, blunt tail projectiles of diameter 7.7 mm and length 30 mm were fired from a rigidly mounted launcher and collected in a sand-filled steel box. Changes in the mis-distance (distance from the flight path to the water surface) could be made by raising or lowering the tank. The launch velocity was measured at 2300 fps (628.8 m/sec) corresponding to a Mach number M_A=2.02 for the laboratory conditions and was found to vary less than 0.3% between runs. Both the projectile size and velocity were kept constant for all experiments. The mis-distance was kept at 13.5 inches (44.3 cm) for all of the data presented here.

Surface capillary-gravity waves were generated by two different wave-generating systems. The first consisted of a span-wise wedge shaped paddle that was oscillated vertically through direct mechanical coupling to a pair of moving-coil actuators (speakers). Due to the fall off in surface wave amplitude away from the paddle, it was necessary to position the acoustic sensors relatively close to the point of wave generation and adverse effects due to shock reflections from the part of the paddle above the water were detected. These effects limited the placement of the sensors to a minimum of 10 inches in front of the paddle, at a location where the surface wave amplitude was marginal. A second wave-

generator was constructed from a simple hinged strip of polycarbonate measuring 0.75 x 21 x 1/16 inches (3.9 x 3.3 x 0.21 cm) glued to a 1/8 inch (0.41 cm) diameter titanium rod. The entire mechanism was located just under the water surface and was actuated through a slightly more elaborate system of mechanical coupling. This wave-generator was found to be almost invisible to the shock (as it was physically located beneath the water surface and had an acoustic impedance close to that of the water) and was also capable of producing larger amplitude surface waves; this was used for all experiments subsequent to its development. The paddle could be driven with any arbitrary waveform and was capable of a maximum excursion of 7 mm peak-peak. Figure 4.1 shows a perspective view of the basic laboratory setup.

All pressure measurements were made with Kistler model 211B4 and/or 211B5 type piezotron sensors with resonant frequencies of 500 and 300 kHz respectively. The piezotrons were powered by a Kistler model 5124A1 charge coupler equipped with filters in the 30-250 kHz range as was determined appropriate based on the analysis of preliminary results, a single unfiltered channel was left in all runs so that any unpredicted high frequency effects would not be lost. The transducers were flush mounted into a 5/16 inch (1.03 cm) thick Plexiglas plate of width 2 inches using Kistler model 221A sensor mounting kits. Five sensors were typically used across the span with a spacing of 2 inches. Kistler model 1635A cables were used to couple the piezotrons to the charge amplifier. The plate containing the sensors was secured to a Plexiglas frame with several steps located at known vertical depths. The frame was fixed to the floor of the tank with absorbent foam mounts and lead weights. The entire array of sensors could then be lowered or raised as a group with no changes to the water depth by changing the step locations (this is in contrast to the experiments of Intrieri & Malcolm (1973) where the sensors were fixed and the depth changed by added or subtracting water to/from the tank.) in this way the distance from the flight path to the water surface was kept constant ensuring the same surface forcing for each run. All data was sampled at either 245 or 600 kHz using a National Instruments model PCI-MIO-16E data acquisition board driven by a custom Lab View program capable of acquiring pre-trigger data at up to 1.25 Mhz. The pre-trigger acquisition feature enabled the measurement of any launch-associated vibration transmitted through the concrete floor into the tank before the arrival of the projectile.

4.3 Measurements

Test procedure, projectile speed, reference signature length and measurement period.

A standardized testing procedure was introduced to ensure both good repeatability and to improve on the overall safety of the experiments. The data acquisition computer and charge-coupler were run on batteries to avoid line noise in the data. All other unnecessary electronics were switched off during data acquisition to help ensure an electrically quite environment. All tests were repeated at least twice to ensure ongoing repeatability and as progressive improvements to the laboratory setup were made older data was shelved in favor of the newer results. Some typical pressure wave-form just above the surface of the water are shown in Figure 4.2. It can be seen that the waveform is asymmetric due to the blunt rear of the projectile and the relatively close proximity of the measurements to the flight path. The speed of the projectile was measured at the testing location by fitting 2 piezotrons into a Plexiglas plate with a precisely known longitudinal distance between them and placing the plate on the axis of the tank just above the surface of the water, the sharp signature characterized in Figure 4.2 provided a sufficiently accurate measurement of the projectile speed. Similar data was used to calculate the reference length scale based on the incident wave signature hitting the surface of the water L'. L' was measured as the distance from the positive and negative pressure peaks of the incident wave form and was found to be 8.05 cm. Figure 4.2 shows such data. Although the flight time from launcher to collector was less than 6 msec data was collected from 8 msec before the launch till 12 msec after the launch.

4.4 Flat Water Surface

Verification of Sawyers's attenuation rule, identification and control of random and repeatable noise sources.

In order to characterize the impacting wave signature and to re-verify experimentally both the Sawyers model [14] and the Prandtl-Glauert rule, a large number of tests were done with a flat air-water interface. Most initial testing was aimed at verifying the repeatability of the incident wave in the air and at optimizing the tank/wave-generator geometry so as to eliminate or minimize any reflected/refracted shock effects.

An Initial series of tests were performed to examine the effects of depth level on the over-pressure attenuation. Measurements corresponding to the far-field/large-depth attenuation were made at depths of 3.41, 8.096, 15.875, 24.13, and 29.845 cm all tests were repeated twice. The resulting peak-peak over pressure verses depth level plot is shown in Figure 4.3.

Figure 4.3 shows a power-law curve fit for the far-field overpressure attenuation of $z^{-1.8}$ which is rather close to the z^{-2} in Sawyers model. Individual overpressure waveforms corresponding to the data points in are shown in Figures 4.4.

As can still be seen from Figure 4.4 (which corresponds to *typical* data taken toward the end of the experimental program after many improvements to the signal to noise ratio were made) as the depth increased the signal to noise ratio of the measurements decreased and at depths below 15 cm it was initially difficult to distinguish the over-pressure signature from the noise. A systematic study aimed at isolating the noise source led to the realization that the noise had 2 components, the first component of the noise was random in nature and associated with the electronics and data acquisition system, the second component proved to be systematic and repeatable and was traced to specific details of the tank/launcher geometry. The random noise was greatly reduced by increasing the charge-coupler gain and improving the overall quality of the wiring; a large isolation transformer and UPS system was installed and used to power all relevant electronics. The repeatable "noise", which appeared as a pre-cursor to the overpressure signatures was shown to correspond to upstream disturbances. These underwater disturbances propagate faster than the speed of the projectile and arrive at the measurement station before the incident wave reaches a detectable level. Appreciable change in the form, phase and amplitude of this pre-cursor were observed when changes were made to the upstream projectile inlet. A smooth vertical wall flush with the upstream end of the tank appeared to work best, but the amplitude of the pre-cursor still limited the maximum depth of useful measurements to 20 cm[*]. Further investigation showed the existence of "sweet spots" at particular longitudinal positions in the tank. These sweet spots were characterized by almost no measurable pre-cursor and were typically 10-15 cm long. It was found that by introducing vertical span-wise sheets of low-density open-cell foam (much like a kelp bed in the coastal ocean) at particular longitudinal positions sweet spots could be induced in a controlled manner. The foam sheet which were typically a 1/2 inch thick were held down with lead weights and did not necessarily need to cover the full span or depth to be effective. They did have a tendency to loose their effectiveness as they became waterlogged after a few days of operation. These foam baffles were never closer than 3 signature wave lengths to the piezotrons.

4.5 Wavy Water Surface

[*] The positions in the tank where the repeatable, precursor-type disturbances in question are undetectable.

Stereo-amplifier generated capillary-gravity waves, surface wave train properties, measurement and comparison with Cheng and Lee's cylindrical spreading rule, wave train non-uniformity and other experimental departures from theoretical model.

The primary objective of the project was to determine whether any measurable difference in the underwater signature with and without surface waves could be detected. A large number of ad-hoc tests were done over a wide range of the parameter space at a depth of 10 cm, with the sole objective of qualitatively finding the ringing effect described by Cheng & Lee [29, 29a, 30]. Evidence of this effect was soon found see Figure 4.5 (which shows a *typical* run from the early stages of the experimental program, corresponding to the randomly chosen parameters indicated). The data in Figure 4.5 is noisy and the pre-cursor mentioned above can be clearly seen. Figure 4.6 shows data with and without surface waves for one of the later experiments when much amelioration to the experimental setup and data acquisition system had been completed. A preliminary systematic exploration of the full relevant experimentally obtainable parameter space was subsequently followed. It should be mentioned that due to the large difference in the speed of propagation of the surface waves as compared to the speed of the projectile, the surface wave field could be considered stationary in all cases. This results in uncertainity in the actual phase of the waves at the time when the projectile is directly above the sensor. This uncertainty in the surface wave phase is a source of error in determining the peak amplitude of the wavelet packet envelope.

By performing multiple ensembles for the same experimental conditions the form of the envelope can be obtained (as the phase for each run is random). This is illustrated in Fig. 4.6 when the signals corresponding the differences between the wavy and flat water surface are shown for two different ensembles of the same experiment, in which the true form of the wave packet envelope can be better seen.

The Generated Wave Fields

The surface wave fields were generated by forcing the paddle described in Section 2 with a sinusoidal signal generated by a BNC Model 625AT Arbitrary waveform generator, the signal was amplified using a classical Car Stereo amplifier before being fed in parallel to a pair of high performance speakers that were mechanically modified to drive the paddle in phase with their motion. This technique produced surface capillarity-gravity waves that decayed exponentially with distance from the paddle. An image of a typical wave field is shown in Figure 4.7.

Surface Wave Amplitude Measurement

As predicted by the theory of Cheng & Lee [29,30], it was found that the strength of the phenomena was strongly dependant on the surface wave amplitude and surface-wave number. The amplitudes were initially measured using a vertically mounted depth micrometer, which closed a circuit lighting a small LED when it made contact with the water surface. This approach proved laborious and inaccurate; in addition this procedure required the installation of an apparatus that had to be removed before each test. A non-intrusive optical wave height measurement system was subsequently developed.

This optical measurement system consisted of a small laser diode that was aimed at an approximately 25-degree angle such that the beam was reflected from the water surface onto a screen placed just in front of the collector. Any change in the water surface slope would cause the beam to move on the screen. Careful comparisons between the optical and mechanical measurement systems yielded differences of less than 8%.

Using the optical wave height gauge the typical wave heights at any location in the tank could be quickly measured. Due to strong capillary effects at the relatively small scale of the laboratory setup, the surface waves exhibited significant decay in amplitude away from the generating paddle. Figure 4.8

shows the wave half height as a function of distance behind the wave-generating paddle for forcing frequencies of 5, 6 and 7 Hz corresponding to surface wavelengths λ of 3.1, 4.2 and 6.0 cm respectively.

Figure 4.8 shows clearly that the shorter wavelength waves have larger decay exponents making the generation of a constant wave height wave field more difficult. Substantial efforts have been made to reduce the decay rate by adding a stationary paddle upstream to cause forming a standing wave and by adding surfactants (see Attachment 2), but these are not used in the final measurements, owing to complications in the resulting waveforms and other reasons. Qualitative diagrams of the measured surface wave amplitudes for two of the typical surface wavelengths used in the majority of the experiments are shown in Figs. 4.9, 4.10. Once again it can be seen that the smaller values of λ are associated with larger decay exponents, an effect that is to be expected and will be discussed later when the dependence of P_2' on λ is examined.

The Non-uniformity of Delta: Departure from Theoretical Model

The surface wave amplitudes are characterized by δ=A/λ. According to Cheng and Lee the peak amplitude of the envelope P_2', ($P_2' = P_{total}$ (with waves)-P_o (flat water)) should increase linearly with δ. As δ in these experiments decreases exponentially away from the wave-generating paddle and as the region of surface influence increases with the depth of the measurements, only measurements made at relatively shallow depths can be expected to have a moderately constant surface wave train amplitude influence. Figure 4.11 shows P_2' as a function of δ for a depth of 8.1 cm and λ=4.17 cm. At depths of less than L′~8cm we are typically in the near field for both the flat water and the wavy water attenuations. As these experiments are aimed primarily at verifying the far-field attenuation laws for both the flat and wavy air/water interfaces, data taken in the near field (z<L′) where the surface wave trains influencing P_2' are relatively constant in amplitude are not useful. For depths greater than L′ where the surface influences consist of a region with increasing variation in δ with depth, we expect significant deviation from a linear dependence of P_2' on δ. This is illustrated in Fig. 4.12, where P_2' is shown verses δ for 3 different depths. The deviation from linearity at depths of 15 and 29 cm is particularly noticeable for smaller values of δ where capillary forces are more dominant making the variability in δ even stronger.

The values of δ used in Figs. 4.11, 4.12 are measured perpendicularly above the piezotrons and do represent some typical value but, due to the exponential decay of δ, they are neither average values, nor is their representation constant when either one of the depth, the surface wavelength λ or δ itself is varied. When determining the maximum value of the P_2' envelope from these time traces, the peak values are used regardless of their location in the envelope. The precise location is always noted with the intension of using the data from Figs. 4.8-4.12 to determine the approximate value of δ for the particular surface wave corresponding to the peak amplitude sub-wavelet within the envelope that gave this maximum value for P_2'[*].

The Attenuation of P_2'

The theory of Cheng and Lee [29,30] predicts a far-field 2D cylindrical spreading type attenuation of P_2' with depth, corresponding to $P_2' \sim \varepsilon\delta/z^{1/2}$ where ε is the overpressure ratio $\varepsilon = P'/P_a \sim 0.1$. Figure 4.13 shows $P_2'/\varepsilon\delta$ plotted against the normalized depth in reference signature lengths L′. A best-fit line shows an attenuation as $z^{-.55}$ not too far from the $z^{1/2}$ predicted by the theory.

[*] Since the tail end of the measured waveform is affected by disturbances from downstream, the measurement may not captured the total acoustic (exposure) energy perceived at a specified depth level, as pointed by the commentator.

The data in Figure 4.13 can also be represented by normalizing P_2' by the measured values of P_2' at one signature depth. Such normalization is justified as the inverse-square-root attenuation law is only valid in the far-field which corresponds roughly to depths greater than 1 signature. This is shown in Figure 4.14, where slightly better collapse of the data is observed and there is better agreement with the theory. Here the departure from the cylindrical-spreading rule is seen to be no more than 20%, corresponding to a discrepancy less than 2 dB (re.1 uPa). Future laboratory experiments will provide measurements at depth levels less than one signature length, and will be compared with Cheng and Lee's theory which is not restricted for a large z.

Individual time traces of P_2' are shown in Fig. 4.15 for 4 different depths, it can be seen that, in accord with the theory, as the depth increases the width of the envelope of P_2' also increases and a larger number of wiggles can be seen. The asymmetry in the envelope is clearly seen to increase with depth as the area of surface influence increases. By using Fig. 4.8 it is possible to estimate the local δ for each wiggle in Fig. 4.15, for the depth of 29 cm the δ measured directly above the probes is estimated to be about 60% the δ responsible for the largest amplitude wiggle to the right in Fig. 4.15 which occurs about 5 inches downstream of the sensor location.

Dependence on the Surface Wavelength λ

The development of the P_2' phenomena is strongly dependent on λ or k and as anticipated from the theory of Cheng and Lee there is a specific range of L'/λ where the phenomenon is observed. Measurements were made for a range of L'/λ corresponding specifically to λ 's of 1.53, 1.87, 2.36, 3.1, 4.17, 6.0, 9.46, 16.77 and 29.5 cm. The dependence of the effective δ on both λ and the depth make it difficult to isolate the most receptive value of L'/λ without first decoupling the effects of δ, such an analysis is presently in progress and using the technique described briefly above should be viable, but time consuming. Nonetheless some preliminary observations can be made.

A crude estimate of the optimum ratio L'/λ can be obtained from some of the preliminary data taken with the first generation (wooden, vertically oscillating) wave paddle and based on mechanical measurements of δ. This data is presented in Figure 4.16, and shows an optimum λ/L' (NOTE INVERSION) of about 2. Some typical plots showing the relative contributions of the total measured pressure P', the flat water component P_1' and the wavy water component P_2' are shown in Figs. 4.17-4.20.

Non-aligned Wave Trains

In an effort to ascertain experimentally if the surface-wave influence may be reduced substantially by the non-alignment of the wave train normal with the flight track (as in the case of $\psi=0$ in Fig. 3.3), the channel axis was moved from the originally aligned position to a yaw angle $\psi=15°$, without moving the launcher and the flight track.

Several tests with the yaw were made under otherwise similar conditions for the aligned case. Measurement records of overpressure waveform and P'_2 amplitude (documented in Attachment 2) show no substantial large from the case $\psi=0$ in which the surface wave propagation direction aligns perfectly with the flight track. This is not surprising since, according to Fig. 3.3, $\psi=15°$, (as well as $|\Lambda|<15°$) is well within the progressive/effervescent wave domain pertaining $M_A = 2$. Details of these and other measurement, and data analysis are examined and discussed in the Attachment II

5. Rocket Plume Related Focal and Superboom Problems

The most intense sonic booms can be expected to occur during the ascent phase of space vehicle or supersonic aircraft; the observed and predicted signatures are complicated by features resulting from wave focusing and changing of wave field structure due to sound speed variability of the atmosphere [9-13]. The designations of "focus booms" and "carpet booms" have been used by Plotkin and others [13, 55, 72, 73] to distinguish sea-level sonic boom (overpressure) signatures having typical features resulting from ray/wave focusing from those having none. Among these typical features is the *spike-like*, high-pressure peak associated with a shock. When the surface (horizontal) Mach number of the sonic boom wave becomes sufficiently close to unity, the sound-speed variation in the field can result in wave field intensification in the vicinity of the hyperbolic-elliptic transition boundary where nonlinear effects may also manifest. The latter phenomenon is referred to as "superboom" after Hayes [5]. The transition boundary/plane beyond which the hyperbolic property of propagating waves cease to apply may be called the *cut-off* boundary. Available model analyses of the superboom problem are few and incomplete to help in identifying its existence from the recorded data. In the context of sonic boom noise penetration underwater, the foremost issue in analyzing the focus-boom and the superboom problems is how to predict the exhaust plume effect on the sea-level waveform or to construct a model for simulating its effects. The plume effect and its related superboom problem can be addressed separately in two tasks

(I) *Rocket-plume effect modeling:* Comparing results by different existing models and generating new source models.

(II) *Superboom model study:* Solving the superboom problem with new boundary conditions pertaining to rocket space launch.

The difficulty in task (I) is the great variety in sea-level waveform that can result from minor variations in the equivalent source models for the plume. Whereas, in task (II), waveform data are available only for the ground level which cannot be used as the boundary condition at the upper boundary of the superboom domain. The results from studies in these two problems are reported below.

5.1 Rocket Plume Problem: Saturn V Ascent Booms

Except for predicting the peak over-pressure, existing sonic boom propagation methods/codes have never been successful in reproducing measured sea-level sonic boom signature of the Focus-Boom type from either aircraft or space-launch operations. This represents a serious discrepancy for underwater impact study, for which the under-pressure (negative-phase) part of the sea-level waveform is known to contribute principally to the deep water wave-field. The cause of this discrepancy is believed to lie in the determination of the source function with inadequate near-field data from the rocket plume. While this discrepancy, as well as the other code break-down treated in Sec.5.2, address problems mainly above the water, they are both essential in furnishing the surface data needed in underwater impact study for space launch operations. The following describes the several computational studies of near-field over-pressure and plume-shape effects on the Focus-Boom type signatures. A high degree of sensitivity to plume shape change is demonstrated, while an adequate model for determining the correct source function is yet to be found.

In order to ascertain the capability of existing propagation programs in predicting correctly the sea-level waveforms produced by rocket space launch of interest, tests must be made on PCBoom and other codes utilizing several candidate "source models" for the exhaust plumes. There have been two models of this kind: one is based on a "universal" Javinen-Hill plume model along with the Tiegerman-Seebass (hypersonic) shock model which has been built in as an option in the Wyle PCBoom3

propagation code [72]. The second one employs a subroutine called "Thomas Delta- P/P vs. X" mode that utilizes the Ames wind-tunnel model data [73]. The latter was a *truncated* wooden model simulating the exhaust plume, much used in the NASA Saturn V/Apollo study series [73]. It was planned earlier to repeat the calculation in Ref. [49] for the Apollo 17 study on PCBoom3 and another NASA propagation (Thomas) code, using the same (second) plume-source model as the near-field option—to see if the long, negative-phase feature of the waveform can be captured. The latter has never been made clear in Ref. [49] and other existing documents.

Another important input needed for the calculations is the recorded or designed vehicle trajectory and flight history. It was decided after a search in the NASA archive, with help of J. Mendoza, that Saturn V ascent booms, for which records of design trajectory and flight history are available through the 1965 NASA/MSFF Report [74], were selected for the study; the computation task was to be carried out at Wyle Laboratories by K. Plotkin, using mainly PCBoom3. (The calculations employing the NASA Thomas code were abandoned owing to the lack of sufficient computer resource for J. Mendoza). As a support to aid understanding of the exhaust plume issue, a study of the plume-shape influence was also made by S. Cheung, using an Euler code.

The study with PCBoom calculations were made in two categories: one pertains to applications implemented with the two source models of the plume mentioned, and the other represents an unusual approach which used inputs inferred from field data recorded at the sea level and applied the code in the reversed propagation direction. This reversed approach may furnish a set of near-field data for the unknown rocket plume responsible for the recorded sea-level signature of interest; the error in the (ray-acoustics based) propagation code in the plume vicinity may however cause discrepancies, and some iteration cycles with help of an Euler code may be needed for the solution convergence in this case.

PCBoom Calculation: Two Saturn V Plume Source Models

These calculations used the 1965 design trajectory and flight history of Saturn V ascent mentioned; an updated version of PCBoom, referred to as "PCBoom3", was used. As planned originally, the two plume source models used were:

Source Model 1 Universal plume (Jarvinen-Hill) model [75] plus hypersonic shock model (Tiegerman-Seebass) [76],

Source Model 2 Extrapolated Ames wind-tunnel data via the Thomas delta-P/P vs X mode [73, 74].

The Ames data for Model 2 are the pressure signatures documented in NASA Rept. TMX-62, 117 [74] for ten Mach numbers over a range from 3.01 to 7.29 for a .00053-scale model of the Saturn-Apollo launch vehicle complete with an exhaust plume simulated by a wooden aft body.

One run was made for each source model; two sets of outputs were selected from each run to produce a "carpet boom" of which no ray-focusing is evident, and a "focus boom" with features characteristic of a caustic. A total of four sets of outputs were obtained, labeled as: Focus 1, Carpet 1, Focus 2, and Carpet 2, detailing sea-level overpressure signature, specific launch and flight conditions and wave-field properties.

With the surface sound speed of 1118 ft/sec, the focus boom in each case is chosen when/where the surface (horizontal component) Mach number is 1.146; whereas the carpet boom in each case is chosen where/when the surface Mach number is a slightly higher value, 1.167.

The computed results in sea-level overpressure waveform for Focus 1 and Carpet 1 are shown in Figs. 5.1a and 5.1b, respectively; the corresponding results for Focus 2 and Carpet 2 are shown in Figs. 5.2a and 5.2b, respectively. The full length of the signature can be inferred from the waveform duration and sound speed for each case: 897 ft. for Focus 1; 921 ft. for Carpet 1; 4,030 ft. for Focus 2, and 3,859 ft. for Carpet 2. The boom magnitudes found in Focus 2 and Carpet 2 are too high, being three times higher than the corresponding cases with source model 1. The large differences are believed to have resulted from using direct near-field signatures, rather than extrapolating to a larger distance via the method recommended in Ref. [73]; the latter allows a strong shock, as well as avoiding an uncertainty of a reference length scale (according to K. Plotkin).

More importantly, both plume source models yield only N-like waves, instead of the single-shock followed by a long tail in negative-overpressure phase as expected from recorded field measurement. It must be noted that the real shocks had been built into the method in the analyses with the source model 1, and that, in analyses with source model 2, the real shock may not have been avoided, because the truncated wooden plume model gave a real shock in the near field. The latter was considered unimportant with regard to the prediction of the front shock and the positive phase of the boom. Owing to the lack of a proper plume source model offering features pertinent to underwater studies, the following study adopts an inverse approach.

The Inverse PCBoom Calculation

In this analysis, the propagation code (PCBoom3) was applied in reverse time steps, tracing the ray path upward from the sea level, using the desired/preferred ground signature as input. This procedure has been known to work for many initial boundary-value problems and applies well on PCBoom3. In the present application, the forepart of the F-function in positive phase and the associated rays are unchanged from the original PCBoom3 program; the reverse procedure was employed mainly to the real, negative-phase part of the F-function, using the corresponding negative-phase portion of the Apollo 15 data recorded by Hilton and Henderson [68]. This procedure ought to give an equivalent source next to the flight trajectory that should render the PCBoom3 the ability to reproduce the desired ground signature.

For reasons mentioned earlier, the propagation code cannot be expected to yield exactly the ideal plume source unless an iterative procedure involving the use of an Euler code can be implemented and its convergence proven. The results obtained by this method without the benefit of iterations are presented in Figs 5.3a and 5.3b for two cases, designated as Focus 3 and Carpet 3, respectively. They are for the same trajectory points as used in the focus and carpet booms for Source Models 1 and 2. Thus all flight parameters, surface trace Mach numbers, etc. are the same.

In spite of the limitations and seemingly ad hoc nature of the procedure, the results do produce the expected single-shock, followed by a long, negative-phase over pressure features in each of Figs.5.3a,b. A favorable feature in Fig.5.3a is the retention of the spike-like, high peak characteristics seen from most recorded focus booms. Its appearance should not be too surprising, since it was retained through the use of the Tiegerman-Seebass shock model for the forepart, independently from the inverse procedure.

Grazing Incidence: Post Focus Booms

Whereas the most intense booms from space launches pertain to the focal booms with surface Mach numbers typically not far from 1.1, there are booms generated during the early ascent phase riding along shallow ray paths which reach the ground/sea level at grazing angels with surface Mach number much closer to unity than 1.1. This type of booms are called "post-focus booms" by many on account of their relatively late arrival due to the additional signal traveling time needed on the longer grazing paths.

The boom intensity predicted by the standard propagation method in this case is expectedly low, but the measured over pressure on the ground could be much higher, by virtue of the superboom phenomenon expected to occur about the cut-off point nearby. [We must quickly point out that superboom should not be associated with a post focus event in aircraft sonic boom studies]. Figure 5.4 shows an example of post-focus boom overpressure associated with a grazing ray, calculated by PCBoom3, for which the surface Mach number is 1.05.

Additional Plume Sensitivity Study

To better understand how shape change in an infinitely extended exhaust plume may affect the negative-phase of the sea-level waveforms, S. Cheung performed CFD wave field analyses for three distinct plume-shape changes, using an Euler code in the symmetry plane. For this study, a uniform atmosphere was considered and the acoustic signals were emitted from the vehicle at 70 body lengths from the ground. Three plume geometries and the resulting ground overpressure signatures from the analyses are shown in Figs.5.5a,b, 5.6a,b and 5.7a,b. [Fig.5.5c shows the bow shocks and the Mach-wave system for the plume model of Fig.5.5a] While vastly different ground overpressures result from the three after-body shapes, the one in Fig.5.5a with the milder aft sectional narrowing trend gives an extended negative overpressure phase similar to those of the recorded focus booms. The large positive-phase portion of the waveform, lacking the spike-like peak, in this case is understandable, because this model analyses did not allow trajectory curvature and vehicle acceleration, and therefore features from ray/wave focusing should not be expected.

Conclusions from Exhaust Plume Studies

The foregoing study suffices to indicate the following observations:

(i) The sea-level sonic boom waveform, the negative-phase part in particular, is very sensitive to the near-field input representing the effect of the rocket plume; improved source model resulting from a (uniformly) valid near-field approximation of the exhaust plume effect is essential for solving the as-yet unpredictable signature problem in space launch application.

(ii) Baring those "post-focus booms", computed and measured sea-level sonic boom signatures from rocket space launches to-date all fall in the class of focus booms, involving no "cut-off", i.e. no superboom; on the other hand, whether a superboom wave field may still be found under a focus boom remains to be answered.

(iii) In as much as existing sea-level overpressure signatures from measured records are not believed to pertain to superboom, the data can be directly applied to the ocean surface as input for sonic boom penetration study. This observation lends support to the direct use of the Titan IV signature shown in Fig.3.21b as input for the underwater penetration study.

5.2 The Super-Focus Booms: CFD Study

The standard wave propagation method may also break down where the local sound speed exceeds the horizontal component of the sonic-boom wave speed. The latter situation becomes critical when this location occurs near the ground or sea surface and will result in significant signal intensification according to the super-boom theory. The very same condition is expected to occur during each rocket space launch when sonic boom first reaches the ground level. It represents the strongest among booms reaching the ground/sea level subsequently, and is therefore an important problem to be

investigated for sonic boom impact study, especially for understanding its role in amplifying an already very strong Focus-Boom wave. In addition to several significant wave-field properties brought out by the CFD analysis, the study described below confirms the substantial intensification power of the superboom.

Problem Background

Sonic boom prediction method using standard propagation codes must be implemented with special treatments where ray *focusing* and/or *cut-off* phenomena occur. As noted earlier, the latter represents a limit/boundary between the hyperbolic and elliptic domains (in the Galilean reference frame) that may occur in an atmosphere with sound-speed variability. The phenomenon involving the cut-off has been termed the *superboom* after Hayes [5, 53], for its expected power of signal magnification, although it could well be considered a *special* ray-focusing event occurring in the vicinity of a *caustics*, which happens to be a cut-off (transition) boundary. We shall continue the used of Hayes' term to distinguish it from other focusing phenomena, of which the occurrence do not require the existence of a cut-off boundary.

Whereas, focus booms and superboom may occur independently, in combination, or concurrently (in Coalesce), it is unclear, in the context of the space-launch application, if a genuine superboom can be identified from any of those strongest booms recorded during the ascent phase of rocket space launches. More specifically, the existing information reported in reports and archives [13, 49, 55, 68, 72] do not furnish sufficiently accurate data of those "focus booms" for determining whether the "surface Mach number" is slightly above or below M_A=1. These booms have been accepted as focus booms on the basis of computed results from standard propagation codes [49, 68]. These observations/believes cannot answer, however, the question: whether a slight/moderate change from the standard atmospheric, or from the real atmosphere during a launches, could find the superboom to occur in combination with, or *right underneath*, or preceding, the "focal boom".

The CFD analyses of the superboom problem was undertaken here not only for its expected wave field-amplification feature in general [56, 57] but for answering the above mentioned question concerning its specified role in space-launch sonic boom prediction. Several wave field properties, brought out from the analysis, especially the applicability of a linearized theory, should be extremely helpful for developing an analytical approach to the interaction problem of superboom and wavy ocean.

There is, however, a problem of obtaining the appropriate incident focus-boom data for the input for CFD calculations, since most documented (measured and computed) pertain to the overpressure at the sea level. Owing to the absence of resources for propagation-code utilization that can generate the type of input in question (cf. discussion in Sec. 5.1), we considered an atmosphere which is modified (slightly) from the standard version. This modified atmosphere represents an *analytic continuation* of the standard model to altitude level (slightly) below the sea level; it may be regarded as being resulted from an atmospheric temperature change that raise the standard distribution upward (slightly), or from flying over a region warmer than in the standard model. With this moderate atmospheric change, the measure overpressure signature from a Titan IV test may then be applied (at the upper boundary) as input to the superboom CFD analysis.

In the following, we shall summarize briefly the governing equation system for the CFD problem and the important boundary conditions, followed by a short description of the difference equations and the basic numerical procedures and algorithms. Examples for an incident focus boom and for an incident N-wave are discussed.

Nonlinear Tricomi Equations and Boundary Conditions

Following Hayes [5], the perturbation velocity potential ϕ in the superboom domain is governed by a partial differential equation (PDE) of the same form as the (steady) transonic small-disturbance equation (in standard notations aerodynamics)

$$\frac{\partial}{\partial x}\left[\left(1-M^2\right)U\phi_x-\frac{\gamma+1}{2}\phi_x^2\right]+U\phi_{zz}=0 \tag{5.1}$$

where M is the Mach number $M\equiv U/a(z)$ based on the ambient sound speed *a(z)* assumed to be function of altitude (distance from the ground/sea level). This PDE may also be generalized to allow horizontal time-dependent acceleration effect through a modification in the coefficient $\left(1-M^2\right)$, and through the described condition on the upper boundary. In passing, we note from Ref. [57, 58] that the unsteady effect resulting from horizontal speed change could be significant unless (in physical variables)

$$\frac{1}{U}\left|\frac{dU}{dt}\right|<<\left(\frac{L'}{\Delta}\right)^{1/3}\frac{a}{L'} \tag{5.2}$$

where Δ is a scale height, L' is the reference signature length and a is the sound speed. For space-launch applications, the RHS of (5.2) is typically $(10)^{-1/3}/3\sim 0.27Hz$ so the time-dependent LHS of (5.2) may not appear to be extremely small. This effect, however, is not expected to assume a dominant importance for the present study; the analysis will focus mainly on the influence of the hyperbolic-elliptic transition through cut-off boundary. The acceleration influence may nevertheless enter indirectly through the focus-boom signature prescribed at the upper boundary resulting from vehicle path bending and speed changing on a larger (global) scale.

This PDE can be reduced to a parameter-free, canonical form which embraces the transitional and nonlinear features on an equal footing

$$\frac{\partial}{\partial x}\left[-\tilde{z}\phi_{\tilde{x}}-\phi_{\tilde{x}}^2\right]+\frac{\partial^2}{\partial\tilde{z}^2}\tilde{\phi}=0$$

after rescaling the variables through

$$\tilde{x}\equiv x/L',\qquad \tilde{z}\equiv\left(2\frac{\Gamma_1 L'}{\Delta}\right)^{1/3}\frac{z}{L'} \tag{5.4a,b}$$

$$\tilde{\phi}\equiv\phi\Big/\frac{2}{\gamma+1}\left(2\frac{\Gamma_1 L'}{\Delta}\right)^{2/3}UL' \tag{5.4c}$$

where a linear sound speed decrease with increasing height is assumed and Γ_1 is the ratio of the pressure scale height to the sound-speed scale height

$$\Gamma_1\equiv\frac{\Delta}{a}\frac{\partial a}{\partial z}\approx 0.15$$

for the standard atmosphere. In this nonlinear version of the Tricomi equation, the transition boundary occurs at $\tilde{z}=0$.

Let us consider the problem in which the overpressure $(p-p_*)$ and the horizontal wave speed are known at the height z_* where the sound speed and pressure are a_* and p_*, respectively. Also known are reference surface Mach number and the maximum overpressure ratio

$$M_* \equiv \frac{U}{a_*}, \tag{5.5a}$$

$$\in_* \equiv \max.\left(\frac{p-p_*}{p_*}\right) \tag{5.5b}$$

The upper boundary condition in this case may then be expressed as

$$\widetilde{\phi}_{\tilde{x}} = -\frac{\gamma+1}{2\gamma M_*^2}\left(\frac{\Delta}{2\Gamma_1 L'}\right)^{2/3} \in_* F(\tilde{x}), \tag{5.6a}$$

at

$$\tilde{z} = \tilde{z}_* \equiv \left(2\frac{\Gamma_1 L}{\Delta}\right)^{1/3} \frac{z_*}{L} = \left(M_*^{2-1}\right)\left(\frac{\Delta}{2\Gamma_1 L}\right)^{2/3} \tag{5.6b}$$

where

$$F(\tilde{x}) \equiv \frac{p-p_*}{\max.(p-p_*)} \quad \text{at } z = z_* \tag{5.6c}$$

In upstream,

$$\widetilde{\phi}_{\tilde{x}} = 0, \quad \tilde{x} \to -\infty \tag{5.7}$$

On the ground or the non-wavy ocean surface, an impermeable condition is assumed:

$$\widetilde{\phi}_{\tilde{z}} = 0 \quad \text{at } \tilde{z} = \tilde{z}_{gr} \equiv \left(2\frac{\Gamma_1 L}{\Delta}\right)^{1/3} \frac{z_{gr}}{L'} \tag{5.8}$$

Inspection of this PDE system shows three important parameters entering through the boundary conditions (5.6a,b) and (5.8). Namely,

$$\tilde{z}_{gr}, \quad \in_* \left(\frac{\Delta}{2\Gamma_1 L'}\right)^{2/3}$$

The z-domain where the hyperbolic-elliptic transition feature manifests, corresponds to $\tilde{z} = 0(1)$; it is small compared to scale height Δ but large compared to the signature length L', i.e.

$$\frac{z}{\Delta} = 0\left[\left(\frac{1}{2\Gamma_1}\right)^{1/3}\left(\frac{L}{\Delta}\right)^{2/3}\right] << 1$$

$$\frac{z}{L'} = 0\left[\left(\frac{\Delta}{2\Gamma_1 L}\right)^{1/3}\right] >> 1$$

At the upper boundary $z = z_*$, corresponding to $\tilde{z} = \tilde{z}_*$, where z_* is small compared to the scale height, but may be larger than, or comparable to, the signature length, depending on how close is M_* to unity, i.e.

$$\frac{z_*}{\Delta} = \frac{1 - M_*^2}{2\Gamma_1} << 1, \quad \frac{z_*}{L'} = \frac{1 - M_*^2}{2\Gamma_1 \dfrac{L}{\Delta}} >> 1 \text{ or } << 1$$

Two Examples:

The chief study objective is to examine whether the focus-boom like Titan IV surface overpressure in Fig. 3.21b can be meaningfully used (after being reduced by one half) as input to a superboom wave field in the *extended*, standard atmosphere in which a cut-off boundary can occur. An example of superboom with an incoming N-wave was also studied to exhibit contrast with results from the space launch. The Mach number M_* for Titan IV waveform was taken to be 1.06 which is the same estimate for the surface Mach number M_A of the Titan IV focus-boom, being not very far from M_A=1.03 estimate by Cheng & Lee [39] for the Saturn V-Apollo 17 field measurement, and the M_A=1.146 estimate by K. Plotkin (cf. Sec. 5.1) for Apollo 15 focus-boom. The same M_* is adopted for the case of incident N-wave.

The two sets of parameters, normalized variables, and the upper boundary conditions used in the subsequent calculations are

Set (1) Titan IV focus-boom as incident wave

$$M_* = 1.06, \ \epsilon_* = \frac{1}{2}\frac{8(psf)}{2116.8} = 0.00189$$

$$\frac{\Delta}{L} = 10, \ \Gamma_1 = 0.15, \ \gamma = 1.40, \ L' = 1 \ km$$

$$\tilde{x} = x/L', \ \tilde{z} = (0.311)z/L', \ \tilde{\phi} = (12.4)\phi/UL'$$

Boundary condition at $\tilde{z} = \tilde{z}_* = 1.280$

$$\tilde{\phi}_{\tilde{x}} = 0.0158 F_1(\tilde{x})$$

Set (2) Incident N-wave

$$M_* = 1.06, \ \epsilon_* = \frac{1}{2}\frac{2(psf)}{2116.8} = 0.000473$$

$$\frac{\Delta}{L} = 100, \ \Gamma_1 = 0.15, \ \gamma = 1.40, \ L' = 100 \ m$$

$$\tilde{x} = x/L', \ \tilde{z} = (6.934)z/L', \ \tilde{\phi} = (57.69)\phi/UL'$$

Boundary condition at $\tilde{z} = \tilde{z}_* = 5.943$

$$\tilde{\phi}_{\tilde{x}} = 0.0184 F_2(\tilde{x}).$$

Numerical Methods

The First and Second Order accurate schemes of Engquist and Osher [77] were used to solve numerically the canonical superboom problem. The study was undertaken by M.M. Hafez and E. Wahba at Univ. Calif., Davis.

The First-order scheme

A type-dependent first order scheme is applied to the governing equation (5.3) resulting in

$$\left(\frac{f_{i+\frac{1}{2},j} - f_{i-\frac{1}{2},j}}{\Delta x}\right) + \left(\frac{\bar{f}_{i-\frac{1}{2},j} - \bar{f}_{i-\frac{3}{2},j}}{\Delta x}\right) - \left(\frac{\bar{f}_{i+\frac{1}{2},j} - \bar{f}_{i-\frac{1}{2},j}}{\Delta x}\right) + \left(\frac{\phi_{i,j+1} - 2\phi_{i,j} + \phi_{i,j-1}}{\Delta y^2}\right) = 0 \tag{5.10a}$$

where

$$f \equiv -z\phi_x - \phi_x^2 \tag{5.10b}$$

$$\bar{f} = f \text{ if } \phi_x > -z \tag{5.10c}$$

$$\bar{f} = \frac{1}{2}\phi_x^2 \text{ if } \phi_x < -z \tag{5.10d}$$

In above, all the curly bars over $\tilde{x}$, $\tilde{z}$, and $\tilde{\phi}$ are omitted

The Second-order scheme

A type-dependent second order scheme is applied to the governing equation resulting in

$$\left(\frac{f_{i+\frac{1}{2},j} - f_{i-\frac{1}{2},j}}{\Delta x}\right) + \left(\frac{2\bar{f}_{i-\frac{1}{2},j} - 3\bar{f}_{i-\frac{3}{2},j} + \bar{f}_{i-\frac{3}{2},j}}{\Delta x}\right) - \left(\frac{\bar{f}_{i+\frac{1}{2},j} - \bar{f}_{i-\frac{1}{2},j}}{\Delta x}\right) + \left(\frac{\phi_{i,j+1} - 2\phi_{i,j} + \phi_{i,j-1}}{\Delta y^2}\right) = 0 \tag{5.11}$$

where again

$$\bar{f} = f \text{ if } \phi_x > -z$$

$$\bar{f} = \frac{1}{2}\phi_x^2 \text{ if } \phi_x < -z$$

Linearization of the flux

Due to the non-linearity of the $\left(\frac{1}{2}\phi_x^2\right)$ in the function (f), a linearization method has to be applied to this term. Newton's method is used to linearize $\left(\frac{1}{2}\phi_x^2\right)$, which results in the following linearization expression:

$$\left(\frac{1}{2}\phi_x^2\right)_{new} = \left(\frac{1}{2}\phi_x^2\right)_{old} + \phi_{xold}\left(\phi_{xnew} - \phi_{xold}\right)$$

where ϕ_x and f are evaluated at the mid-segment. The grid used in the numerical solution was generated based on:

$$\Delta x = \Delta y = 0.01$$

Finer grids are used in examples where accurate descriptions are needed.

A block iterative scheme was selected to solve the system of simultaneous algebraic equations. A tri-diagonal solver, based on Thomas' algorithm, is used for inversion along each z-column. Successive sweeps in the x-direction are applied till convergence is achieved (namely, the maximum residual becomes less than 10^{-18}). While the first-order Engquist-Osher (E-O) scheme is known in ensuring a monotone shock transition, the second-order E-O scheme has the merit of avoiding non-physical "expansion shocks". The second-order scheme was used in most examples studied below.

Numerical Results

Solutions to the superboom equation using similar relaxation methods have been presented in Refs. 56-58; these works addressed mainly the problem for incident N-waves, employing numerical algorithms and for parameter sets different from those shown in sets (1) and (2) above. Results from the example for parameter set (1), which employs the "Titan IV focus-boom" as input data on the upper boundary, will first be studied. The solution for parameter set (2) for an incident N-wave pertaining to aircraft booms is examined later; the results will illustrate features in contrast, as well as in common with, the space-launch boom of set (1).

Model of space-launch superboom

The PDE (5.3) was solved with the boundary condition and parameters of set (1), using a measured "Titan IV focus-boom" as input at the upper boundary. As indicated, the analysis intends to model a superboom problem in an (slightly) extended, standard atmosphere to allow occurrence of the cut-off plane near the ground/sea level.* Results were obtained for three ground levels relative to the cut-off/transition plane, $z = z_{gr}$.

Figures 5.8a,b,c show numerical results obtained for (negative of) overpressure signatures at successive heights for three cases with ground level set at z = 0, -0.20, -0.50, using a mesh of $\Delta x = \Delta y = 0.01$. Forgiving at the moment the shortcoming of a shock-capturing algorithm implicitly used here on a rough grid (well known and accepted in CFD community), the solutions do substantiate the expectation for the "virtue" of signal amplification, being particularly evident near the transition plane (z=0, see Figs. 5.8a,b). The smoothness in the ground signature profiles in Figs. 5.8b,c suggests that sonic

* The depth increase called for the extended, standard atmosphere in this case is estimated to be no more than 3 km, comparable to the height of Mt. Wilson in southern California.

boom shock will not reach the ground for $|z_{gr}| \le 0.2$, corresponding to 600 *m* below the cut-off plane in this case. It is unclear, however, if the maximum overpressure near the transition plane may exceed the peak of the input (Titan IV) signature, owing to the uncertainty in the rough-grid accuracy. Curiously, the strong recompression in the ground signature of Fig. 5.8a would suggest an unexpected N-wave like feature, even though the "Titan focus-boom" has only single peak and shock.

These ambiguities are clarified by the results presented in Fig. 5.9 in which the earlier results of Fig. 5.8a are compared with results from the finer grids: $\Delta x = \Delta y = 0.005$ (in dashes), and $\Delta x = \Delta y = 0.0025$ (in dash-dots). Here, the sharpen front shock on the ground attends a peak *more than twice* the peak in the original Titan IV signature, and the recompression suggesting a real shock in Fig. 5.8a disappears into small dispersive wiggles. The focus-boom like space-launch signature is thus seen to be amplified in accord with the superboom theory. The physical reality of the dispersive oscillatory feature following the recompression seen from Fig. 5.9 may be suspect. This feature reveals, in fact, a minor flaw of the Engquist-Osher scheme. This comment is supported further in its application to an example of N-wave in a uniform supersonic flow (not presented here).

The numerically small value of ϵ_* controlling the input at upper boundary in both parameter sets (1) and (2) suggest that the nonlinear term in (5.3) can be important only in the immediate vicinity of the transition boundary z=0. The significance of the *linear* domain, where the superboom wave-field can be described by the Tricomi equation in its original linear version, has been recognized in earlier numerical studies mainly in the context of aircraft sonic booms [56, 57]; the condition for its existence was not as apparent as in the present form. To assess how adequate can be the linearized version of (5.3), we repeat the line-relaxation procedure to (5.3) without the nonlinear term, and compare the results with the corresponding nonlinear solution, using the same grid. The latter has a mesh of $\Delta x = \Delta y = 0.01$ which should suffice for the purpose. The nonlinear solution (in solid curve) and the linear solution (in light dashes) are compared for the case z_{gr}=-0.5 in Fig. 5.10. They are almost undistinguishable with minor differences noticeable only at the lower pressure peaks. The close agreement support the expectation that a linear superboom theory can furnish a useful extension of sonic boom prediction methodology, while analytical and refined numerical analysis, extending the works of Refs. [13, 54, 78] may be needed to treat the non-uniform approximations in the shock vicinity and in approaching the transition (cut-off) line.

Superboom under an incident N-wave

We next examine the superboom wave-field structure under an incident N-wave (from, say, a carpet boom), using the boundary condition and parameters of Set (2). The results of the (normalized, negative) overpressure at different heights computed with $\Delta x = \Delta y = 0.01$ are shown in Figs. 5.11a,b for two cases with the ground lying below the transition plane, i.e. z_{gr}=-0.20, -0.50. While the trend of amplification in approaching the transition line is apparent, the pronounced asymmetry resulting from the much greater amplification of the real shock is noteworthy. The latter feature is in accord with results found for nonlinear calculations of aircraft superbooms, especially with regard to the persistent appearance of the real shock below the transition line where the front shock has disappeared and become a weak compressive wave. Results obtained from finer grids are expected to further substantiate the foregoing observations, and to make the real shock compression sharper and stronger.

In summarizing the CFD superboom study, we conclude that the incident focal boom from space launch can be greatly intensified upon approaching the transition plane, with a significant increase in the peak overpressure. The wave-field structure is affect little by the nonlinearity, except in the vicinities of the transition plane and the shock, where a much finer CFD analysis together with proper implementation of the analytical methods [54, 78] are still needed for the maximum peak pressure determination. [Thus

very intense focal booms observed in field measurement could have been the working of an underlying superboom]. Unlike a space-launch which lacks a prominent rail shock, the latter in the case of an incident N-wave is vastly amplified on the approach to the transition plane and persists even beyond (below) the cut-off line. The more complete study is detailed in subsequent papers by M. M. Hafez and E. Wahba.

6. Conclusions

Underlying the key features in the experiments and analyses are the time-dependent, acoustic source produced by the (weakly-nonlinear) interaction which, in turn, generates *dispersive* waves in a moving frame underwater, with a continuous spectrum of finite bandwidth. In progressing into deep water, these waves disperse into a packet of (quasi) monochromatic, cylindrically spreading wavelets; the result overwhelms the otherwise, primary flat-ocean wave field by virtue of its much slower attenuation rate.

Several different series of laboratory measurements were made during the 6 months of testing. Due to continuing development and improvements in both the data acquisition and other measurement systems, each series of experiments was treated independently; typically the older data was quickly exploited then discarded once the desired changes (improvements) were achieved. This approach provides adequate verification of any questionable results under slightly different experimental conditions (different tank, microphones, wave-generator, projectiles, room geometry etc.) and contributes to the overall robustness of these results. The principal quantity of interest is the maximum peak overpressure associated with the waveform, as this will best allow localization of the region in parameter space with maximum sensitivity to the phenomena.

In spite of the limitations in the experiment designed for a relatively rapid validation of theory, the significant difference in deep water overpressure between wavy and non-wavy surface models are found in accord with the theory. Within the important parameter ranges of the theory, the experiments confirms the dominance of the wave-surface influence in deep water; the results substantiate Sawyers' inverse-square rule for a flat water surface and the cylindrical-spreading rule for a wavy interface in agreement with Cheng & Lee's analysis. Although a detail spectral analysis of the measurements was not made, the crucial spectral data are all contained in the waveforms recorded. Some unique deepwater spectral properties, such as the frequency downshift and the spatial similarity, are already apparent from the waveforms observed.

The original interaction analysis has been extended to calculations for general (non-N) sonic-boom waves and also to treatment of multiple, non-sinusoidal surface wave trains. Of significance is the indication from the examples pertaining to supersonic over-flights that disturbances of 100-130 dB (re 1 μPa) in the 10-40 Hz range are perceivable at depth levels 50-500 m., over a duration of 2-4 sec. The peak over-pressure and frequency are shown to increase markedly with surface Mach number M_A and surface-wave number k, while moderate changes are found with non-alignment of the wave train with the flight track (as long as it is within the progressive-wave domains displayed in Fig. 3.3). Noteworthy among the time-domain waveforms are their common features of the frequency-downshift and the inverse square-root rule in the reduced depth variable kz, for moderate and high k.

Of interest to space launch applications is the example with an incident focus-boom waveform, characterized by a single over-pressure peak and a long, negative-phase portion extending to 1 km. The calculation reveals that *infrasound* in the 1-10 Hz. Range at 100-125 dB (re 1 μPa) is perceivable at depth levels down to 1 km, with a duration 20-40 sec. While the far-field formula and the cylindrical spreading rule are seen working well, the aforementioned high-k scaling rule does not apply to this case with the focus- boom signature as input. The long pulse duration of 20-40 sec. found may increase the exposure period to ambient ocean noise and raise the issue of masking the signals in question. However, based on the 80 dB (re 1 μPa/√Hz) maximum established for the averaged vessel traffic noise, which has been considered the predominant noise source of the ocean [35, 36a], the latter level may be raised to an effective level of 96 dB (re 1 μPa) for the 40 sec noise exposure mentioned, and is therefore still lower than the 100-130 dB level of concern here.

Extensive studies with PCBoom and other propagation codes (Sec. 5) indicate that existing prediction methods, while adequate in predicting the peak over-pressure of a "focus boom", are inadequate for predicting the aft, negative-phase portion of the sea-level signature. The latter was, however, found to be very sensitive to the assumed exhaust-plume geometry, or the near-field source model, but is vital for determining the wave field underwater as well as the superboom occurrence. In the absence of appropriate input data (for the standard atmosphere), the CFD super-boom study employs a (slightly) modified standard atmosphere and shows that a super-boom can occur under a focus boom and significantly amplify its intensity.

With the significant influence of surface waves made evident by the foregoing study and the limitations of the laboratory and analytical models, field experiments remain the critical stage for ascertaining the adequacy of the prediction methodology in question. Equally important is the comparison of estimates derived from the model, tank tests and field measurements with established risk criteria for marine mammal harassment and harm to other endangered species. Apart from lending support to field tests and analyses of risk criteria, analytical and laboratory studies shall be continued to resolve untreated critical issues, to solve newly identified problems, and to assist establishing new assessment guide lines. The following summarizes the unresolved/unsolved problems and research needs under five main categories, which are judged essential toward achieving the program objectives of protecting ocean environment and sea lives.

I. Need for wider parametric and type coverage; graphics and audio

Space-Launch Examples—Available recorded/computed sea-level sonic boom signatures pertinent to modern space-launch operation needs must be included in a more extensive wave-field study.

Wider Parameter Coverage—Ranges of Mach number, surface wave number, wave height, wave-train alignment angle, etc. should be enlarged to allow more realistic representations; an analytical development for high surface- wave-number is included.

Graphic and Audible—Static and cinematic contour plots illustrating wave-field penetration depth and time sequence are needed to reach a wider audience and aid insight; audio play-back in synch with computed wave packet in transit is also expected to help in this respect.

II. Marine mammal response to audio playback

Underwater Experiments with Marine Mammals—Over-pressure signals computed from theory for deep water is broad-cast and directed to a marine mammal species (preferably not too far from the surface on a calm sea) in close range, in an audio play-back experiment under water to observed/record the animal's response to the predicted deep-water sound. The project is to be carried out jointly with marine biologists and will provide data and understanding which may not be obtainable otherwise.

III. Shallow-water response to sonic booms

Non-Wavy Shallow Water—Large parameter domain of a flat, shallow ocean, including the limit of a vanishing depth, must be explored and ascertained. The work will be a joint theoretical and experimental effort.

Wavy Shallow Water—Response to sonic boom in this case has not been analyzed thus far; laboratory investigation is expected to precede theory in this study.

Sediment Boundary Wave Excitation—Studies will include greater varieties in elastic properties and in shear-wave speed distribution, including the singular problem of a vanishing shear-wave speed at the sediment interface; the study will be made jointly with seismic-acousticians; laboratory study in limited scope will be considered.

Near-Surface Wave Field of a Wavy Ocean—The results, not thoroughly delineated thus far, may impact significantly the study of potential physiological harm to a broader animal group, including dolphins and seals.

IV. Non-uniform surface wave train and other laboratory issues

Attenuation and Compactness (Finite Length) of Surface Wave Train—In response to the capillary wave decay observed in the laboratory measurement, a new theory is being developed to address non-uniformity in surface wave train due to attenuation and other shape changes; the analysis multi-scale and Laplace transform technique. Test of theory will be provided by comparison with underwater measurement for laboratory-generated compact wave train.

Laboratory Studies of Making Longer and More Uniform Capillary-Wave train—Efforts include surface-wave generation with blowing fans, and the use of larger projectile and surfactants.

Side-Wall Effect—The effect will be substantially reduced in experiments made in the larger test tank, which has been constructed and will be available.

V. Ariel sonic boom propagation method break-down

Near-Field Data Inadequacy—CFD method will be used to improve full-length modeling of the rocket plume and its near-by wave field to furnish correct input for the propagation code.

Super-Boom Analysis Improvement and Extension—New, appropriate input data at the upper boundary will be generated from a propagation code for the standard atmosphere; a non-dispersive, finite-difference scheme are to be used to avoid unwanted algorithm generated wavy features; grid refinement or shock-fitting treatment shall be used to determined the correct peak over-pressure. Match-asymptotic theory can be used to solve the quasi-linear, super-boom problem; the approach promises an extension for the interaction with a wavy sea surface.

Acknowledgement

The author would like to express his appreciation of the fruitful collaborations and enlightening communications with M. Badiey, A. Bowles, F. K. Browand, L. Carroll, D.M.F. Chapman, S. Cheung, C.S. Clay, F. Desharnais, G. D'Spain, J. Edwards, A. Fincham, C.R. Greene, C. Griffice, M. M. Hafez, R.M. Hicks, R. Kaplan, J. Kunc, Y.G. Li, V. Lang, G. Malcolm, T. Maxworthy, H. Medwin, J. Mendoza, P. Newton, R. Nigbor, K. Plotkin, L. Redekopp, J. Sigurdson and E. Wahba. The work has also received much benefit from discussions with E. Haering, V. Sparrow, R. Sohn, and fellow members of the Southern California Sonic Boom Forum and also with colleagues at the University of Southern California, and the Aerospace Corporation.

The production of this report could not have realized in time without the able assistance of A. Anaya, L. Aragon, M. Patel, M. Penoliar, J. Wong and other AME Department staffs. A good part of this work was produced under the Ocean Sonic Boom Program sponsored by the Environmental Management Division, AF Missile and Space System Center, Los Angeles, through Parsons Engineering Science Subcontract: 738249-3000-00 during July 2000-August 2001. The helpful assistance and valuable service offered by A. Hashad and R. Crisologo and their colleagues in program and contract management are gratefully acknowledged.

Cited References

[1] Gladwin, D. N., Manci, K. M., and Villella, R., "Effect of Aircraft Noise and Sonic Booms on Domestic Animals and Wildlife; Bibliographic Abstracts," Tech. Rept. US Fish & Wildlife Serve National Ecology Res. Center (1988).

[2] Stewart, B. S., Young, R. W., Francine, I. K. and Drawbridge, M., "Monitoring Biological and Geological Effects of Launch-Specific Related Noise and Sonic Boom from Titan IV on 8 March 1991," Huubs-Sea World Res. Inst. Report (1991).

[3] Dept. Transportation Federal Aviation Administration, "Programatic Environmental Impact Statement for Licensing Launches," **vols. I, II**. DOTFAA Associate Administration for Commercial Space Transportation (2001).

[4] Dept. Air Force Material Command, "Environmental Assessment for U.S.A.F. Atmospheric Interceptor Technology Program," Dept. AFMC Headquarter, S & M System Center, Nov. 1997.

[5] Hayes, W. D. "Sonic Boom." *Annual Rev. Fluid Mech*., **vol. 3**, pp. 269-190 (1971).

[6] Hunter, J. and Keller, I. B., "Weakly Nonlinear High Frequency Waves," Comm. Pure Appli. Math. Math. (1983); also see "Weak Shock Defraction," *Wave Motion*, **vol. 6**, pp. 79-89 (1984) by same authors.

[7] Guiraud, J. P., "Acoustic geometrique, bruit ballistique desavions supersoniques et focalisation," *J.Mecanique*, **vol. 4**, pp. 215-267 (1965).

[8] Walkden, F., "The Shock pattern of Wing-Body Combination Far From the Flight Path," Aeronautical Quarterly, **vol. 9**, pp. 164-194 (1958).

[9] Carlson, H. W. and Maglieri, D. I., "Review of Sonic-Boom generation Theory and Prediction Methods," *J. Acoustical Soc. America*, **vol. 51**, No. 2 (pt. 3), pp. 675-685 (1972).

[10] Darden, C. M., (ed.) "Status of Sonic Boom Methodology and Understanding," *NASA Conf. Pub. 3027* (1988).

[11] Thomas, C. L., "Extrapolation of Sonic Boom Pressure Signature by the Waveform Parameter Methods," NASA TN D-6832 (1972).

[12] Onyeonwu, R. C., "A Numerical Study of Effects of Aircraft Maneuvers on the Focusing of Sonic Boom," Inst. Aerospace Studies, Univ. Toronto, UTIAS Report 192 (1973).

[13] Plotkin, K. I., "Evolution of a Sonic Boom Focal Zone Prediction Model," Wyle Research Lab. Report WR 84-43, Feb. (1985).

[14] Sawyers, K. H., "Underwater Sound Pressure from Sonic Boom," *J. Acoust. Soc. Amer*., **vol. 44**, no. 2, pp. 523-524 (1968).

[15] Water, J., "Penetration of Sonic Energy into the Ocean: An Experimental Simulation," *Noise & Vibration Control Engineering* (ed. M. Croker), *Proc. Noise Control Conf. Purdue Univ*., July 11- 16, 1971, pp. 554-557 (1971).

[16] Intrieri, P. F. and Malcolm, G. N., "Ballistic Range Investigation of Sonic-Boom Overpressure in Water," *AIAA J*., **vol. 11** , no. 4, pp. 510-516 (1973).

[17] Cook, R., "Penetration of a Sonic Boom into Water," *J. Acoustic Soc. Am*., **vol. 47**, no. 5, pt. 2, pp. 1430-1436 (1970).

[18] Sparrow, V. W., "The Effect of Aircraft Speed on the Penetration of Sonic Boom Noise into Flat Ocean," *J. Acoust. Soc. Am*., **vol. 97**, no.1, pp. 159-162 (1995).

[19] Sparrow, V. W., and Ferguson, T., "Penetration of Shaped Sonic Boom Noise into a Flat Ocean," *AIAA Paper 97 -0486* (1997).

[20] Bowles, A. E., "Effects of Sonic Booms on Marine Mammals: Problem Review and Recommendation Research," Proc. 1995 NASA Sonic Boom workshop, *NASA Conf. Pub. 3335* (1995).

[21] Bowles, A. E. and Stewart, B., "Disturbances to the Pinnipeds and Birds of San Miguel Island, 1979- 1980", *in Potential Effect of Space Shuttle Sonic Booms on Biota and Geology of the Calif. Channel Islands*, (ed. J.R. Jehl and C.F. Cooper) Tech. Rep. 80-1 by San Diego State Univ., Hubbs-Sea World, Res. Inst. and USAF Space Div. (1980).

[22] Stewart, B., Thorson, P. H., Francine, J. K., "Behavior Response of Pinnipeds and Selected Avifauna at Vandenberg AFB and the Northern Calif. Channel Islands to Rocket Noise and Sonic Boom During Launch of a Titan IV k-22 Rocket SLC-4E, Vandenberg AFB, on May 12, 1996", Huubs-Sea World Res. Inst. Tech. Report 96-264: 1-68 (1996).

[23] Richardson, W. I., Greene, C. R., Ir., Ma1me, C. I., and Thomson, D. H., *Marine Mammals and Noise*, Academic Press (1995) pp. 15-86, 525-452.

[24] Richardson, W. I. & Wursig, "Influence of Man-made Noise and Other Human Actions on Cetacean Behavior," *Marine Freshwater Behavior Physiology*, **vol. 29** (1997): p. 188 (summarizing literature).

[25] National Res. Council Ocean Study Board Committee. "Low Frequency Sound and Marine Mammals." NRC Report 1992, **vol. viii**. (1992)

[25a] Au, W. W. L., Nacktingall, P. E. and Pawloski, J. L., "Acoustic Effects of the ATOC Signals (75 Hz, 195 dB) on Dolphins and Whales", *J. Acoust. Soc. Am.*, **vol. 101**, no. 5, pp. 2973-2977 (1997).

[25b] Awbrey, F. T., Thomas, J. A. and Kastelein, R. A., "Low-Frequency Underwater Hearing Sensitivity in Belugas", *Delphinapterus Leucas, J. Acoust. Soc. Am.*, **vol. 84**, no. 6, pp. 2273-2275 (1988).

[26] Natural Resource Defense Council. *Sounding the Depths: Supertankers, Sonar, and the Rise of Undersea Noise*, NRDC Report (1999).

[26.a] Information on a typical mass stranding of beaked whales and other cetaceans in Greece and the Bahamas received through Internet Mail Service (courtesy of J. Edwards and A. Hashad): (1) Message (03/23/00) from A. Frantzis <afrantzis@otenet.gr> to MARMAM <mannam@univ.ca>; (2) Message (03/23/00) from K. Balcomb and D. Claridge, Bahamas Marine Mammal Survey. <bmrns@oii.net> to M. Braynen, Director of Fisheries, Nasau, Bahamas, and B. R. Gisiner, ONR; (3) Letter (03/21/00) Wetzler <awetzler@nrdc.org> to R. Danzig, Secretary of the Navy, S. Preston, Dept. Navy Council, and I. Sustersic, ONR on L W AD Sea Test.

[27] Potter, I. R., *Environment and Development*, **3**, no. 2, 47-62 (1994)

[28] ARPA, NOAA and State of Hawaii, "Final Environmental Impact Statement for the Kauai Acoustic Thermometry of Ocean Climate Project and its Associated Marine Mammal Research Program," (1995); ARPA NOAA and Univ. Calif., San Diego, "Final Enviro. Statement for California Acoustic Thermometry of Ocean Climate Project and Its Associated Mammal Res. Program," (1995), **vols. I, II**.

[29] Cheng, H. K. and Lee, C. J., "Sonic Boom Noise Penetration Under a Wavy Ocean: Part I Theory," Univ. Southern Calif. Dept. Aerospace & Mechanical Eng., *USC AME Report 11-11-00* (2000); documented on web site <http://www-bcf.usc.edu/-hkcheng>.

[29a] Cheng, H. K. and Lee, C. J., " Sonic Boom Noise Penetration Under a Wavy Ocean: Theory", Manuscript completed for submission for journal publication (2002).

[30] Cheng, H. K., Lee, C. J., and Edwards, J. R., "Sonic Boom Noise Penetration Under a Wavy Ocean: Part II Examples and Extension", *USC AME Report 4-4-2001* (2001) (Attachment I of this report).

[31.a] Cummings, W. C. and Thompson, P. 0., "Underwater Sounds from the Blue Whale, *Baleanoptera Musculus*," *J. Acoust. Soc. Am*., **vol. 50**, no. 4 (part 2), pp. 1193-1198 (1971)

[31.b] Frankel, A. S. and Clarke, C. W., "Results of Low-Frequency Playback of M-sequence Noise to Humpback Whales, Megaptera Novaeangliae, Hawaii," *Can. J. Zool*., **vol. 76**, pp. 521-535 (1998).

[32.a] D'Spain, G. L., Kuperman, W. A., Hodgkiss, W. S. and Berger, L. P., "3-D Localization of a Blue Whale," Univ. Calif. Scripps Inst. Oceanography, Marine Physical Lab Tech. Memo. 447: MPL-U-87/95 (1995).

[32.b] McDonald, M. A. and Fox, C. G., "Passive Acoustics Methods Applied to Fin Whale Population Density Estimation," *J. Acoust. Soc. Am*., **vol. 105** (5), pp. 2643-2651 (1999).

[33] Fichter, George S., "Whales and Other Marine Mammals," Golden Press (1990).

[34] Cardwardine, M., Hoyt, E., Fordyce, R. E., Gill, P., "Whales, Dolphins and Porpoise," The Nature Company Time Life Books & Weldon Owen Pty Ltd., Sydney (1998).

[35] Wenz, G. M., "Acoustic Ambient Noise in the Ocean: Spectra and Sources," *J. Acoust. Soc. Am*., **vol. 34**, no. 12, pp. 1936-1956 (1962).

[36.a] Urick, R. J., *Principle of Underwater Sound*, 3rd ed. McGraw-Hill (1983); also see same author, *Ambient Noise in the Sea*, Peninsula Publ. Los Altos, CA .

[36.b] D'Spain, G. L., Hodgkiss, W. S. and Edmonds, G. L., "Energetics of the Deep Ocean's Infrasonic Sound Field," *J. Acoust. Soc. Am*., **vol. 89**, no. 3, pp. 1143-1158 (1991).

[37] Cheng, H. K., and C. I. Lee, "Submarine Impact of Sonic Boom: A Study Comparing and Reconciling Results from Two Prediction Approaches," Proc. NOISE CON 97, Penn. State Univ. Park, Penn. June 15-17, 1997, pp. 399-404 (1997).

[38] Cheng, H. K., Hafez, M. M., Lee, C. I., and Tang, C. Y., "Assessment on an Improved Theory for Further Program Development of Sonic-Boom Prediction and Submarine Impact Study," Final Report submitted to A.F. Armstrong Labs., OEBN Noise Effect Branch, by HKC Research.

[39] Cheng, H. K. and Lee, C. J., "A Theory of Sonic Boom Noise Penetration Under a Wavy Ocean," *AIAA paper 98-2958* (1998).

[40] Medwin, H., Helbig, R. A. and Hagy, J. D., "Spectral Characteristics of Sound Transmission Through the Rough Surface", *Acoust. Soc. Am.* **vol. 54, no. 1**, pp. 99-109 (1973)

[41] Medwin, H. and Clay, C. S.. *Fundamentals of Acoustical Oceanography,* Acad. Press, San Diego (1998)

[41a] Clay, S.C. and Medwin, H, *Acoustical Oceanography*, John Wiley & Son (1977)

[42] Rochat, J. L. and Sparrow, V. W., "Two-DimensionaI Focusing of Sonic Boom Noise Penetration and Air-Water Interface," *AIAA J*., **vol. 35**, no. 1, pp. 35-39 (1997).

[43] Sochaki, I. S., George, I. H., Ewing, R. E., and Smithson, S. B., *Geophysics*, **vol. 56**, no. 2, pp. 168-181 (1991).

[44] Desharnais, F. and Chapman, D. M. F., "Underwater Measurement and Modeling of a Sonic Boom," Abstract in *J. Acoust Soc. Am*., **vol.104**, no. 3, pt. 2, p. 1848 (1998).

[45] Sohn, R. A., Vernon, F. Hildebrand, J. A. and Webb S. C., "Field Measurement of Sonic Boom Penetration into the Ocean," *J. Acoust. Soc. Am*. **Vol. 107**, pt. 6, pp. 3073-3082 (2000).

[46] Miles, J., The Potential Theory of Unsteady Supersonic Flow, pp. 1-17,18-38 (1959).

[47] Ashley, H. and Landahl, M., Aerodynamics of Wings and Bodies, Addison-Wesley Pub. Co. (1968).

[48] Landau, L. D. and Lifshitz, E. M., *Fluid Mech*. pp. 268-269, Pergaman Press (1959).

[49] Holloway, P. E., Willbold, G. A, Jones, J. H., Garcia, F. and Hicks, R. M., "Shuttle Sonic Boom-Technology and Predictions," *AIAA paper 73-1039* (1973); also see Baize, D. G. (ed.) Proc. NASA High-Speed Research Program: Sonic Boom Workshop, **vol. I**, NASA Conf. Pub. 3335 (1996).

[50] Munk, W., Worcester, P. and Wunsch, C., *Ocean Acoustic Tomography*, Cambridge Univ. Press (1995).

[51] Wijngaarden, L. van, “One Dimensional Flow of Liquids Containing Small Gas Bubbles," *Annual Rev. Fluid Mech*., **vol. 4**, pp. 369-396 (1972).

[52] Axel, R. M., and Newton, P. K., "On the Interaction of Shock with Dispersive Waves: I. Weak Coupling Limit," submitted to the *J. Pure and Applied Math*.

[53] Hayes, W.D., "Similarity Rules for Nonlinear Acoustic Propagation Through a Caustic," 2nd Conf. Sonic Boom Research, NASA SP-180, pp. 165-172 (1969).

[54] Gill, P. M., and Seebass, A. R., "Nonlinear Acoustic Behavior at a Caustics: An Approximation Solution," *AIAA Progress in Astr. and Aero*., ed. H.T. Negamatsu, MIT Press (1975).

[55] P1otkin, K. I., Downing, M. and Page, I. A., "USAF Sing1e-Event Sonic Boom Prediction Model: PCBoom 3," *NASA High Speed Res. Program Sonic Boom Workshop*, NASA Res. Conf. Pub. 3279, pp. 171-184 (1994).

[56] Cheng, H. K., Lee, C. J., Hafez, M. M. and Tang, C. Y., "Focused Sonic Boom in a Non-Isothennal Atmosphere as a Mixed Hyperbolic-El1iptic, Nonlinear 3-D Problem," *Proc. 2nd Asian CFD Conf*., Tokyo Univ., Tokyo, Japan (12/15/96-12/18/96) (1996).

[57] Cheng, H. K., and Hafez, M. M., "Analysis and Numerical Simulation of the Superboom Problem," in *Frontier of Computational Fluid Dynamics*, ed. D. A. Cauhey and M. M. Hafez pp. 241-258 (1998).

[58] Cheng, H. K. and Lee, C. I., "On Superboom Wave-field Under Vehicle Acceleration," *AIAA paper 98-2691* (1998).

[59] Helstrom, C. W., *Statistical Theory of Signal Detection*, Chapter 2, Noise, pp. 30-75 Pergaman Press (1968).

[60] Tolstoy, I. and Clay, C. S., *Ocean Acoustics*, Chapter 7, pp. 243-275, Am. Inst, Physics (1966).

[61] Lighthi11, M. J., "Higher Approximations," *General Theory of High-Speed Aerodynamics*, pp. 345-489 ed. W.R. Sears, Princeton Univ. Pres (1954).

[62] HKC Research, “A Proposal for Experimental and Theoretical Investigations of Ocean Sonic Boom Propagation”, submitted to AF JMC Environmental Management (2000).

[63] Munk, W. H., “Waves of the Sea”, *Encyclopedia Britannica*, ed. 1956, **vol. 23**, pp. 442-444 (1956).

[64] Bascom, W., *Waves and Beaches*. Educational Services, Inc. (1964)

[65] Pierce, A. D., *Acoustics*, Acoustical Soc. America, pp. 75-82 (1994)

[66] Stoll, R. D., *Sediment Acoustics*, Lecture Notes in Earth Sciences, Springer Verlag (1989).

[67] Godin, O. A. and Chapman, D. F. M., “Dispersion of Interface Waves in Sediments with Power-Law Shear-Speed Profiles, II: Exact and Approximate Analytical Results”, submitted to *J. Acoust. Soc. Am*., (1999).

[68] Hilton, D. A., and Henderson, H. R., "Measurements of Sonic Boom Overpressure from Apollo Space Vehicles", *J. Acoust. Soc. Am*., **vol. 56**, no. 2, pp. 323-328 (1974).

[69] Kinsler, L. E., Frey, A. R., Coppens, A. B, and Sanders, J. V. , *Fundamental of Acoustics*, 3rd, ed., Wiley (1982).

[70] Badiey, M., Cheng, A. H. D. and Mu, Y., "From Geology to Geo-acoustics – Evaluation of Biot-Stoll Sound Speed and Attenuation for Shallow Water Acoustics", *J. Acoust. Soc. Am.*, **vol. 103**, no. 1, pp.309-320 (1998).

[71] Hamilton, E. L., "Elastic Properties of Marine Sediments", *J. Geophysical Research*, **vol. 76**, pp. 579-604 (1971).

[72] Plotkin, K. J. "PCBoom3 Sonic Boom Prediction Model – Version 1.Oe", Wyle Research Report WR 95-22E (1998).

[73] Hick, R. M., Mendoza, J. P. and Thomas, C. L., "Pressure Signatures for the Apollo Command Module and the Saturn V Launch Vehicle with a Discussion of Strong Shock Extrapolation Procedures", NASA Ames Res. Center, TM X-62, 117 (1972).

[74] NASA/MSFF (1965).

[75] Jarvinen, P. O. and Hill, J. A. F., "Universal Model for Under Expanded Rocket Plumes in Hypersonic Flow", Proc. 12th JANNAF Liquid Meeting, Las Vegas, Nevada (1970).

[76] Tiegerman, B., "Sonic Booms of Drag-Dominated Hypersonic Vehicles", Ph.D. Thesis, Cornell Univ. (1975).

[77] Engquist, B. and Osher, S., "One-Sided Differential Equation for Nonlinear Conservative Laws", *Mathematics of Computation*, **vol. 36**, pp. 321-352 (1981).

[78] Fung, K. Y., "Shock Wave Formation at a Caustic", *SIAM Journal of Appl. Math.*, **vol. 39**, no. 2, pp. 355-371 (1980.

Captions of Figures

Fig. 3.1 Schematic representation of the interaction problem, showing variables and quantities used in the analysis.

Fig. 3.2 Sketch illustrating the sonic boom impact zone in a horizontal reference plane, with surface-wave crests represented by thin solid lines. The two sets of coordinates (x, y) and (x′, y′) fixed to the moving frame, with Λ and ψ identified with the local swept angle of the surface impact zone and the non-alignment angle of the surface-wave vector, respectively.

Fig. 3.3 The boundaries in the Λ-ψ realm enclosing the cylindrical-spreading domains for four surface Mach numbers M_A = 1.05, 1.5, 2.0, and 3.0, in which the surface-wave interaction effects attenuates according to the inverse square-root rule.

Fig. 3.4 Semi-analytical integrated results of real and imaginary parts of the normalized contribution to the synchronized surface pressure $\hat{p}_2(x', 0)$ for N-wave at M_A = 1.821, k=4.

Fig. 3.5 Real and imaginary parts of the Fourier transform of $\hat{p}_2(x', 0)$ for N-wave with M_A = 1.821, k=4 and their comparison with exact, analytic results.

Fig. 3.6 Real and imaginary parts of the synchronized surface pressure $\hat{p}_2(x', z)$ for N-wave with M_A = 1.821, k=4 at depth level z=0.5, and their comparison with corresponding far-field solutions.

Fig. 3.7 The real and imaginary part of $\hat{p}_2(x', z)$ at depth level z=2.5, with conditions otherwise same as in the preceding figure.

Fig. 3.8 Time-domain waveforms for overpressure at the reference surface z=0 produced by an incident N-wave at M_A = 1.821, k=4 for computed maximum surface slope, δ = 0.02, from the flat surface (in dashes), from the surface-wave interaction effect (dash-dot curve for δ = 0.02), and from the sum of the two (solid curve).

Fig. 3.9 Time-domain waveforms of overpressure at depth level z=0.5, with conditions otherwise same as in preceding figure.

Fig. 3.10 Time-domain waveforms of overpressure at depth level z=2.5, with conditions otherwise same as in preceding figure.

Fig. 3.11 Real and imaginary parts of the Fourier transform of $\hat{p}_2(x', 0)$ for N-wave with M_A = 1.5, k=4, and their comparison with corresponding results from the general numerical code, as a test of the program.

Fig. 3.12 Real and imaginary parts of $\hat{p}_2(x', z)$ at depth level z=2.5 for N-wave with M_A = 1.5, k=4, with conditions otherwise same as in preceding figure, and comparison with results from the general code, as a test of the code accuracy.

Fig. 3.13a,b Example of underwater time-domain overpressure waveform produced by N-wave with M_A=1.5, surface-wave number k=4, maximum wave slope δ=0.025, sea-level signature length L'=300ft., and maximum sea-level overpressure 2 psf, at two depth levels: $z'L'$=150ft and $z'L'$=1500ft.

Fig. 3.14a,b Example of underwater overpressure waveform produced by N-waves with M_A = 1.88, k=16 at two depth levels, with conditions otherwise same as in the preceding figure.

Fig. 3.15a,b Example of underwater overpressure waveform produced by N-waves with M_A = 2.38, k=16 at two depth levels, with conditions otherwise same as in the preceding figure.

Fig. 3.16a Example of N-wave interacting with surface-wave train: overpressure time-domain waveform with M_A = 2.38, k=16, δ=0.025, at depth levels z=2.5, for Λ=0, ψ=0.

Fig. 3.16b Overpressure time-domain waveform at z=2.5, for Λ=0, ψ=30 deg.; conditions otherwise same as in preceding figure.

Fig. 3.16c Overpressure time-domain waveform at z=2.5, for Λ=-30 deg., ψ=30 deg.; conditions otherwise same as preceding figure.

Fig. 3.17a Example of sonic boom interacting with a "cross sea" (multiple wave trains with different non-alignment angles): overpressure time-domain waveform at depth level z=2.5 in the presence of two wave trains (Λ, ψ) = (0, 0) and (Λ, ψ) = (0, 30 deg.); conditions otherwise same as in Figs. 16x.a and 16x.b.

Fig. 3.17b Example of sonic boom interacting with a "cross sea": overpressure time-domain waveform at depth level z=2.5 in the presence of two wave trains (Λ, ψ) = (0, 30 deg.) and (Λ, ψ) = (0, -30 deg.).

Fig. 3.18 Example illustrating sea-floor influence on underwater overpressure waveform: N-wave incident upon a flat interface. In this examination, the depth level z (distance from the interface) is fixed at z=0.5 (one half of the signature length L'), while the channel depth ratio takes on several values $h/L' = 0.5$ thru ∞.

Fig. 3.19 Example of sonic boom disturbance penetrating into shallow water in which sediment boundary wave is not excited. The normalized, maximum overpressure is 0.33 and the channel depth ratio is $h/L' = 2.0$; the density and sound speeds of water and sediment material are listed with the figure. For this set of properties, sediment-boundary wave cannot be excited unless $1.33 < M_A < 1.44$. The waveform shown for the mid channel for M_A=1.5 indicates no sign of resonance, as expected. (a) overpressure on water surface, (b) overpressure at mid channel (z=-1).

Fig. 3.20 Example of sonic boom disturbance penetrating into shallow water in which sediment boundary wave is excited. Conditions same as in preceding figure except M_A=1.36, fallen within the resonance condition $1.33 < M_A < 1.44$. (a) overpressure on water surface, (b) overpressure at mid channel, and (c) overpressure on sea floor.

Fig.3.21 Representative sonic booms recorded at sea level during the earliest phase of rocket space launch: (a) Apollo 17 Ascent, (b) Titan IV Ascent, (c) Apollo 15 Ascent.

Fig. 3.22 Overpressure waveform at three depth levels according to the flat-ocean (Sawyers) model based on the sea-level overpressure signature from the Apollo 17 ascent record: (a) sea level, (b) z=0.156 (1,000ft.), and (c) z=0.776 (5,000ft.).

Fig. 3.23a Example of sonic boom from a rocket space launch interacting with a well aligned surface-wave train ($\Lambda=\psi=0$) assuming M_A=1.08, k=64, L'=1 km and a sea-level overpressure same as one recorded for Titan IV launch. Predicted overpressure time-domain waveform at depth level z=1/8, assuming maximum surface-wave slope δ=0.025.

Fig. 3.23b Predicted overpressure time-domain waveform at depth level z=1/4; conditions otherwise same as in Fig. 3.23a.

Fig. 3.23c Predicted overpressure time-domain waveform at depth level z=1/2; conditions otherwise same as in Fig. 3.23a.

Fig. 3.23d Predicted overpressure time-domain waveform at depth level z=1; condition otherwise same as in Fig. 3.23a.

Fig. 3.24a Example of sonic boom from a rocket space launch interacting with a well aligned surface-wave train ($\Lambda=\psi=0$) assuming k=16; conditions otherwise same as in Fig. 3.23a. Predicted overpressure time-domain waveform at depth level z=1/8.

Fig. 3.24b Predicted overpressure time-domain waveform at depth level z=1/4; conditions same as in Fig. 3.24a.

Fig. 3.24c Predicted overpressure time-domain waveform at depth level z=1/2;conditions same as in Fig. 3.24a.

Fig. 3.24d Predicted overpressure time-domain waveform at depth level z=1; conditions same as in Fig. 3.24a.

Captions of figures 4.1 through 4.20 are furnished with each figure cited in Sec. 4.

Fig. 5.1 Sea-level overpressure waveform calculated by PCBoom3, using Plume Source Model 1: (a) Focus Boom , M_A=1.146, (b) Carpet Boom, M_A=1.167.

Fig. 5.2 Sea-level overpressure waveform calculated by PCBoom3, using Plume Source Model 2: (a) Focus Boom , M_A=1.146, (b) Carpet Boom, M_A=1.167.

Fig. 5.3 Sea-level overpressure waveform calculated by PCBoom3, using source model via an inverse approach (a) Focus Boom, M_A=1.146, (b) Carpet Boom, M_A=1.167.

Fig. 5.4 Sea-level overpressure waveform calculated by PCBoom3, using Plume Source Model 1: "Post Focus Boom", M_A=1.05 (via grazing ray).

Fig. 5.5 Plume-shape sensitivity study, assuming axi-symmetric wave-field in uniform supersonic flow. Plume shape A: (a) Assumed rocket and plume geometry, (b) Sea-level overpressure, (c) Bow shock and wave-field.

Fig. 5.6 Plume-shape sensitivity study, assuming axi-symmetric wave-field in uniform supersonic flow. Plume shape B: (a) Assumed rocket and plume geometry, (b) Sea-level overpressure.

Fig. 5.7 Plume-shape sensitivity study, assuming axi-symmetric wave-field in uniform supersonic flow. Plume shape C: (a) Assumed rocket and plume geometry, (b) Sea-level overpressure.

Fig. 5.8 CFD Study of intensification of a focus boom in a superboom wave-filed in a modified standard atmosphere, using incident waveform inferred from recorded (Titan IV) sea-level signature. (Negative) overpressure at successive heights (z-levels) are plotted for cases in which: (a) sea-level and transition (cut-off) plane coincide, z_{gr}=0, (b) transition plane occurring above sea level, z_{gr}=-0.20, (c) transition plane occurring at a higher level above the ground, z_{gr}=-0.50. The mesh size is $\Delta x = \Delta y = 0.01$.

Fig. 5.9 Results of grid refinement for overpressure at different heights for the case in which the sea-level and transition plane coincide z_{gr}=0. Three mesh sizes were used $\Delta x = \Delta z = 0.01,\ \Delta x = \Delta z = 0.005,$ and $\Delta x = \Delta z = 0.0025.$

Fig. 5.10 Comparison of nonlinear and Linear calculations of superboom wave-field for the case in which z_{gr}=-0.50, showing dominance of the linear (Tricomi) regime for the superboom occurring in this example of a rocket space launch.

Fig. 5.11 Example of intensification of an incident N-wave in the superboom wave-field occurring at surface Mach number M_A=1.05 for two cases: (a) transition plane occurring above sea-level, z_{gr}=-0.25, (b) transition plane occurring at a higher level, z_{gr}=-0.50. Note greater amplification occurs for the real shock.

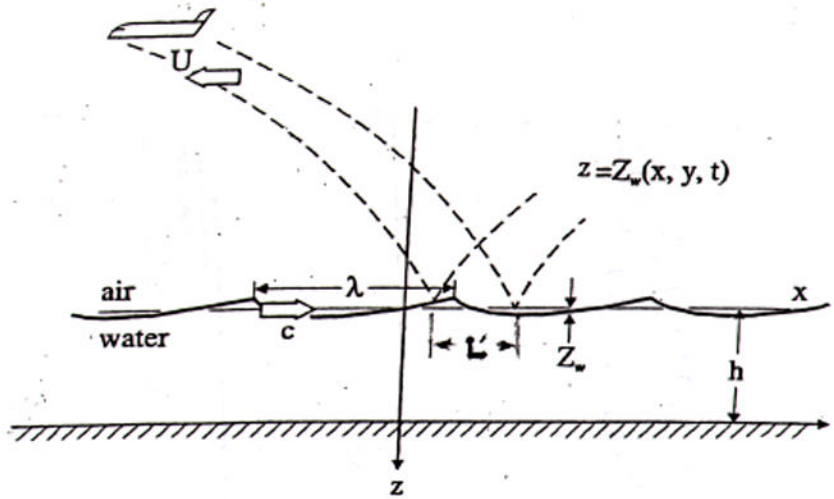

Fig. 3.1

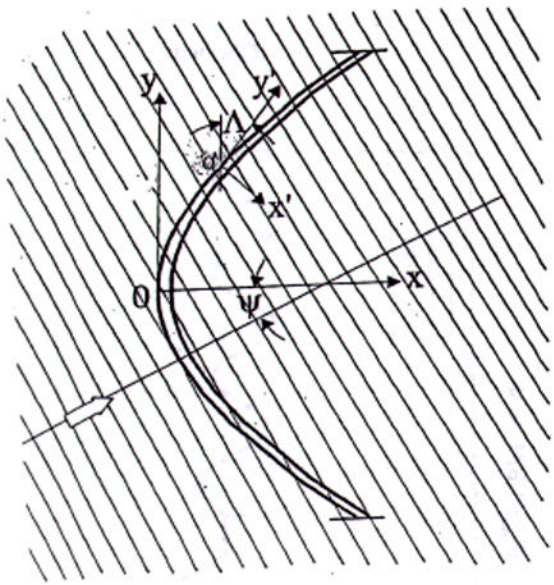

Fig. 3.2

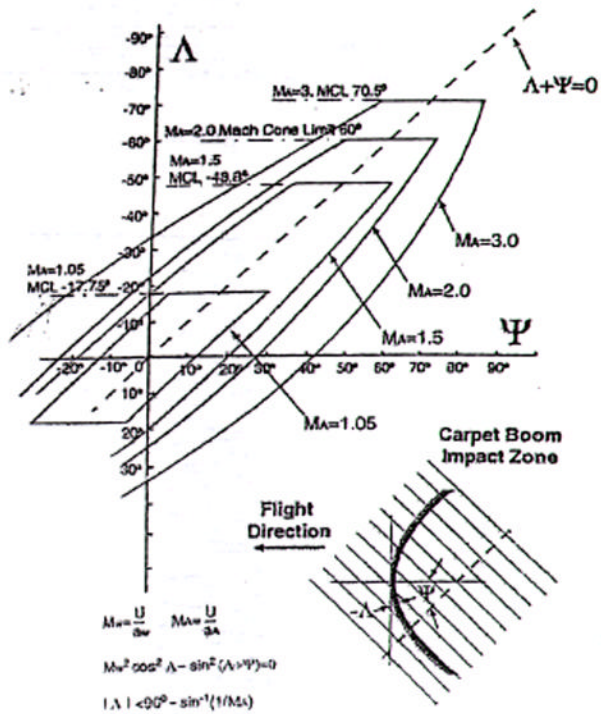

Fig. 3.3

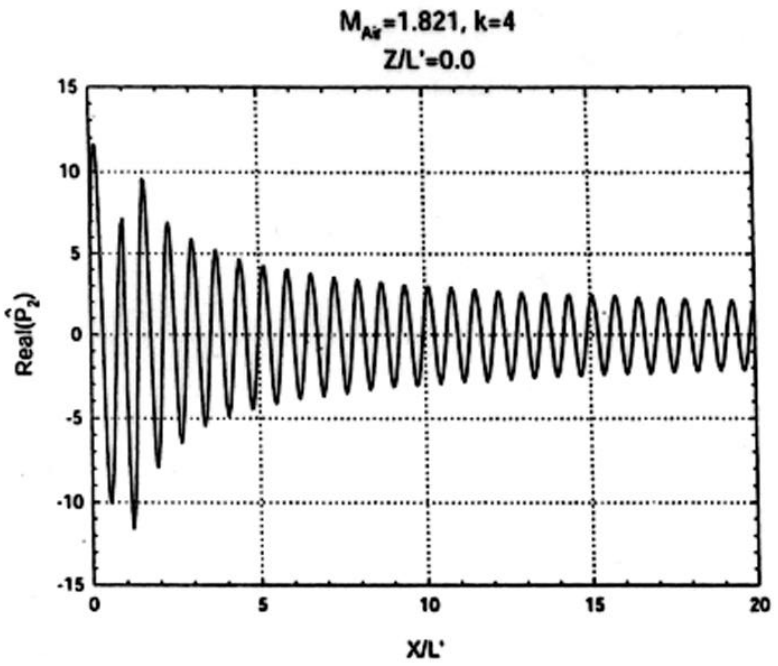
M_{Air}=1.821, k=4
Z/L'=0.0
Real($\hat{P}_2$)
X/L'

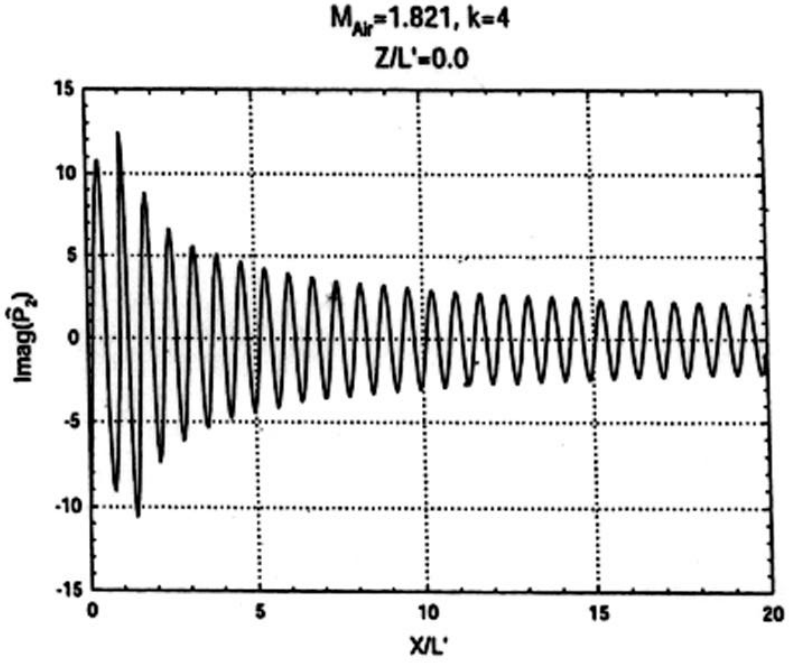
M_{Air}=1.821, k=4
Z/L'=0.0
Imag($\hat{P}_2$)
X/L'

Fig. 3.4

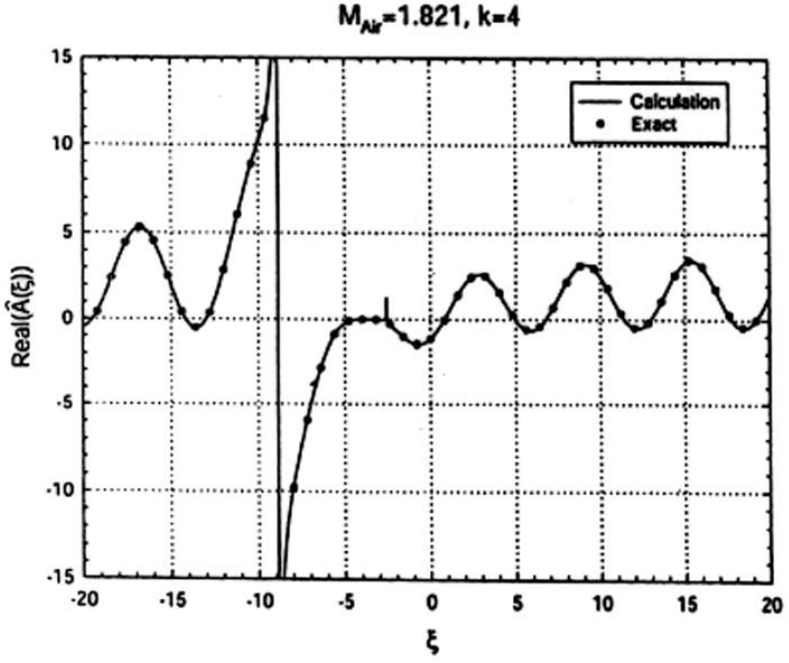
M_{Air}=1.821, k=4
Calculation
Exact
Real($\hat{A}(\xi)$)
ξ

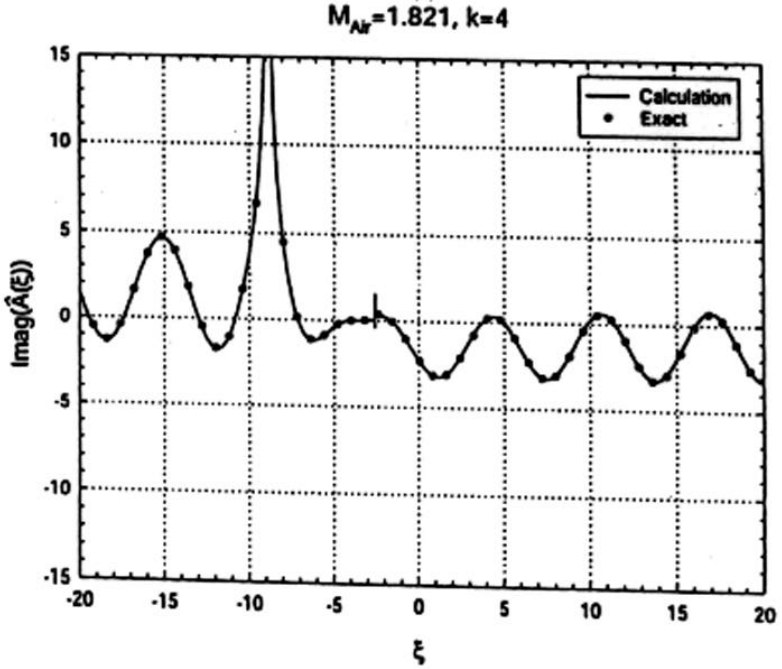
M_{Air}=1.821, k=4
Calculation
Exact
Imag($\hat{A}(\xi)$)
ξ

Fig. 3.5

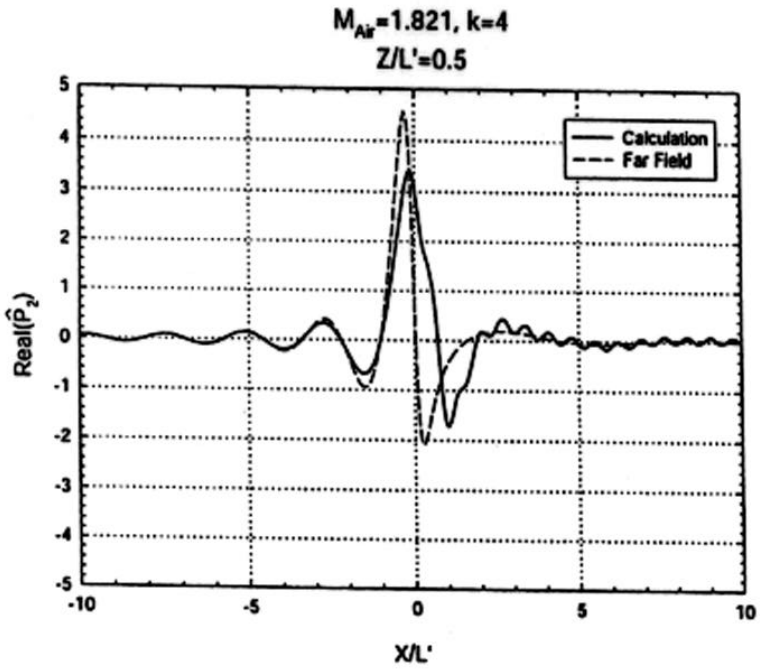
M_Air=1.821, k=4
Z/L'=0.5
Calculation
Far Field
Real(P̂2)
X/L'

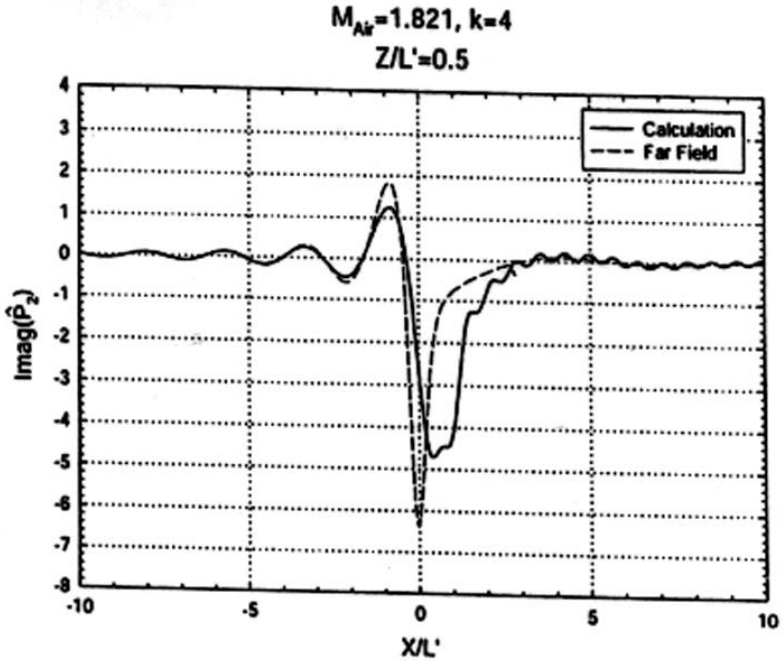
M_Air=1.821, k=4
Z/L'=0.5
Calculation
Far Field
Imag(P̂2)
X/L'

Fig. 3.6

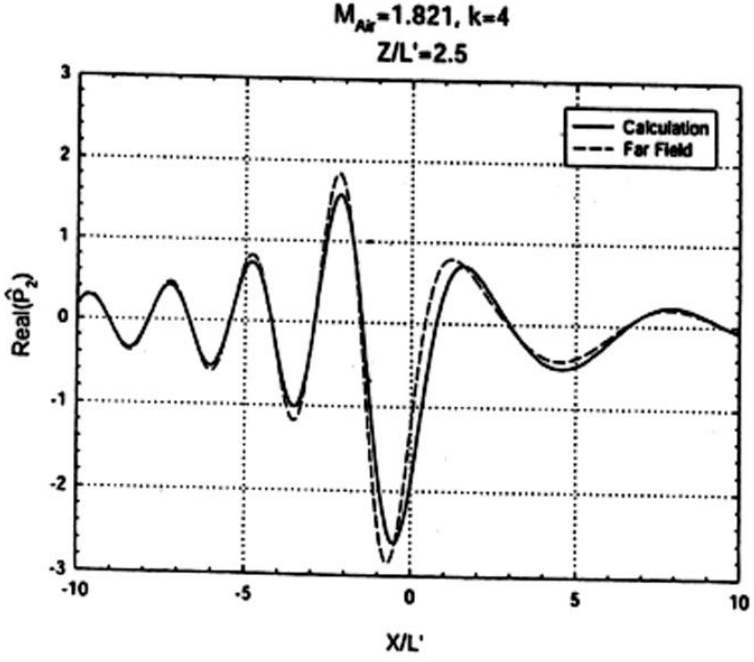
M_Air=1.821, k=4
Z/L'=2.5
Calculation
Far Field
Real(P̂2)
X/L'

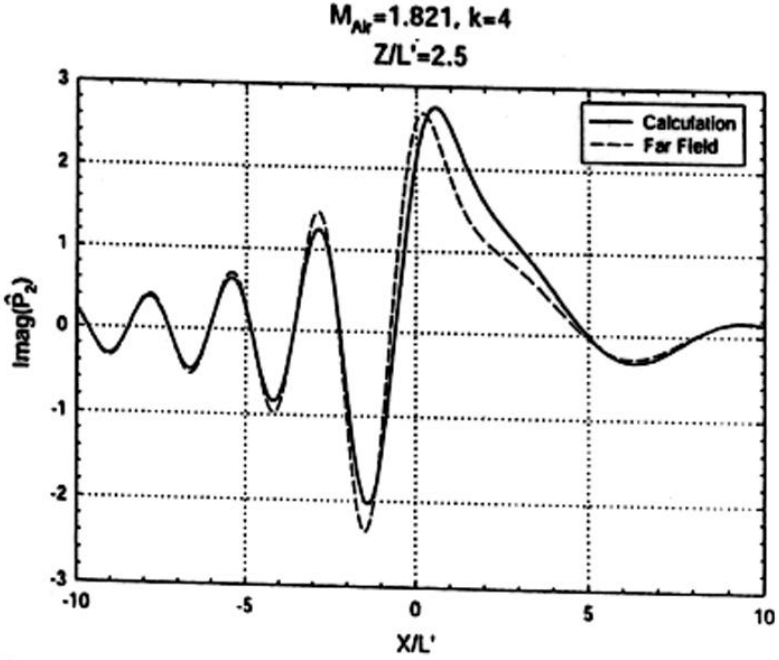
M_Air=1.821, k=4
Z/L'=2.5
Calculation
Far Field
Imag(P̂2)
X/L'

Fig. 3.7

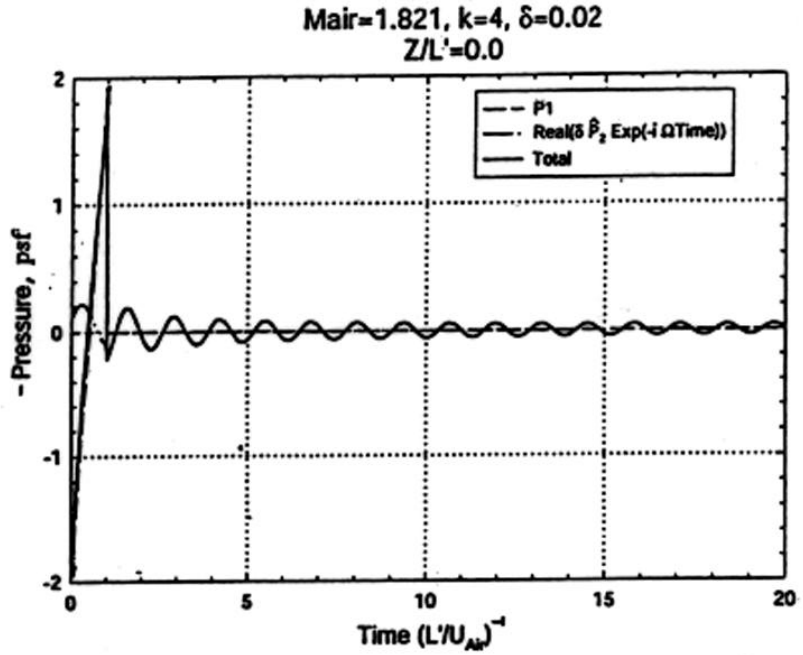

Fig. 3.8

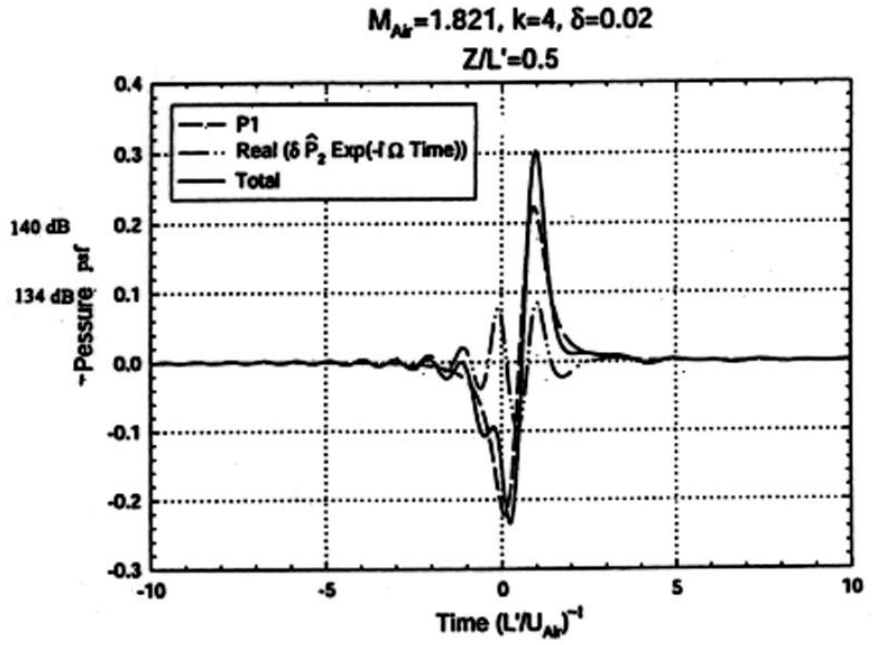

Fig. 3.9

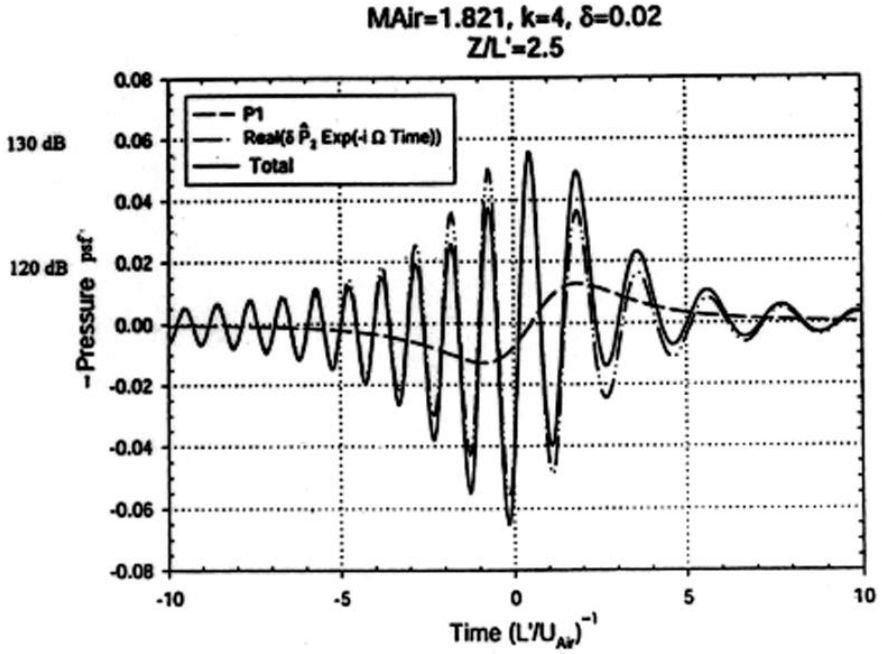

Fig. 3 .10

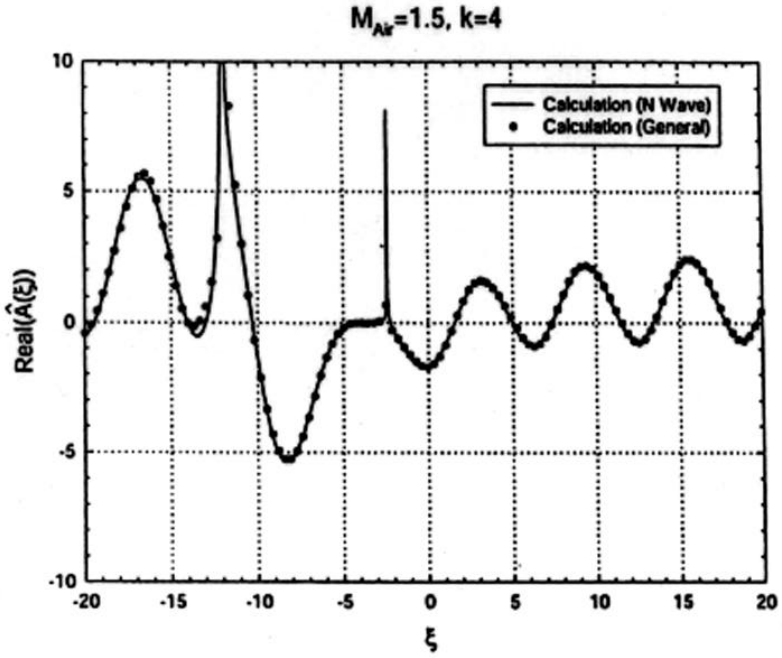

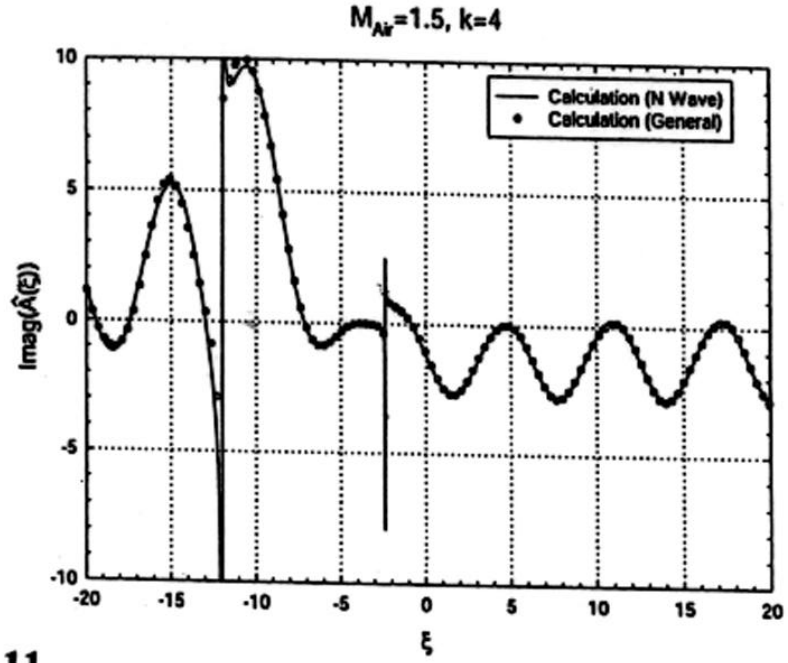

Fig. 3.11

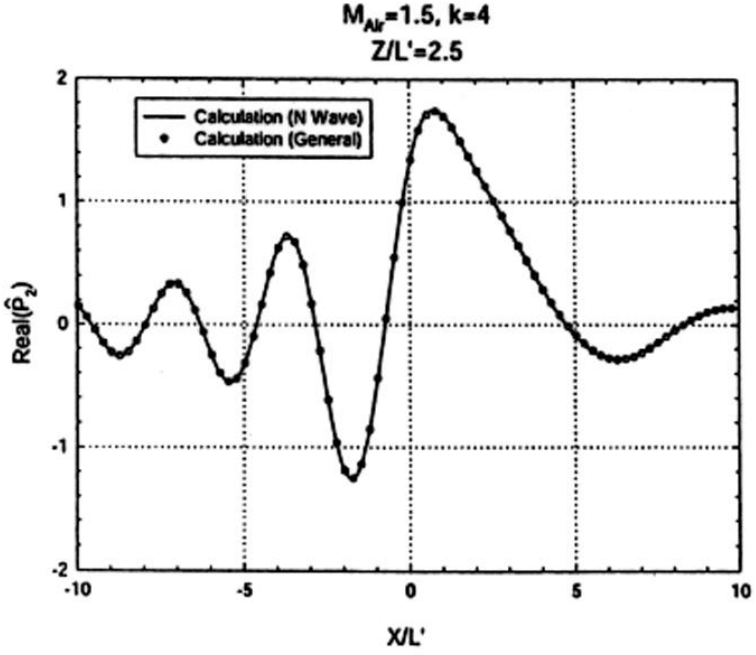

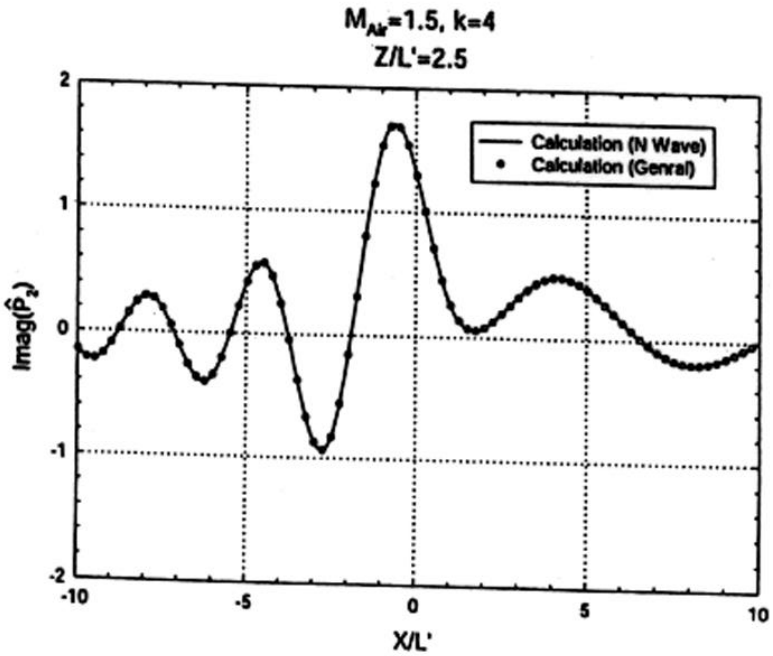

Fig. 3.12

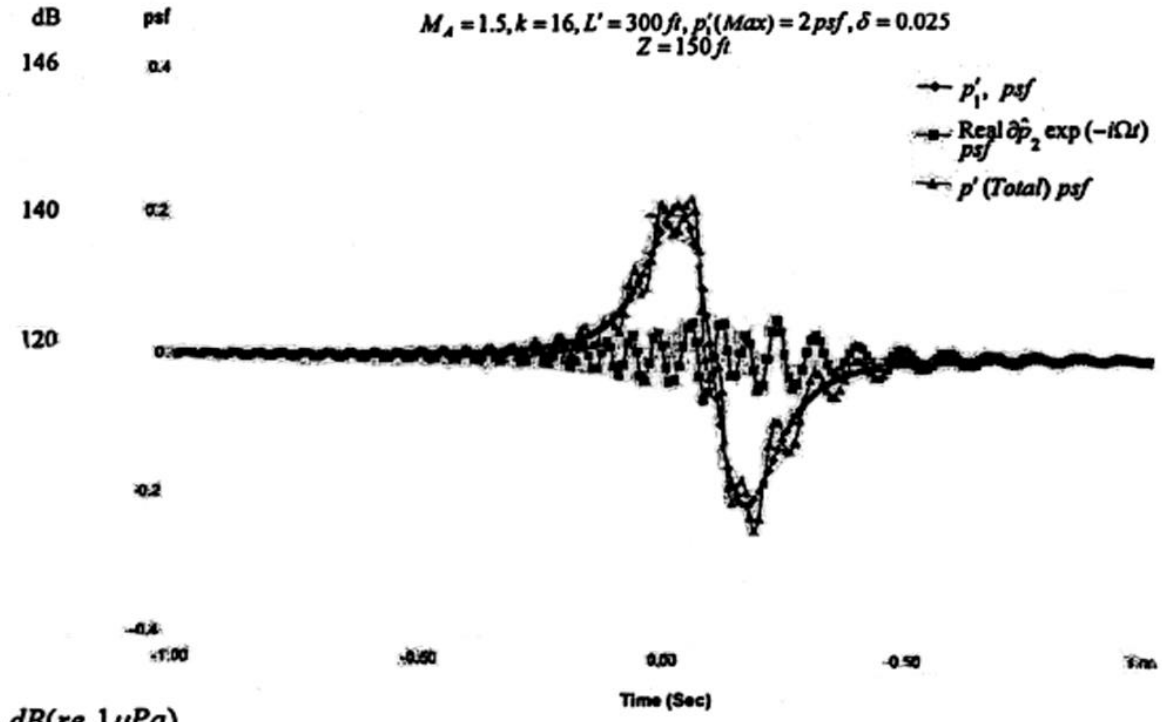

$dB(re\ 1\mu Pa)$

Fig. 3.13a

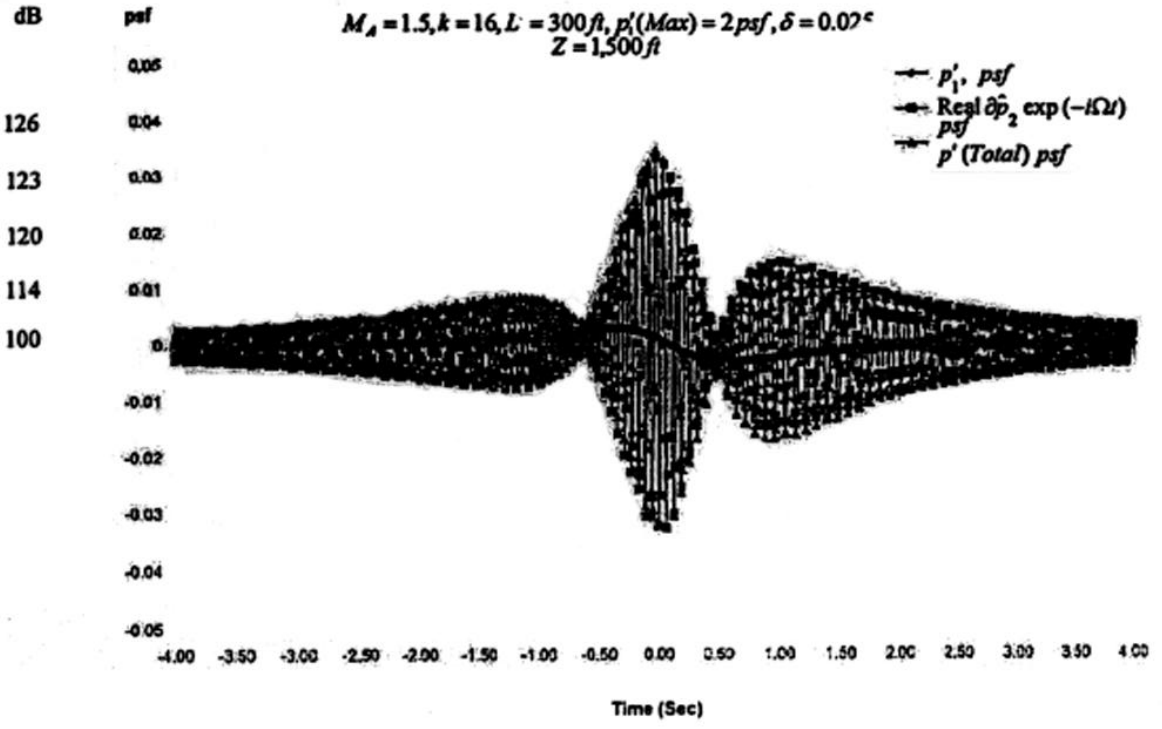

Fig. 3.13b

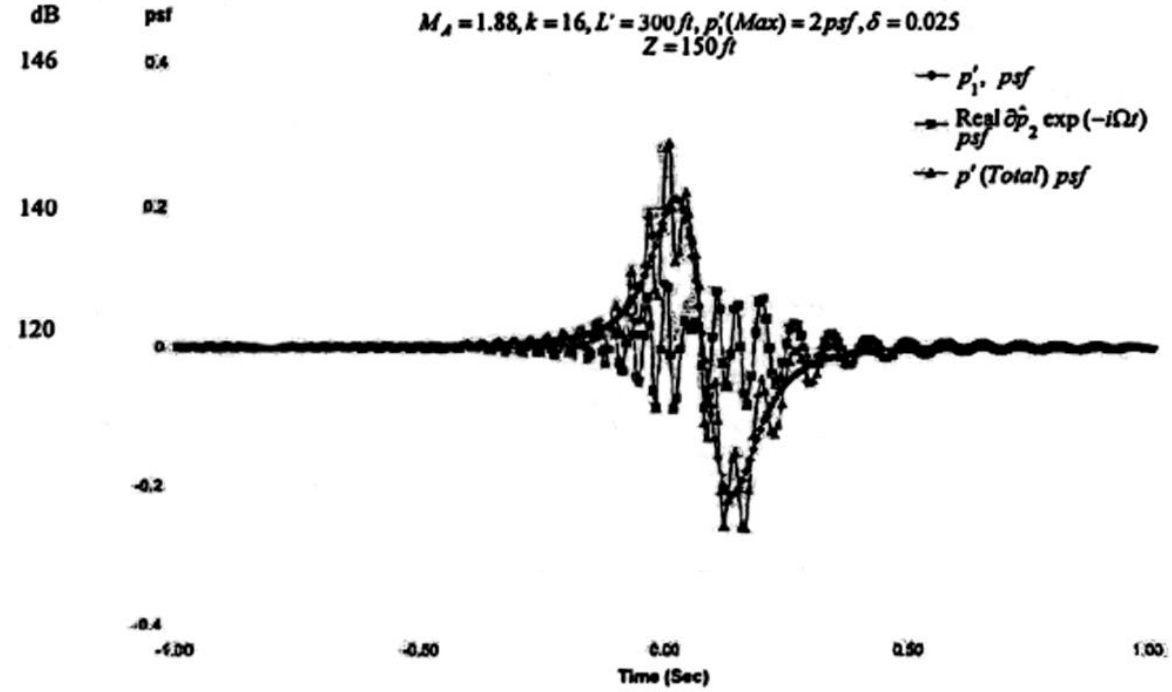

$dB(re\ 1\mu Pa)$

Fig. 3.14a

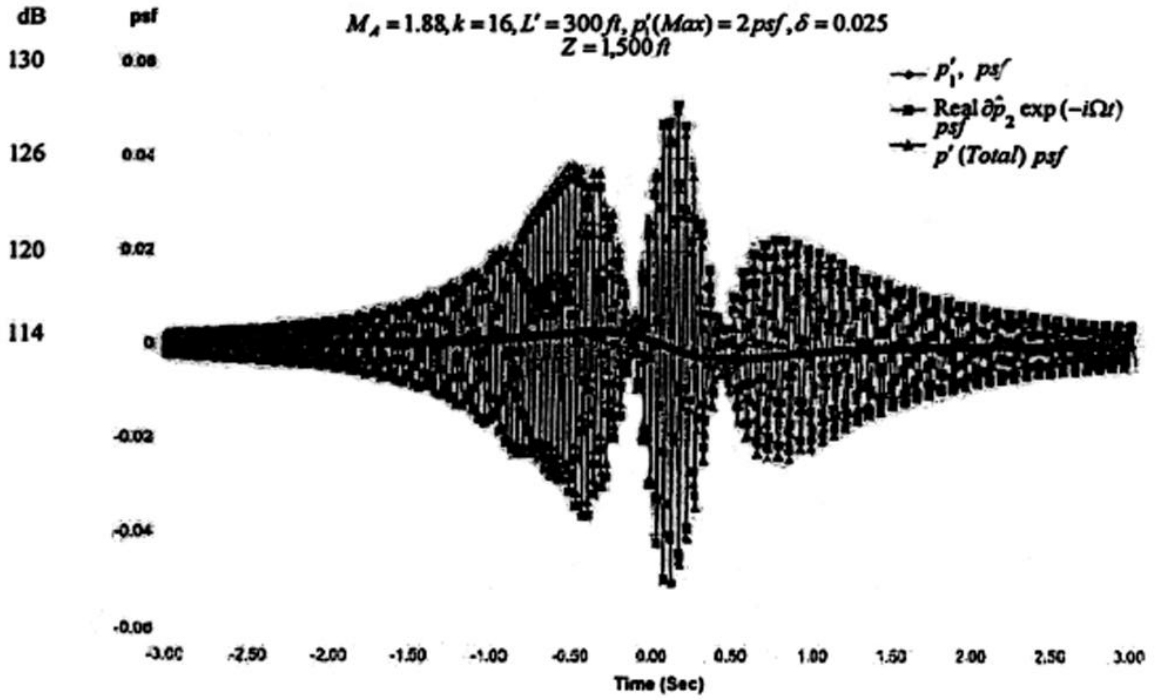

Fig. 3.14b

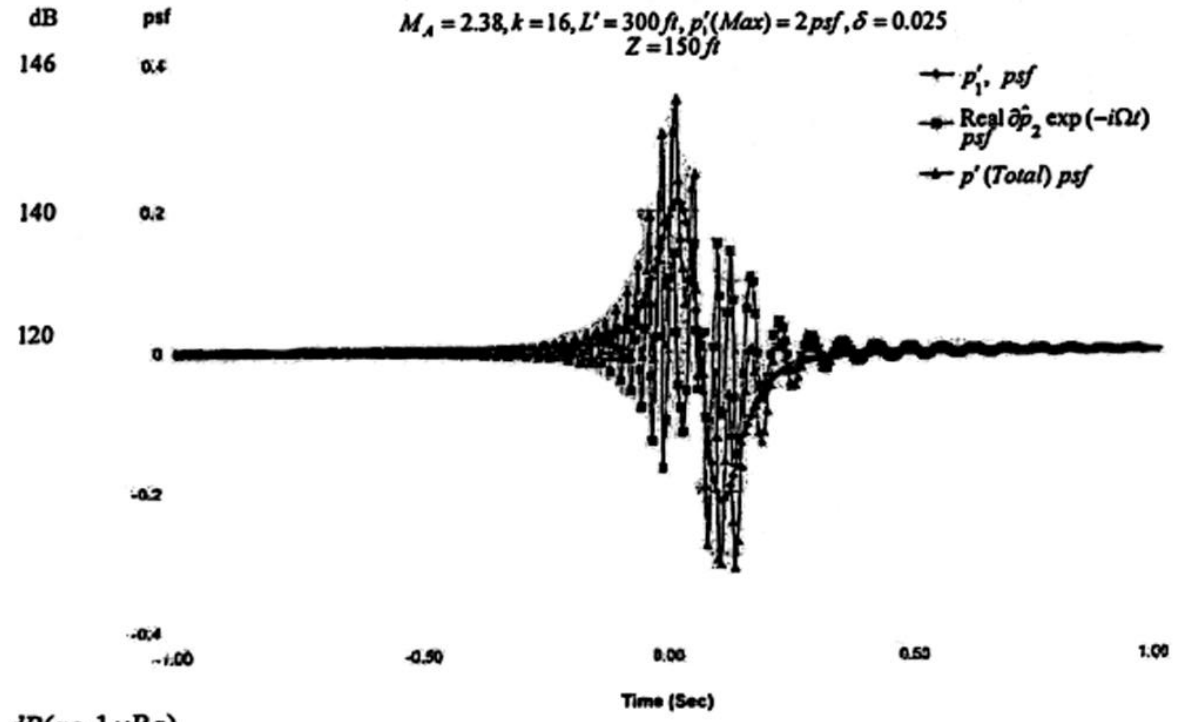

$dB(re\ 1\mu Pa)$

Fig. 3.15a

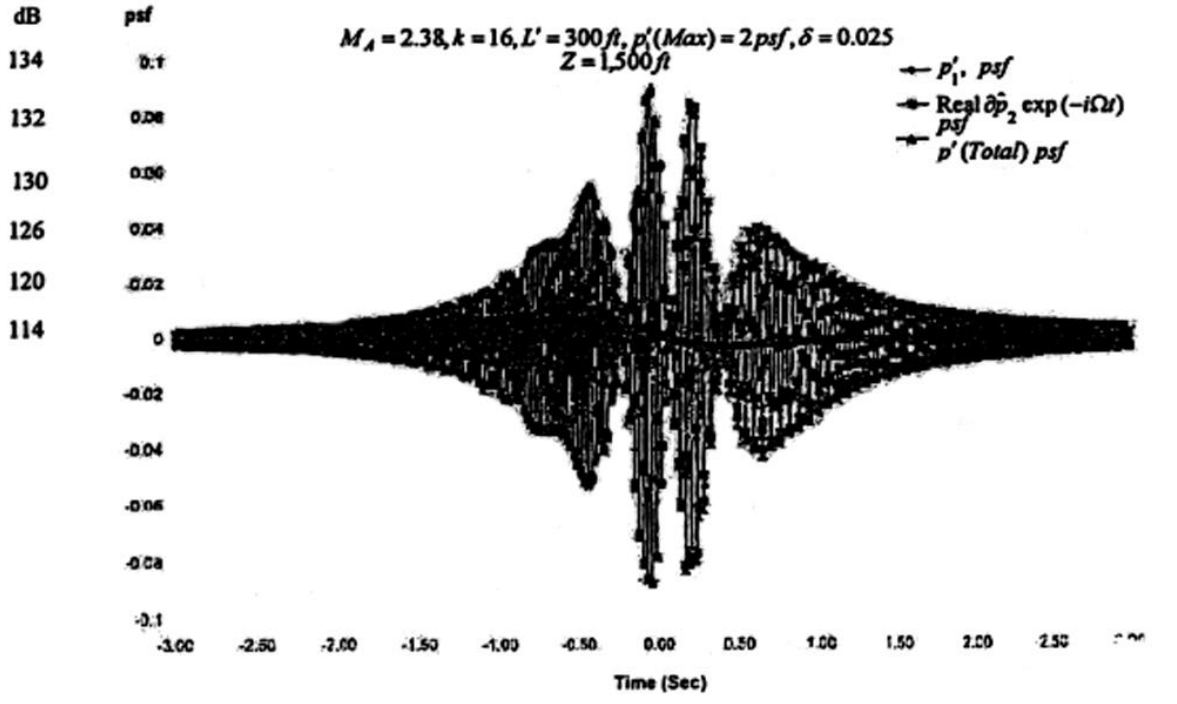

Fig. 3.15b

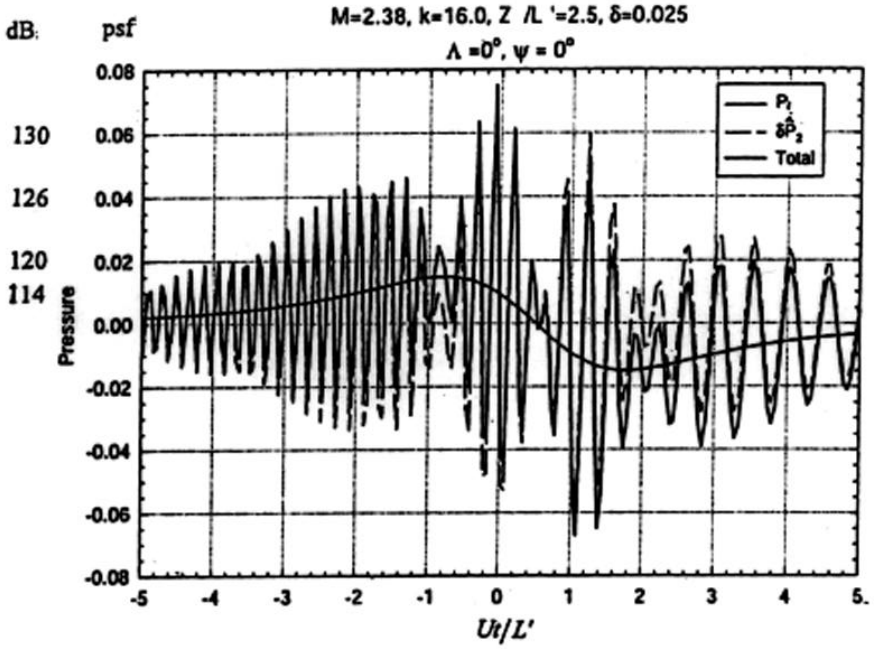

Fig. 3.16a

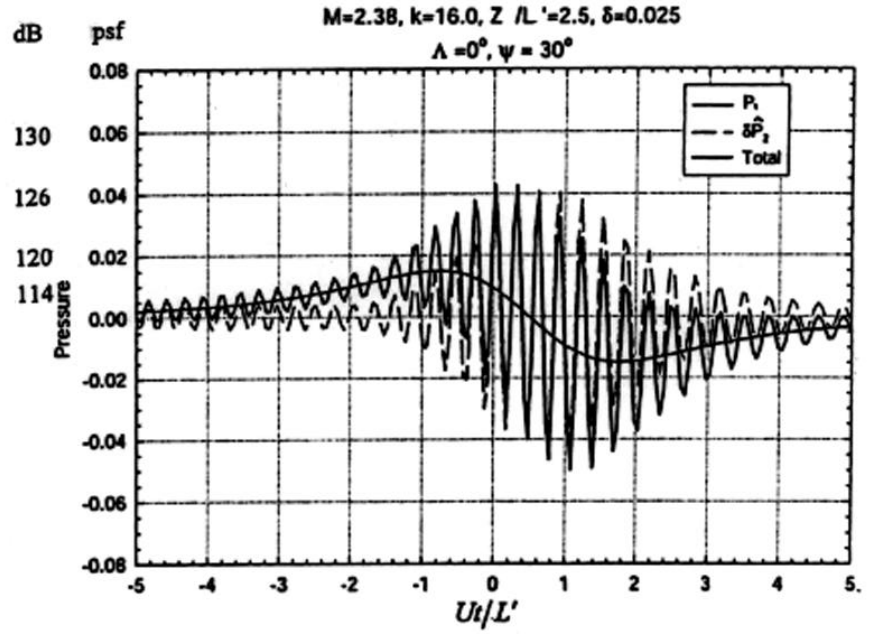

Fig. 3.16b

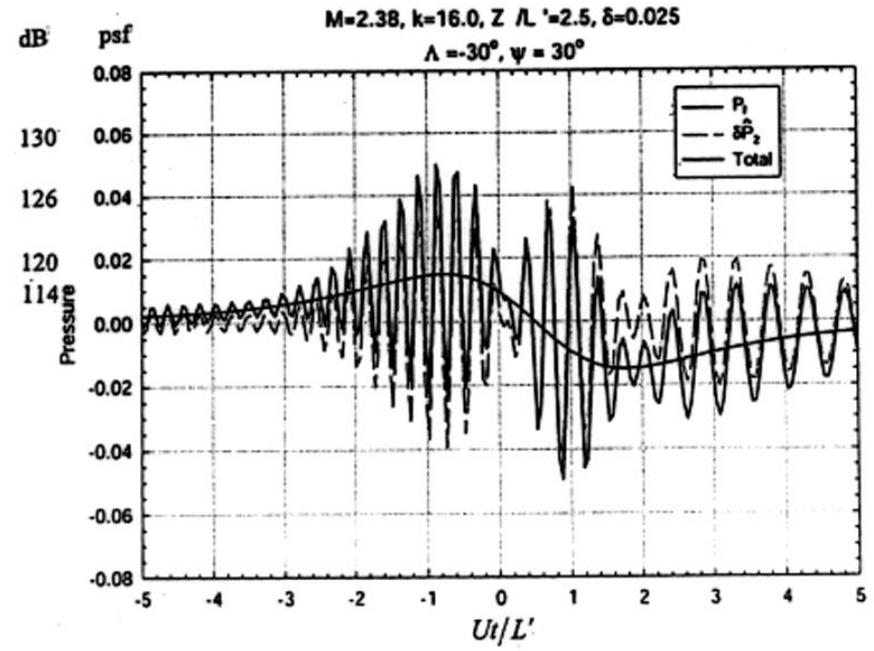

Fig. 3.16c

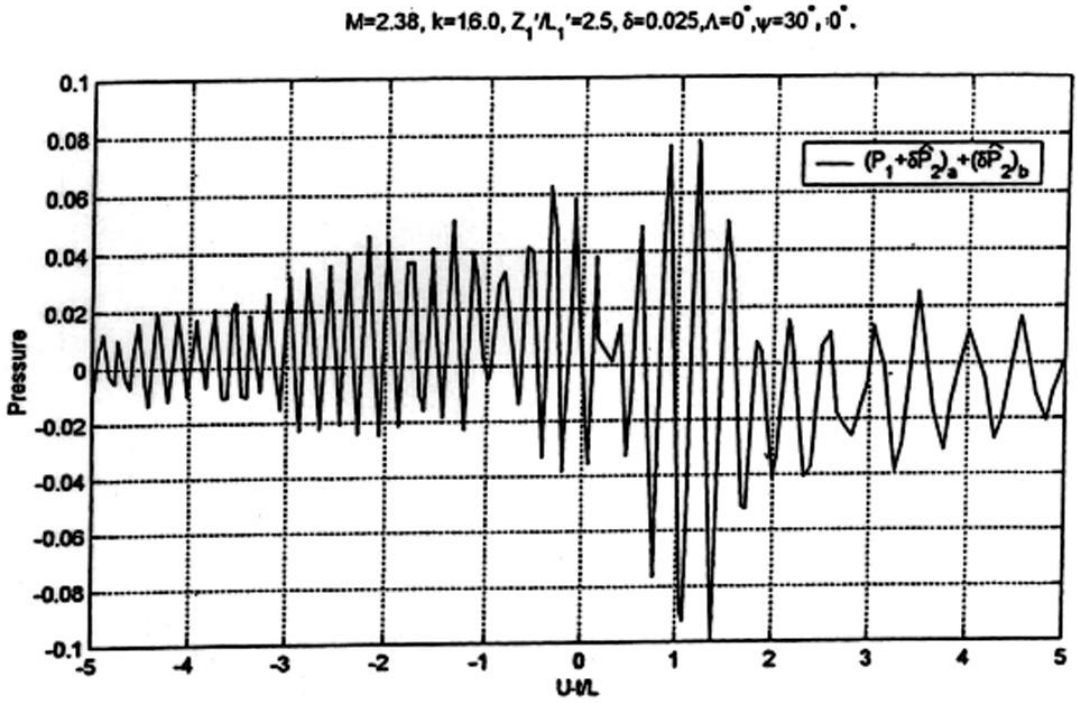

Fig. 3.17a

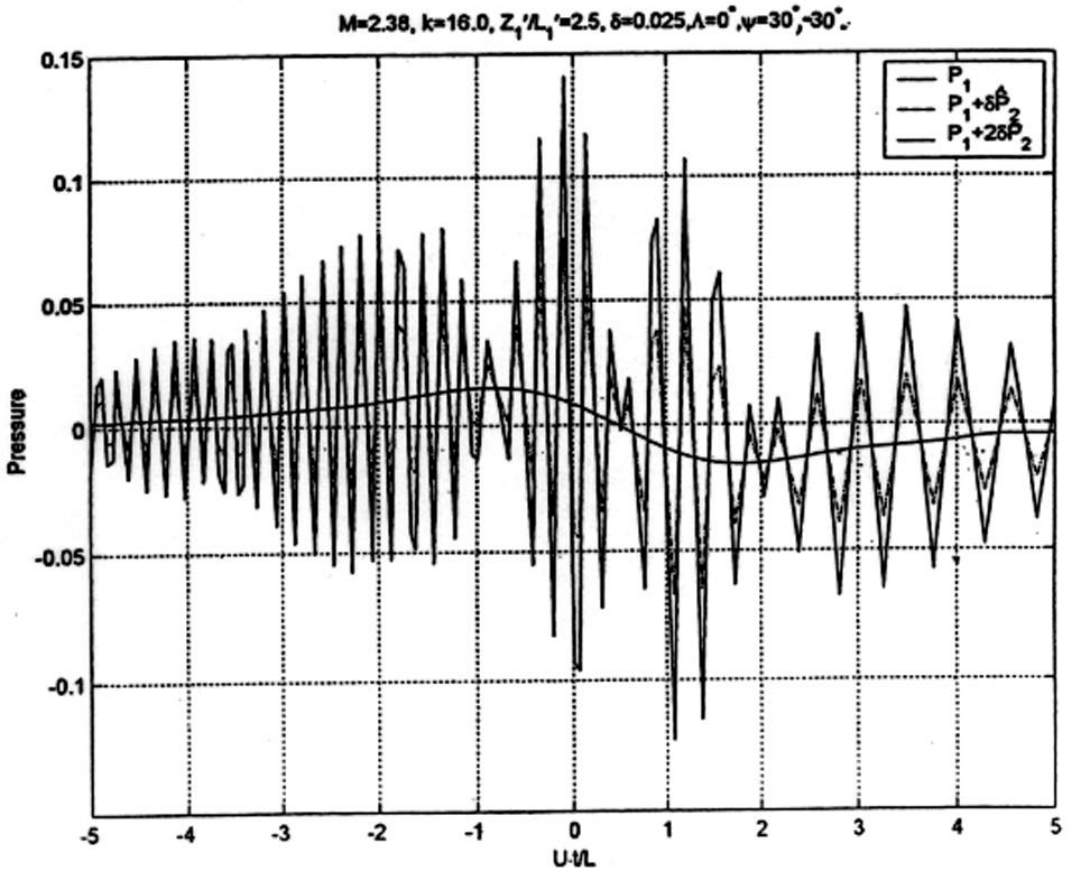

Fig. 3.17b

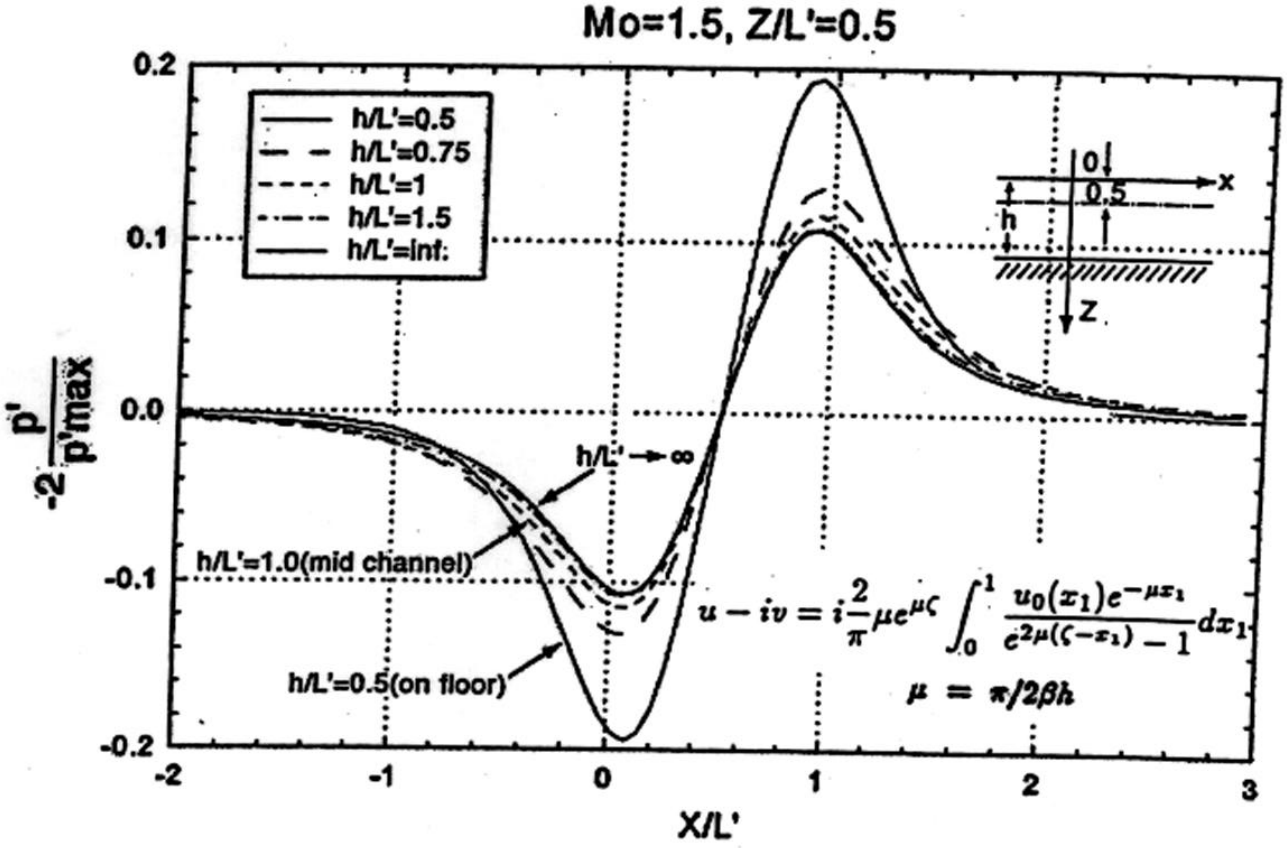
Mo=1.5, Z/L'=0.5
h/L'=0.5
h/L'=0.75
h/L'=1
h/L'=1.5
h/L'=inf.
h/L'→∞
h/L'=1.0(mid channel)
h/L'=0.5(on floor)
$u - iv = i\frac{2}{\pi}\mu e^{\mu\zeta}\int_0^1 \frac{u_0(x_1)e^{-\mu x_1}}{e^{2\mu(\zeta-x_1)}-1}dx_1$
$\mu = \pi/2\beta h$
0
0.5
h
x
z
$-2\frac{p'}{p'max}$
X/L'
0.2
0.1
0.0
-0.1
-0.2
-2
-1
0
1
2
3

Fig. 3.18

$\rho_1=1$ $\rho_2=1.91$

$c_1=1500$ $c_a=331$ $c_p=1711$ $c_s=503$

$m_1=0.331$ $m_p=0.290$ $m_s=0.987$

$\beta_1=0.944$ $\beta_p=0.957$ $\beta_s=0.160$

$D_{BW}=-15.409$

Fig. 3.19

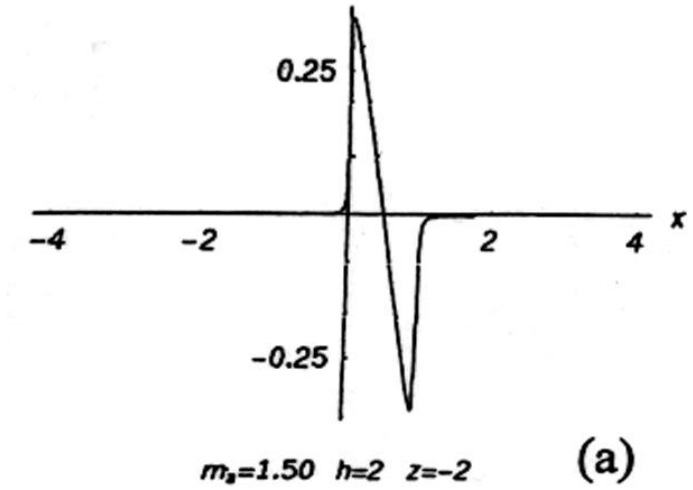

$m_a=1.50$ $h=2$ $z=-2$ (a)

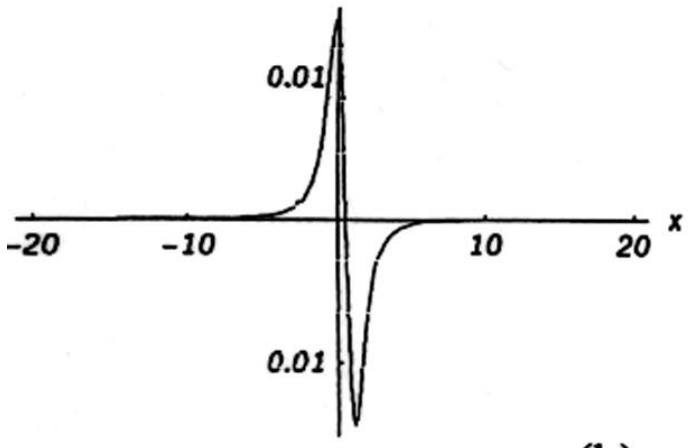

$m_a=1.50$ $h=2$ $z=-1$ (b)

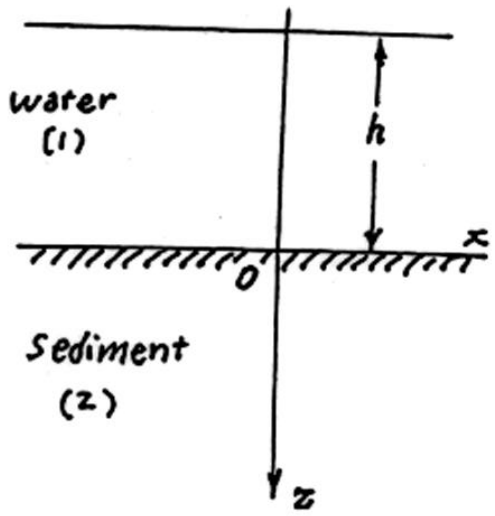

Fig. 3.20

$\rho_1=1$ $\rho_2=1.91$

$c_1=1500$ $c_a=331$ $c_p=1711$ $c_s=503$

$m_1=0.300$ $m_p=0.263$ $m_s=0.895$

$\beta_1=0.954$ $\beta_p=0.965$ $\beta_s=0.446$

$D_{BW}=-1.09$

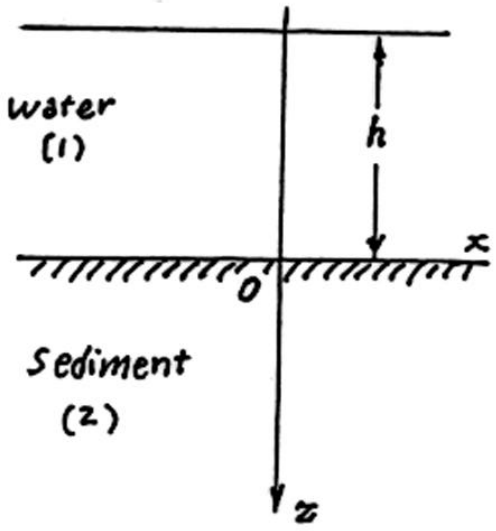

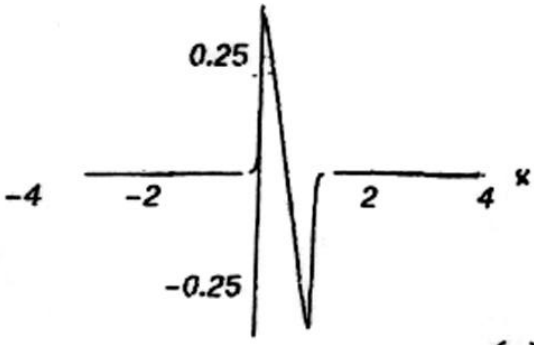

$m_a=1.36$ $h=2$ $z=-2$ (a)

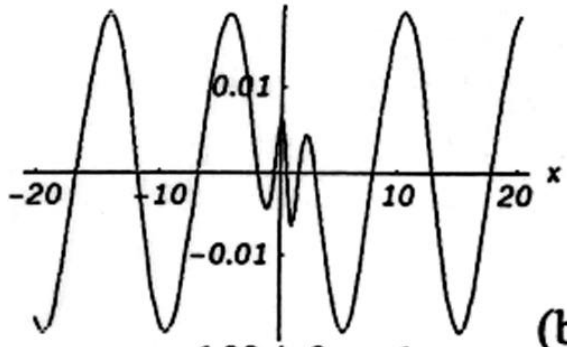

$m_a=1.36$ $h=2$ $z=-1$ (b)

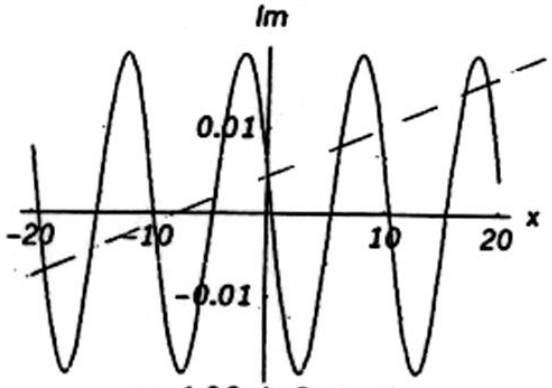

$m_a=1.36$ $h=2$ $z=-1$

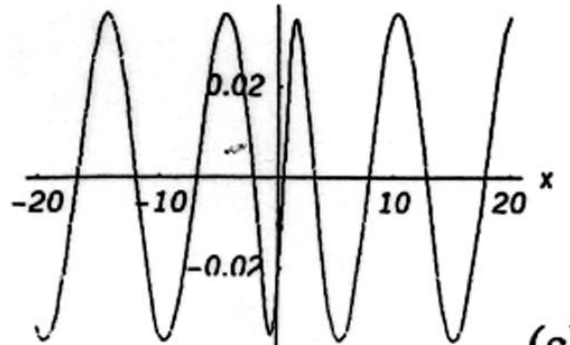

$m_a=1.36$ $h=2$ $z=0$ (c)

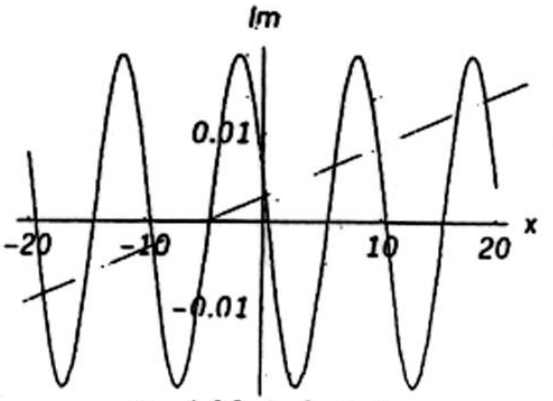

$m_a=1.36$ $h=2$ $z=0$

Fig. 3.21

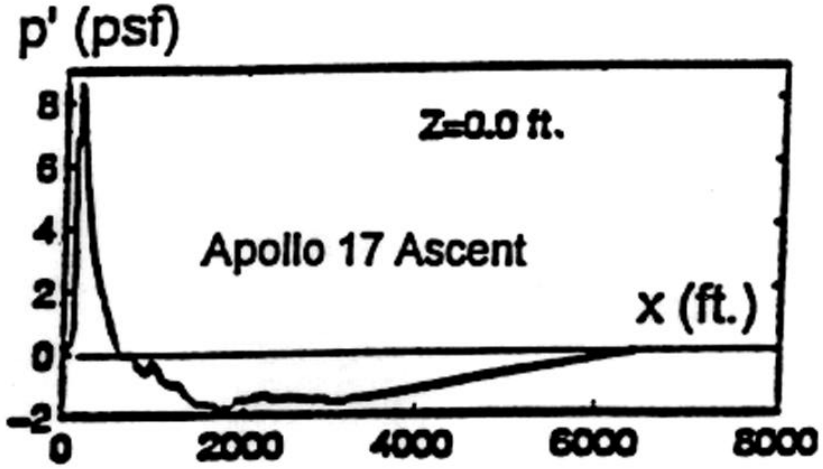
p' (psf)
Z=0.0 ft.
Apollo 17 Ascent
x (ft.)
8
6
4
2
0
-2
0
2000
4000
6000
8000

(a)

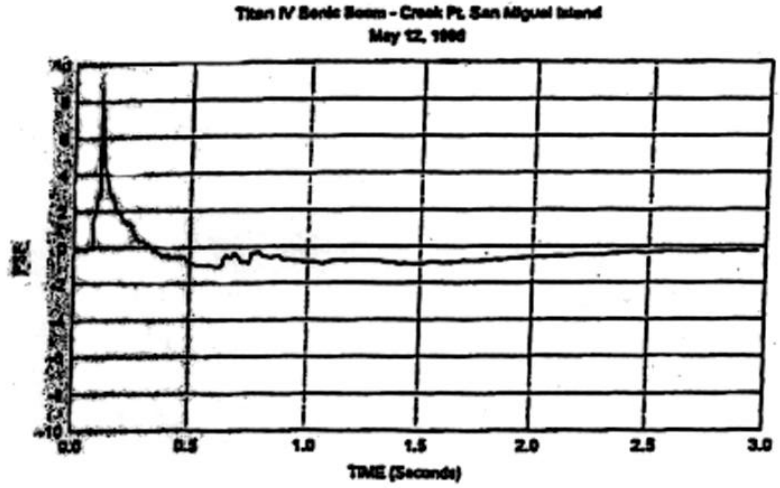
TIME (Seconds)
0.0
0.5
1.0
1.5
2.0
2.5
3.0

(b)

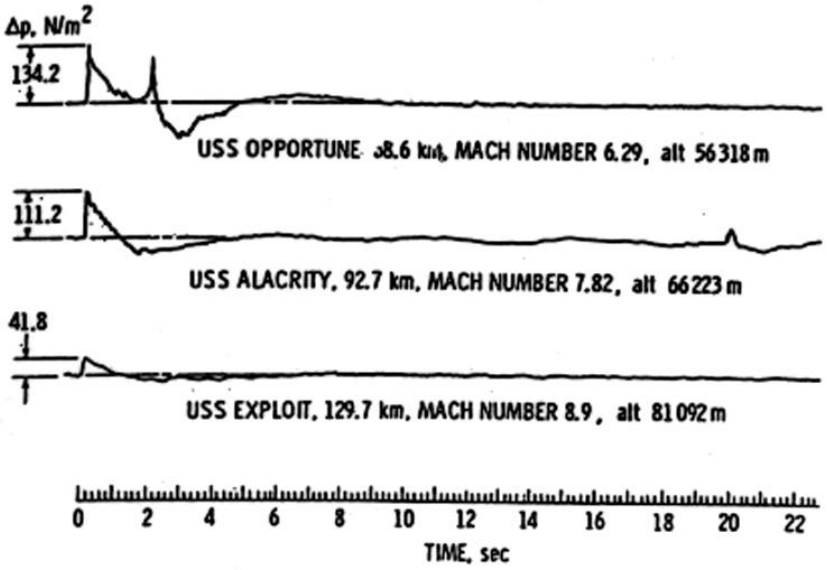
Δp, N/m2
134.2
USS OPPORTUNE
MACH NUMBER 6.29, alt 56318 m
111.2
USS ALACRITY, 92.7 km, MACH NUMBER 7.82, alt 66223 m
41.8
USS EXPLOIT, 129.7 km, MACH NUMBER 8.9, alt 81092 m
0
2
4
6
8
10
12
14
16
18
20
22
TIME, sec

(c)

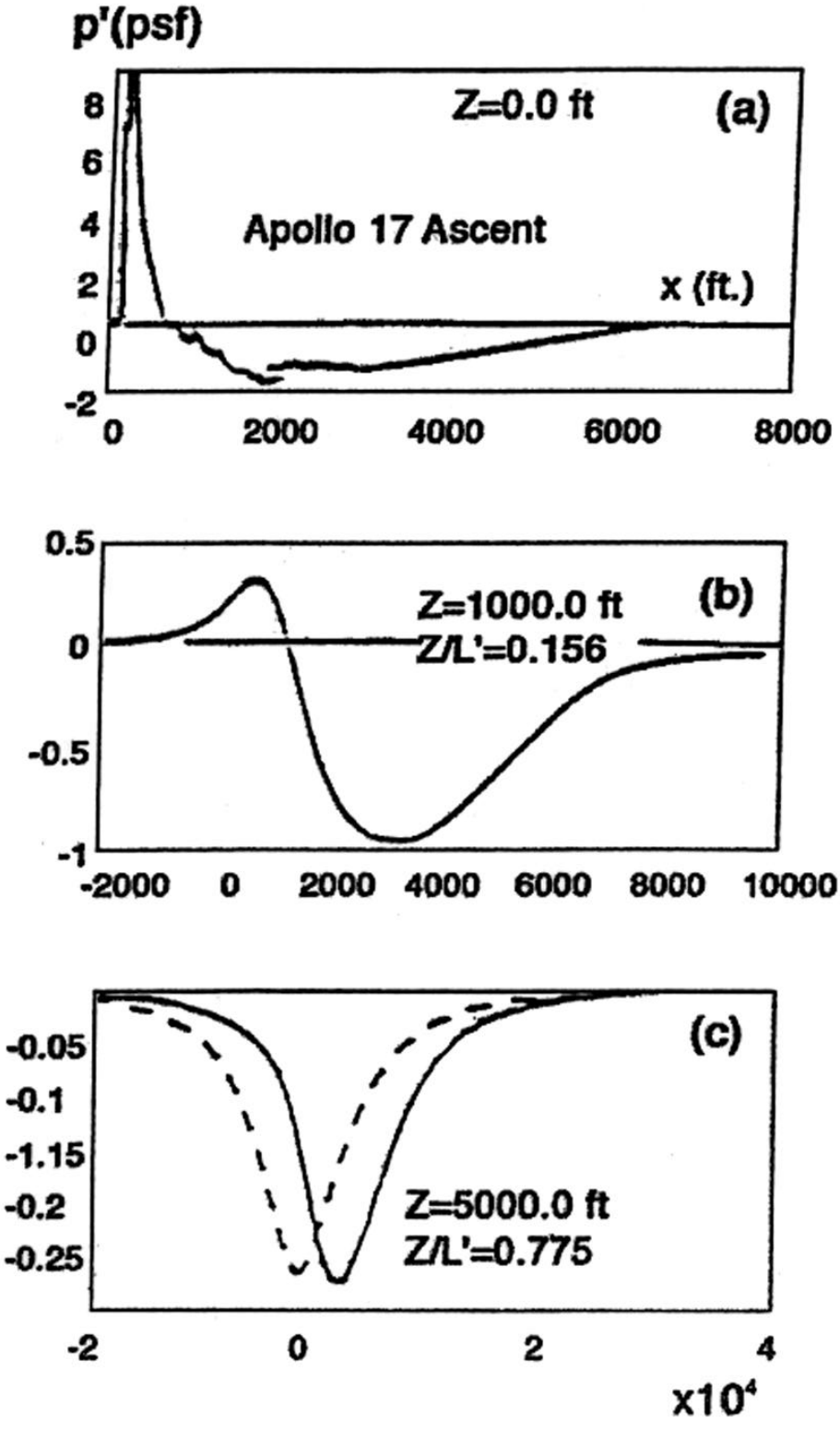
p'(psf)
Z=0.0 ft
(a)
Apollo 17 Ascent
x (ft.)
8
6
4
2
0
-2
0
2000
4000
6000
8000
0.5
0
-0.5
-1
Z=1000.0 ft
Z/L'=0.156
(b)
-2000
0
2000
4000
6000
8000
10000
-0.05
-0.1
-1.15
-0.2
-0.25
Z=5000.0 ft
Z/L'=0.775
(c)
-2
0
2
4
x10⁴

Fig. 3.22

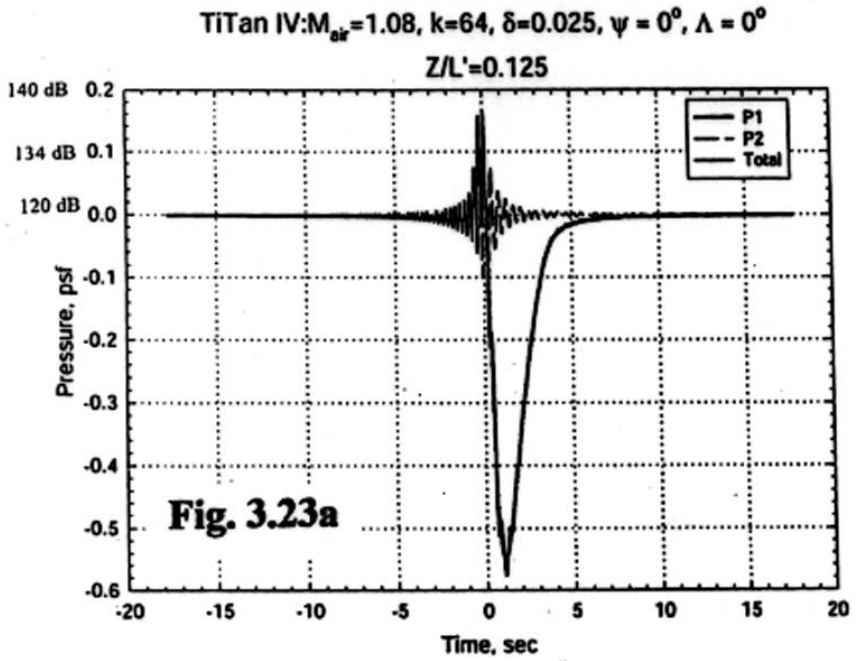

Fig. 3.23a

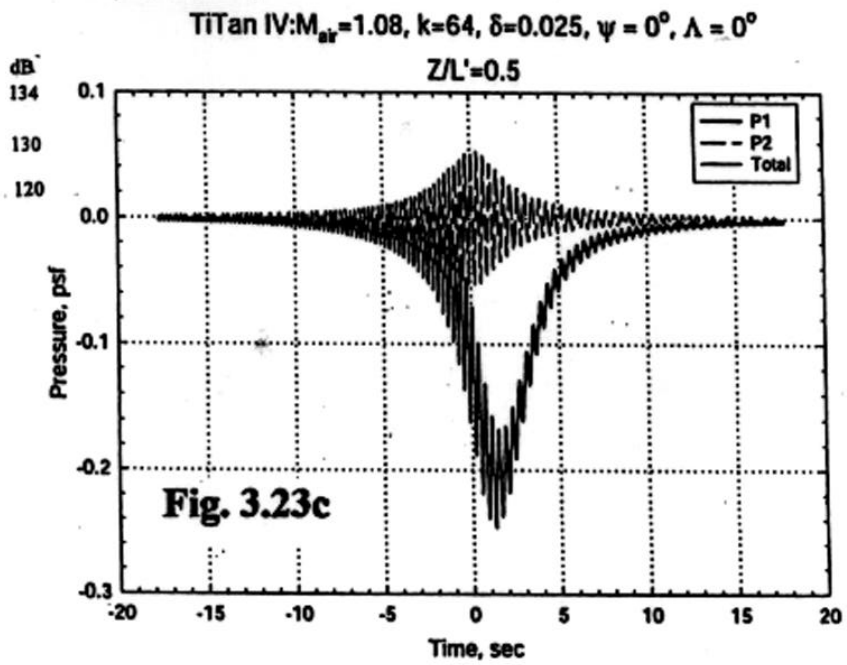

Fig. 3.23c

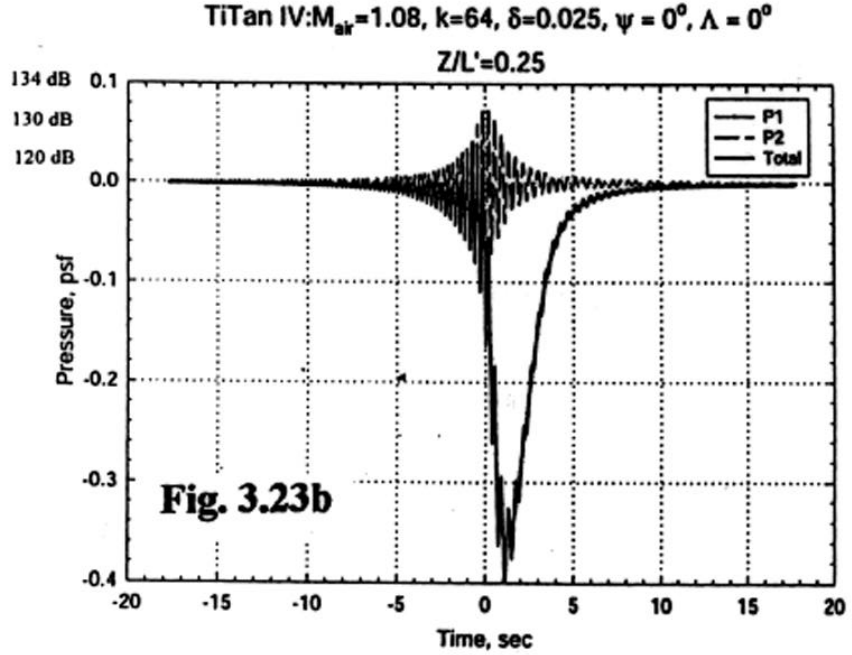

Fig. 3.23b

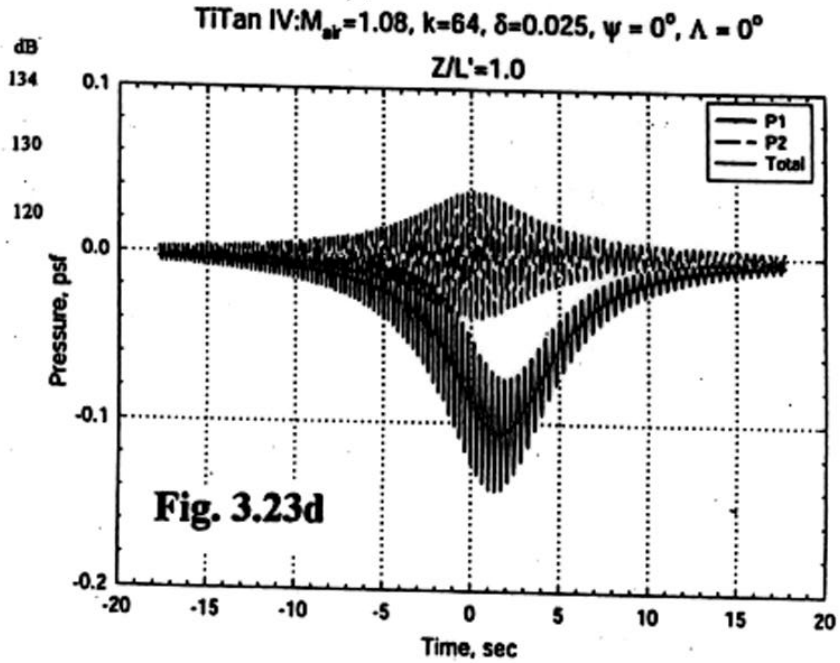

Fig. 3.23d

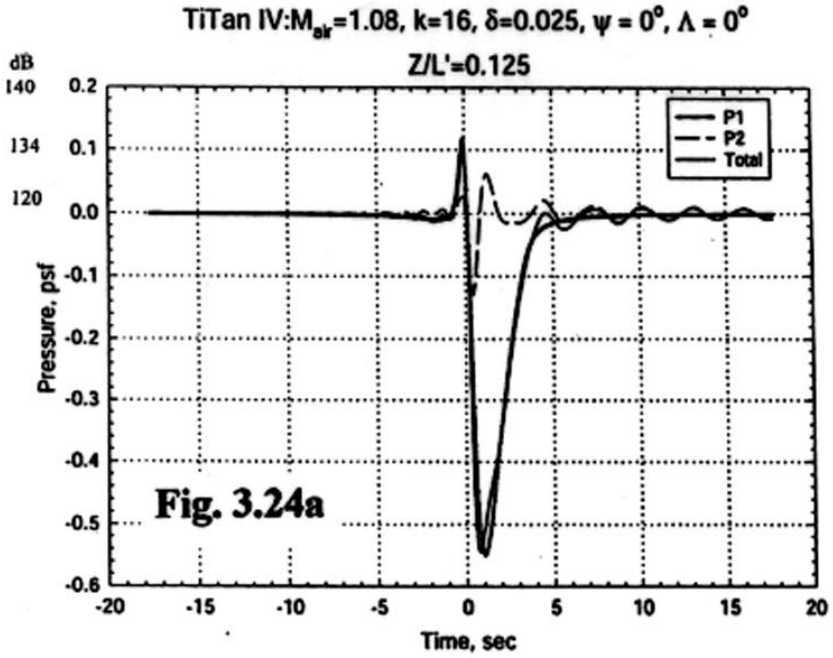

Fig. 3.24a

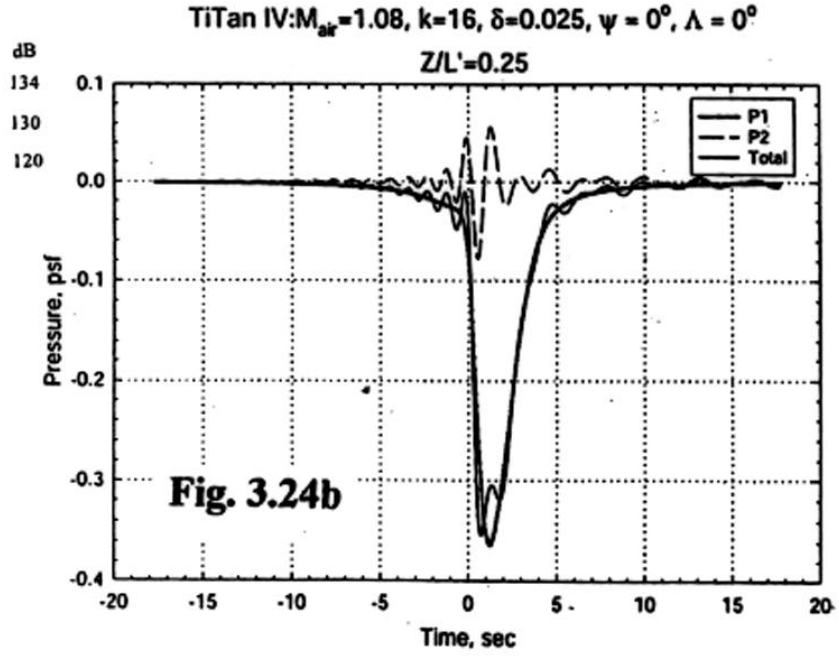

Fig. 3.24b

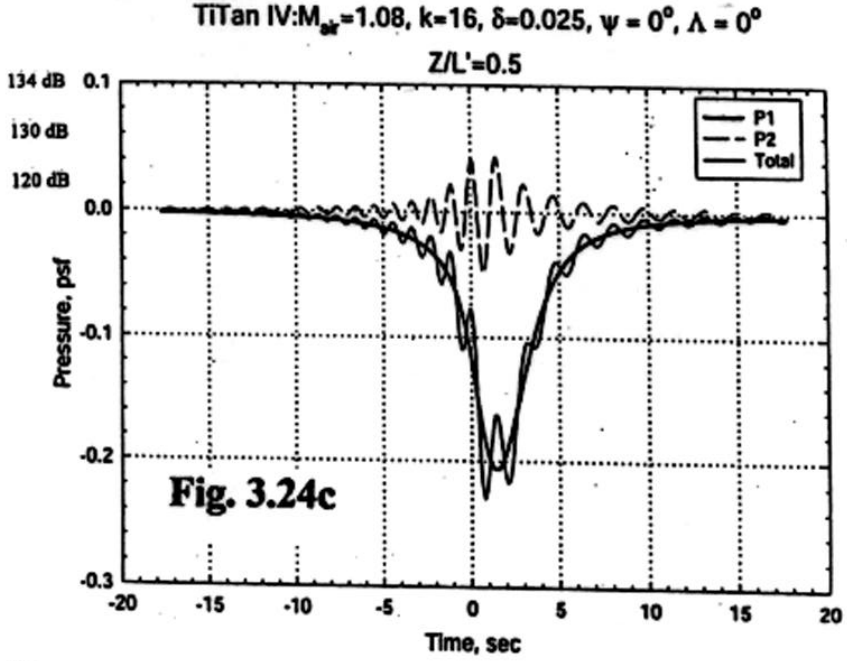

Fig. 3.24c

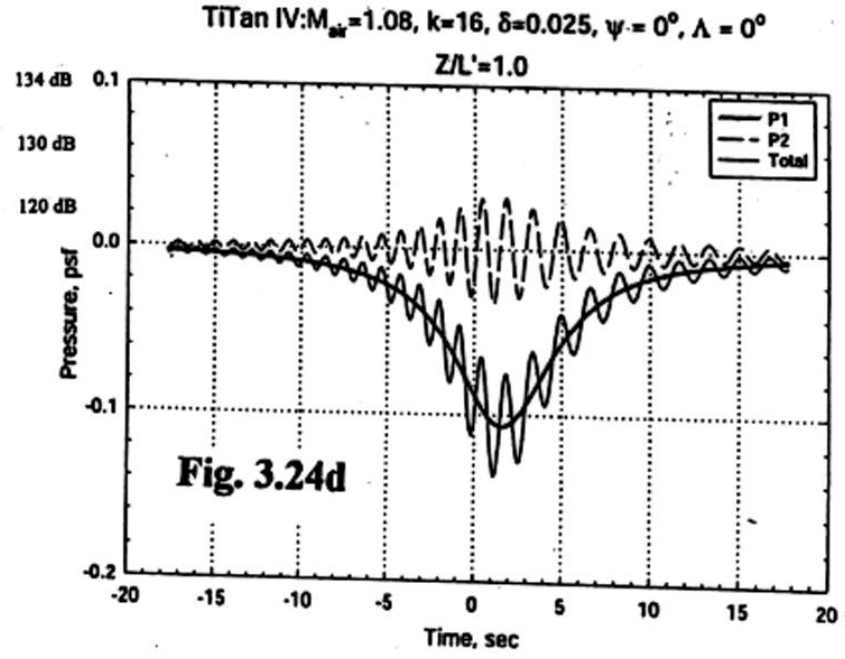

Fig. 3.24d

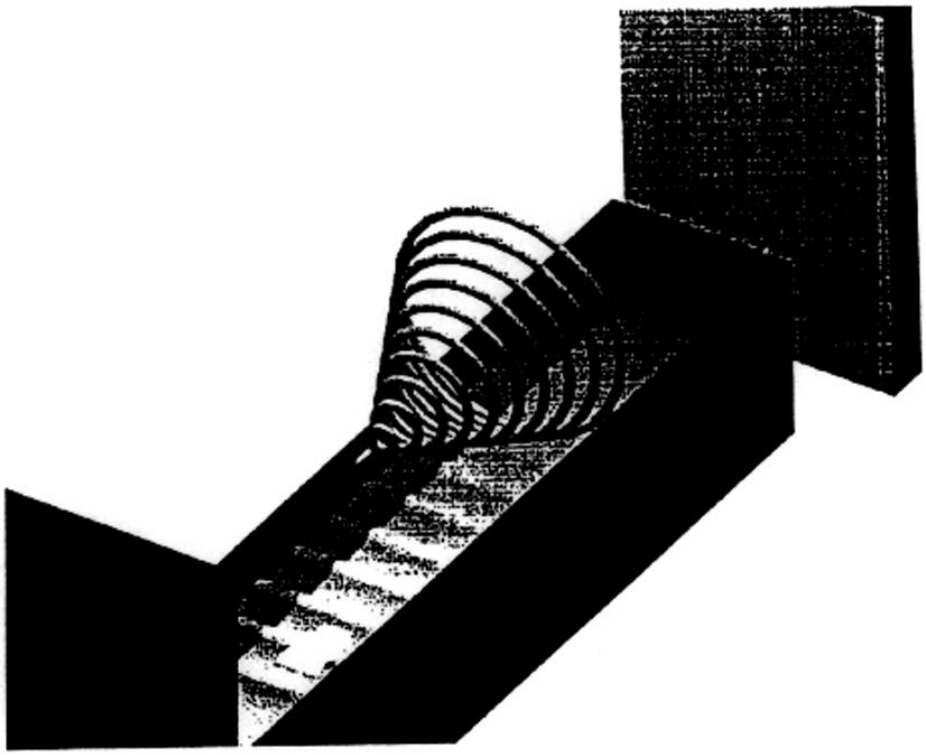

Fig. 4.1 : Perspective view of the basic laboratory setup.

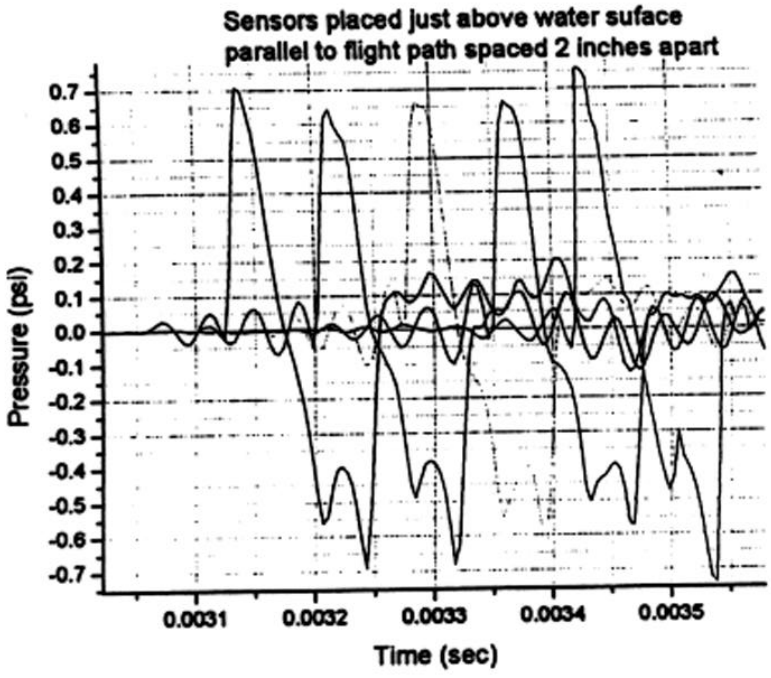

Fig. 4.2: Pressure signals from 5 piezotrons placed parallel to the flight path in the air just above the air-water interface.

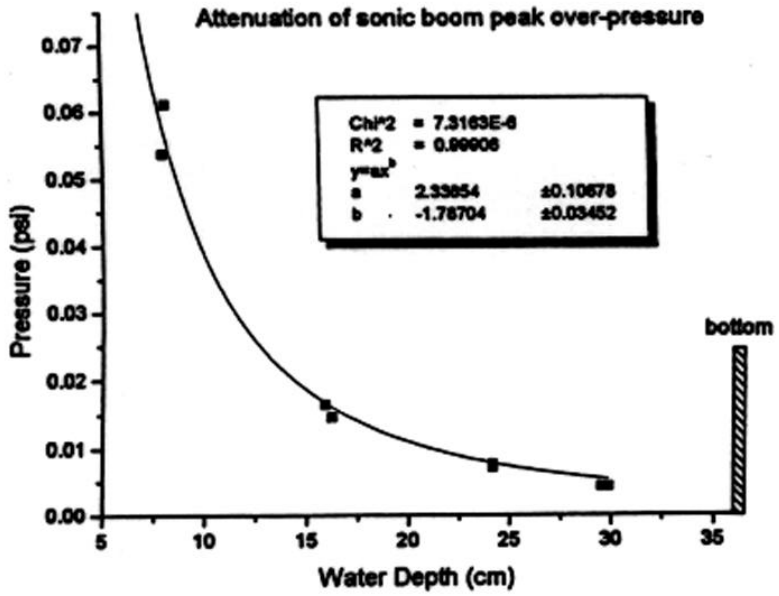

Fig. 4.3: Peak-Peak over-pressure attenuation

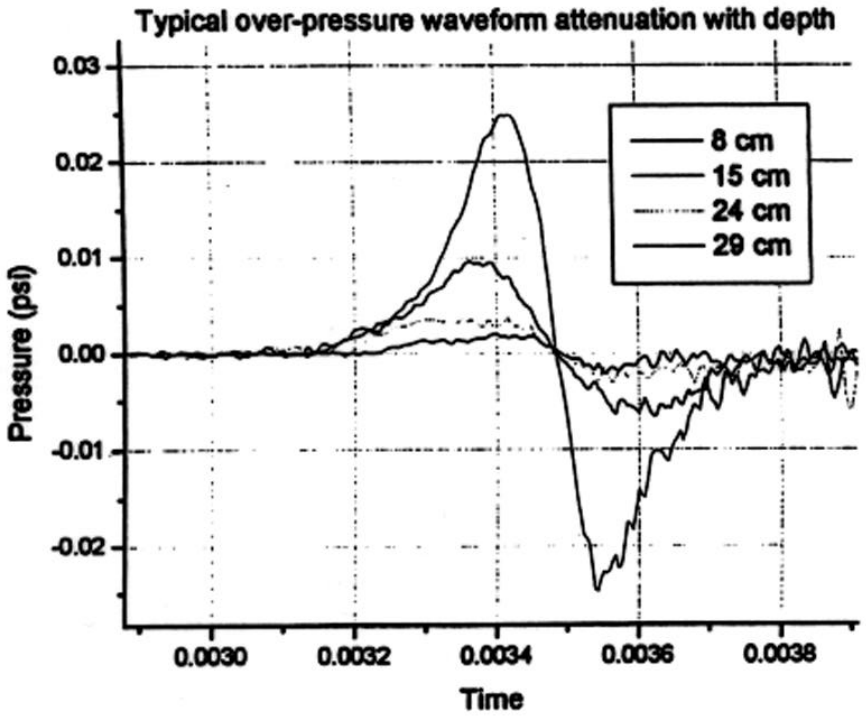

Fig. 4.4: Typical overpressure waveforms

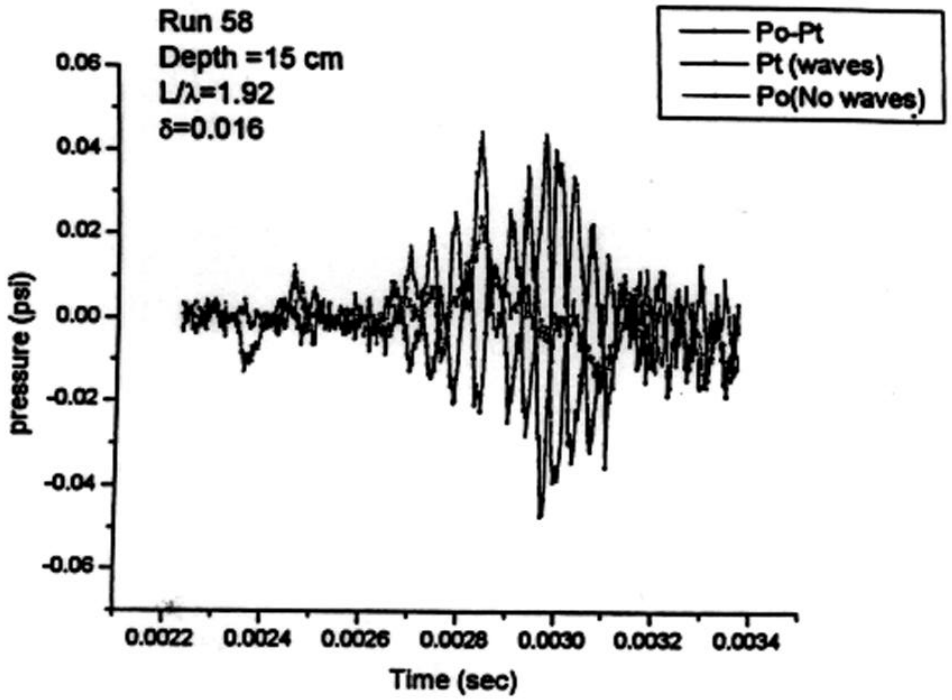

Fig. 4.5: Data with and without surface waves corresponding to a randomly chosen early experiment.

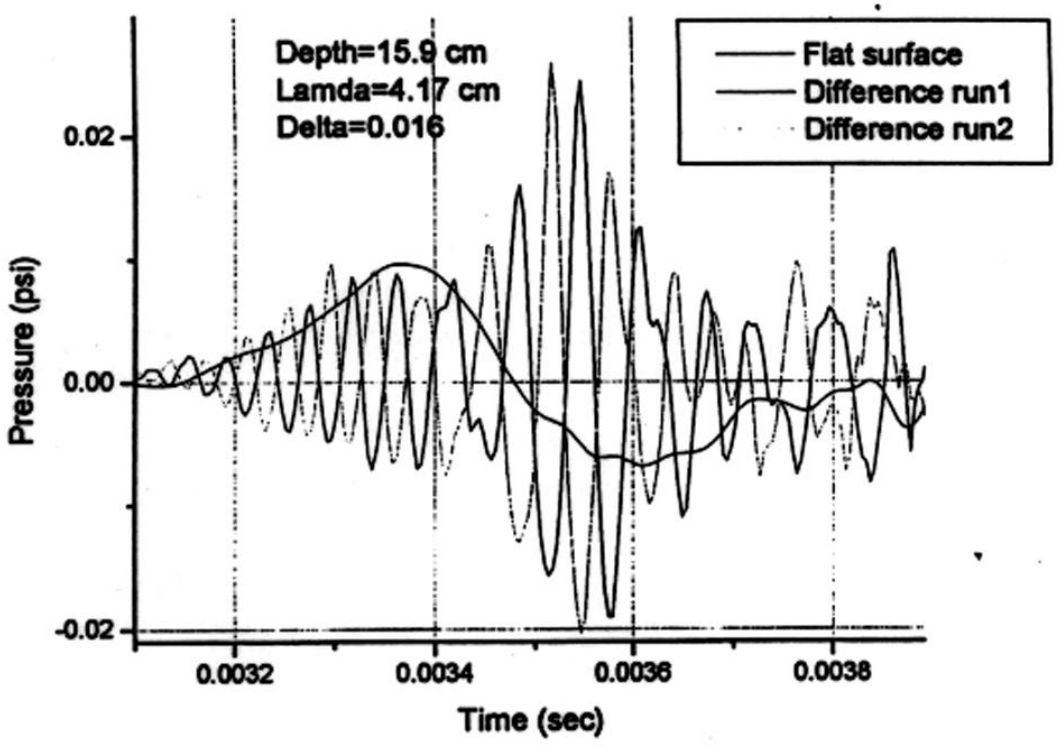

Fig. 4.6: Two different ensembles of the same experiment showing the difference in phase that permits a better resolution of the wave packet envelope.

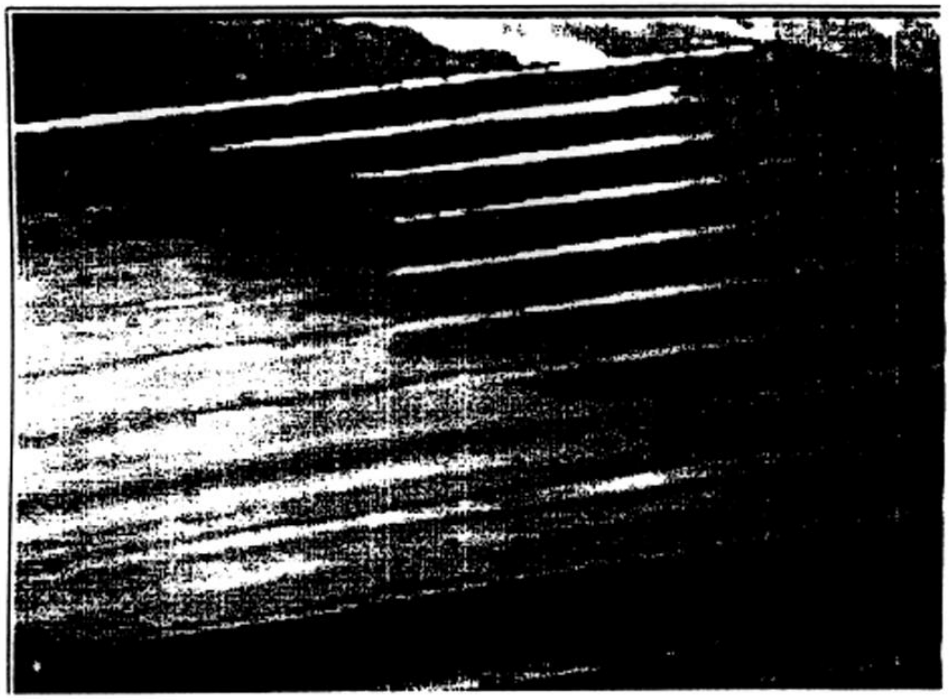

Fig. 4.7 : Image of a typical laboratory generated surface wave field.

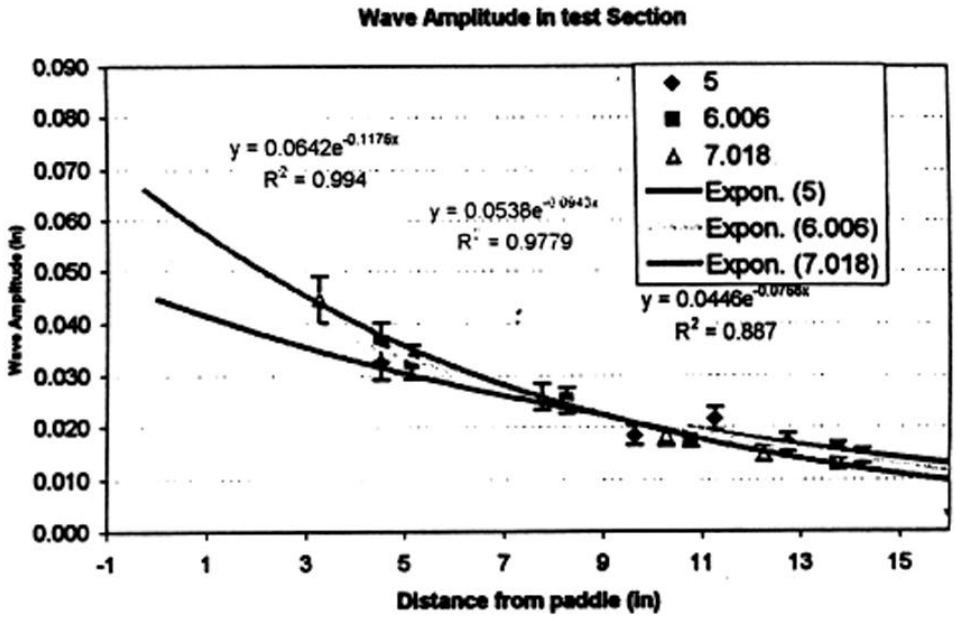

Fig. 4.8: Surface wave height decay away from the paddle.

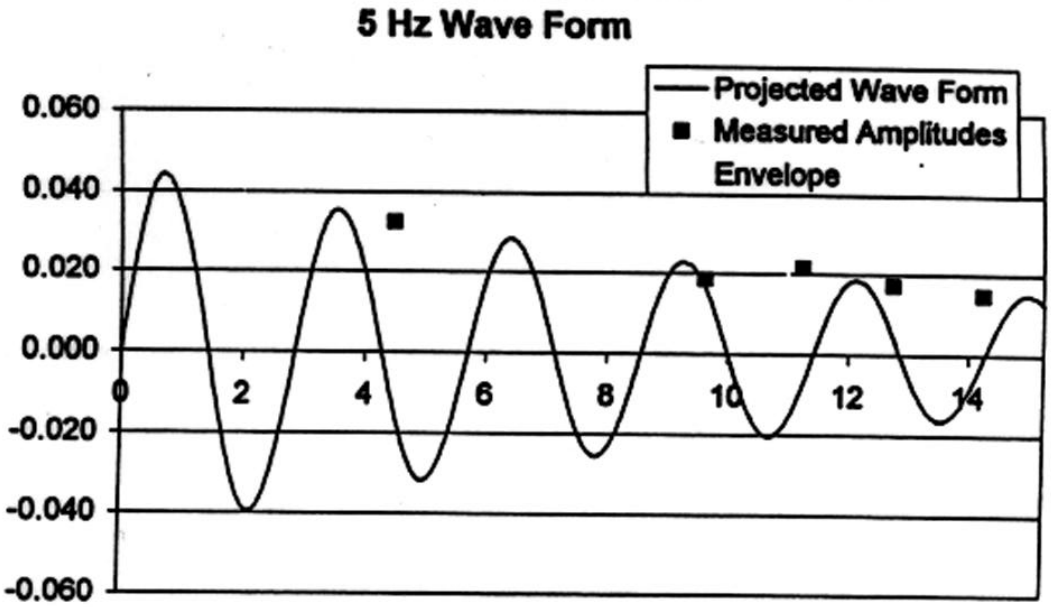

Fig. 4.9: Projected surface waveform decay with distance from paddle for λ=3.1 cm.

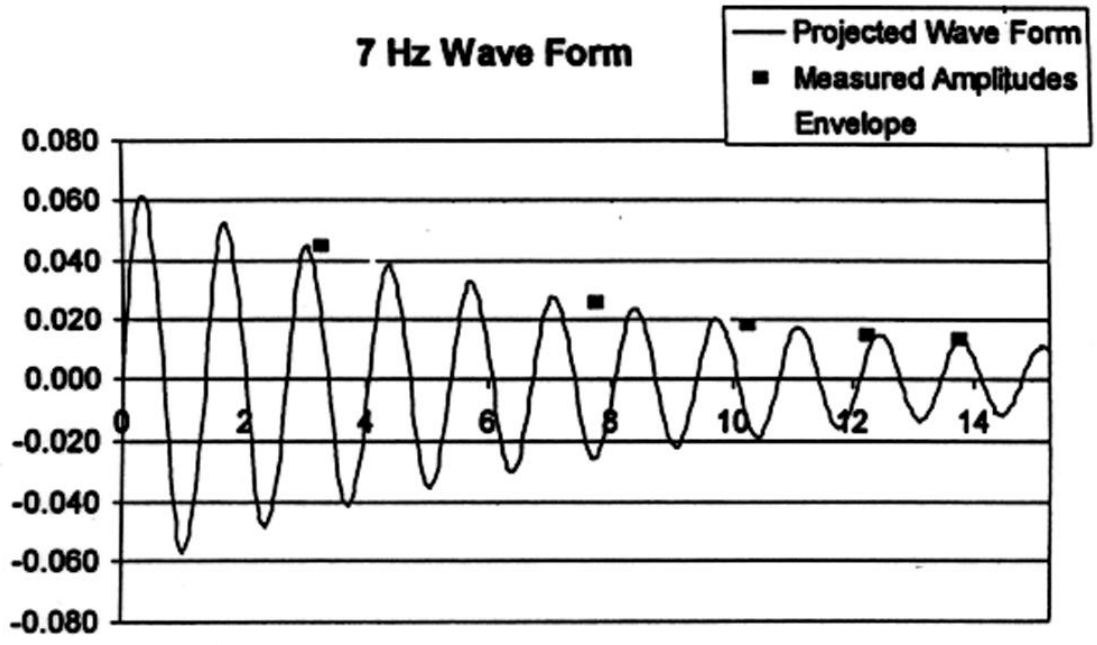

Fig. 4.10: Projected surface waveform decay with distance from paddle for λ=3.1 cm.

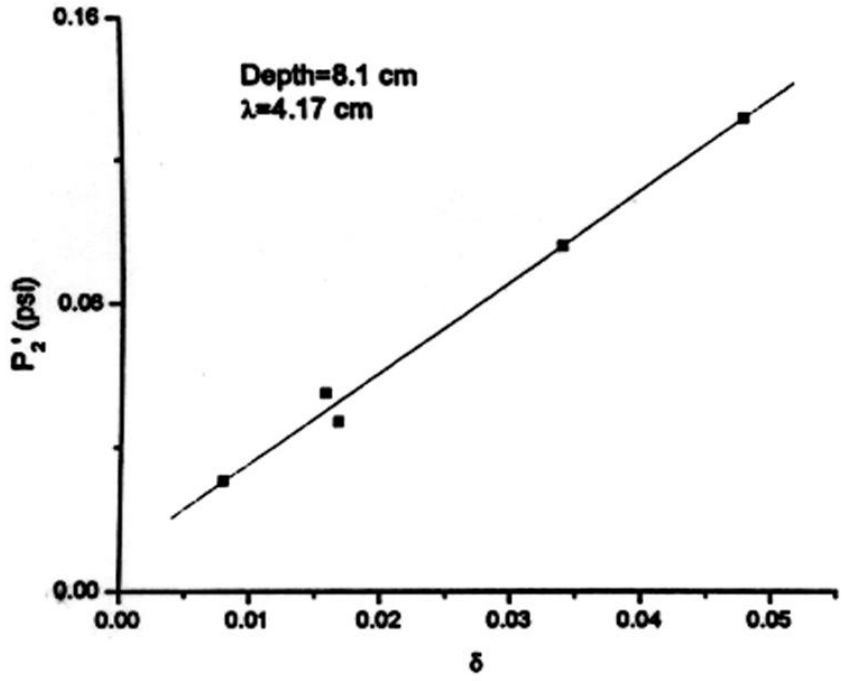

Fig. 4.11: Linear dependence of P_2' on measured delta for shallow depths.

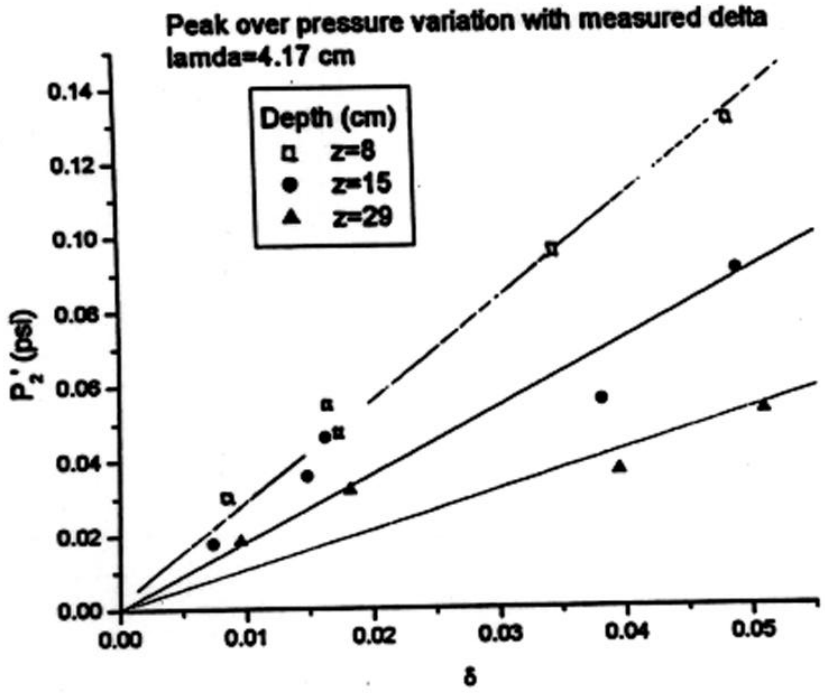

Fig. 4.12: P_2' verses δ for different depths

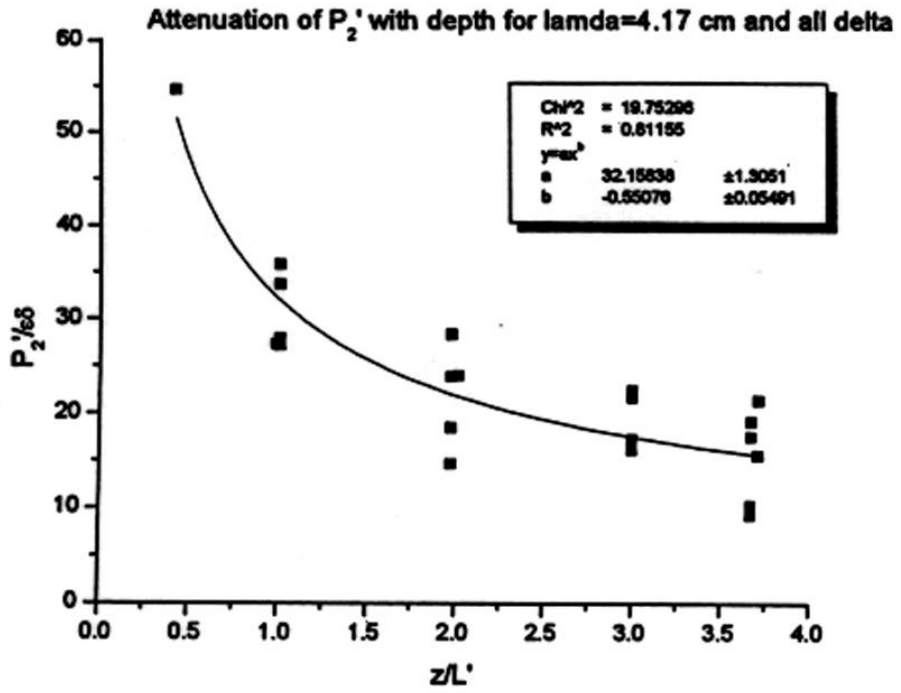

Fig. 4.13: Normalized attenuation of P_2'

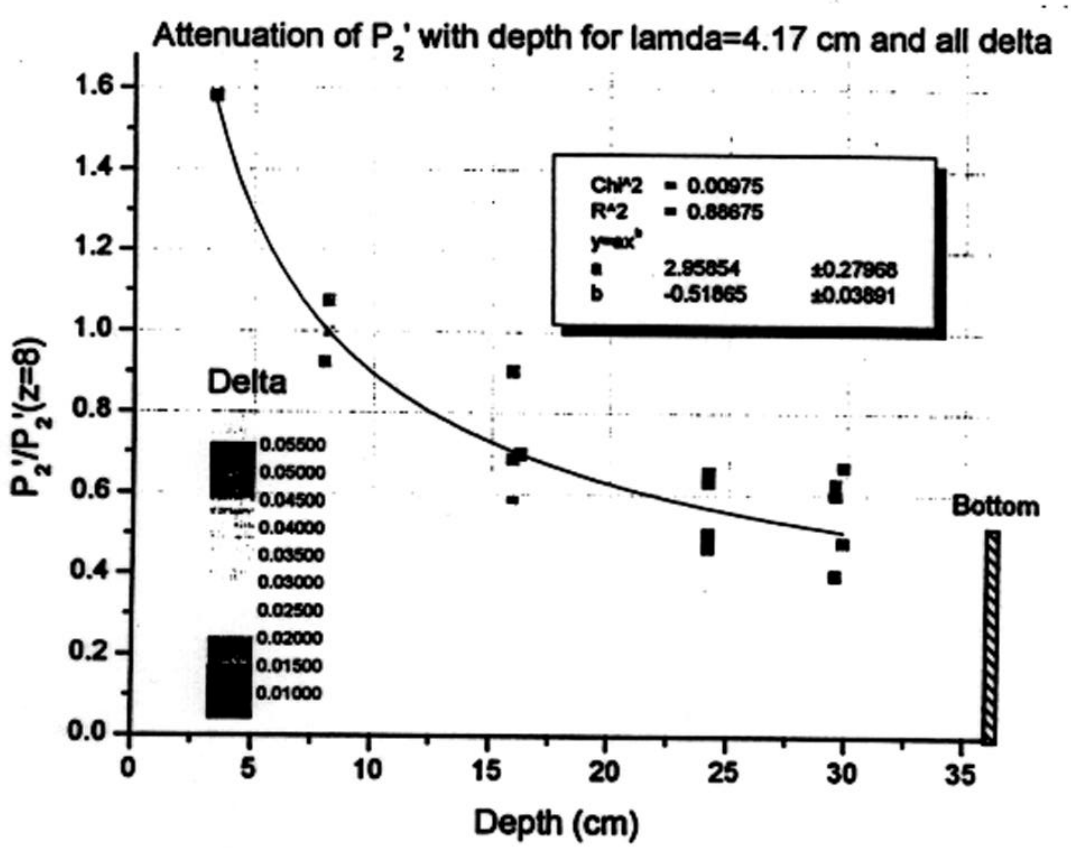

Fig. 4.14 : P_2' normalized by the measured P_2' at z=8 cm (1 signature depth)

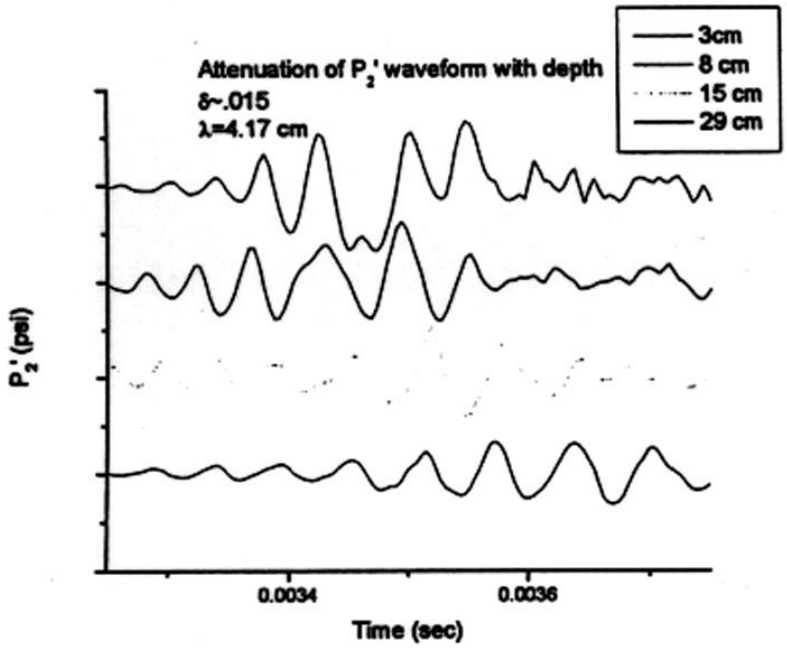

Fig. 4.15 : Pressure time traces of P_2' for 4 different depths, all else constant.

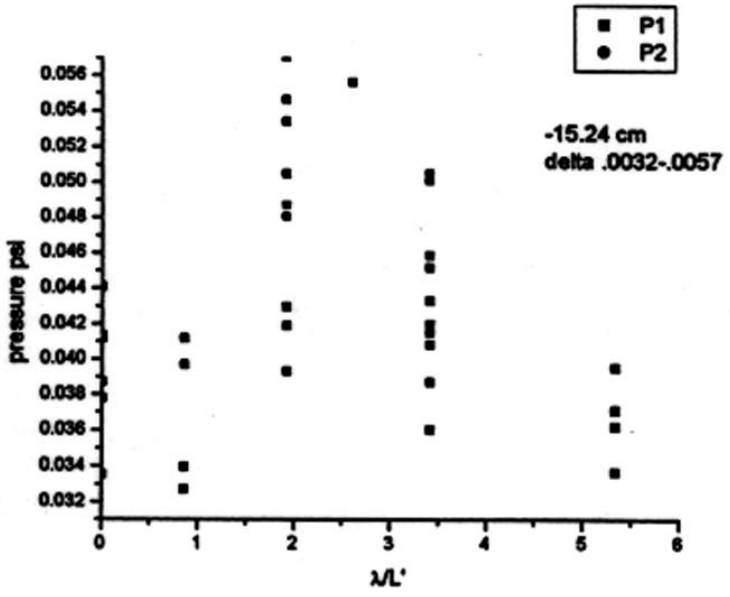

Fig. 4.16 : Preliminary peak measured pressure for probes at 2 different streamwise positions vrs. λ/L' based on older data acquisition and laboratory setup.

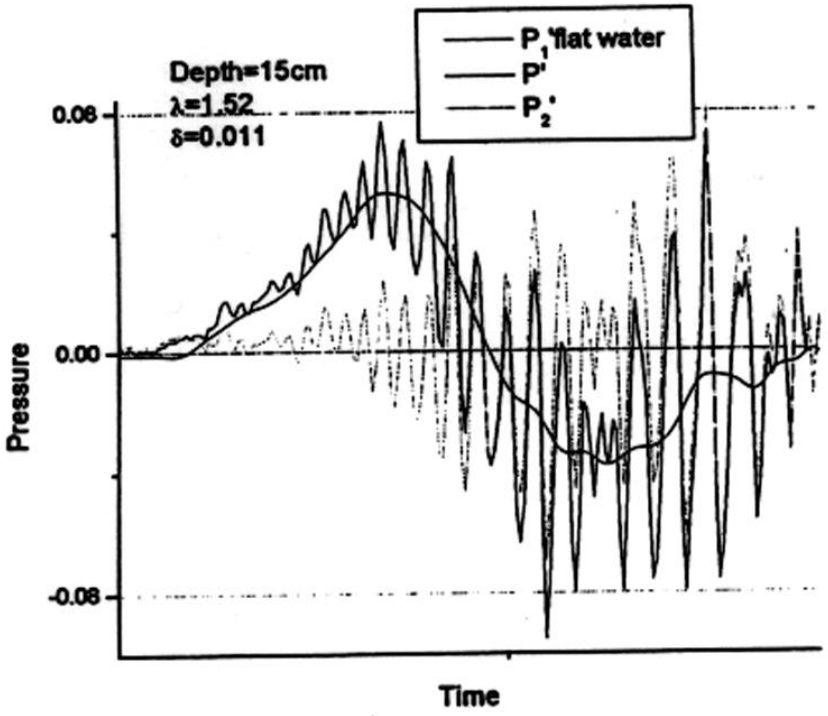

Fig. 4.17: Newer data for λ=1.52 cm and parameters indicated

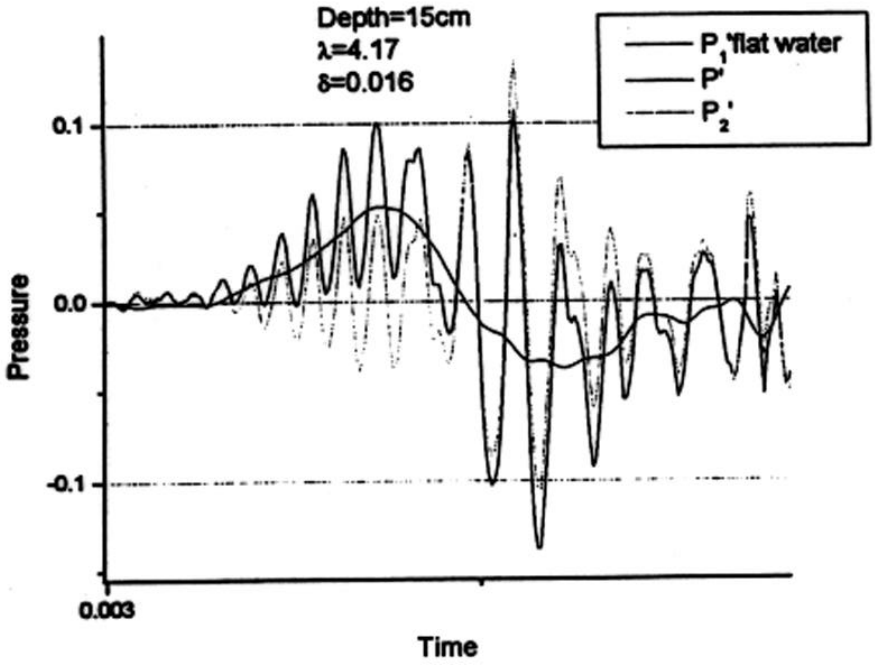

Fig. 4.18 : Newer data for λ=4.17 cm and parameters indicated

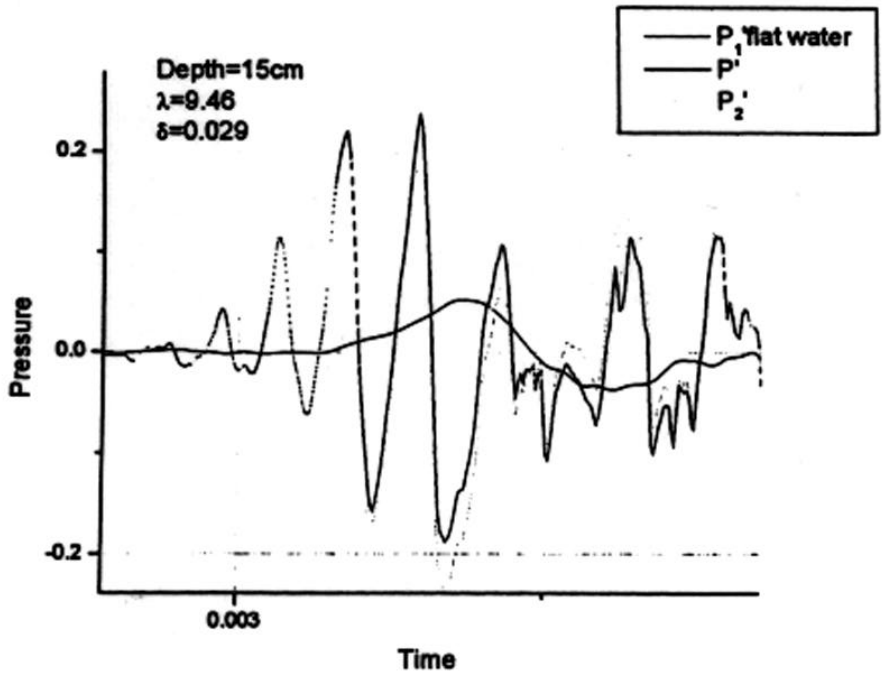

Fig. 4.19: Newer data for λ=9.46 cm and parameters indicated

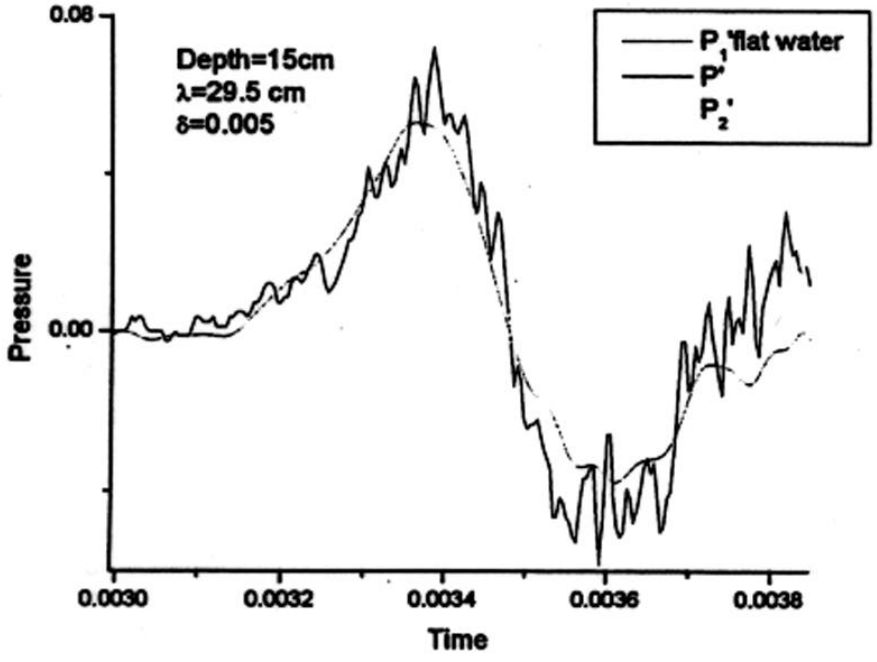

Fig. 4.20: Newer data for λ=29.5 cm and parameters indicated

Focus 1: PCBoom original plume model, focus

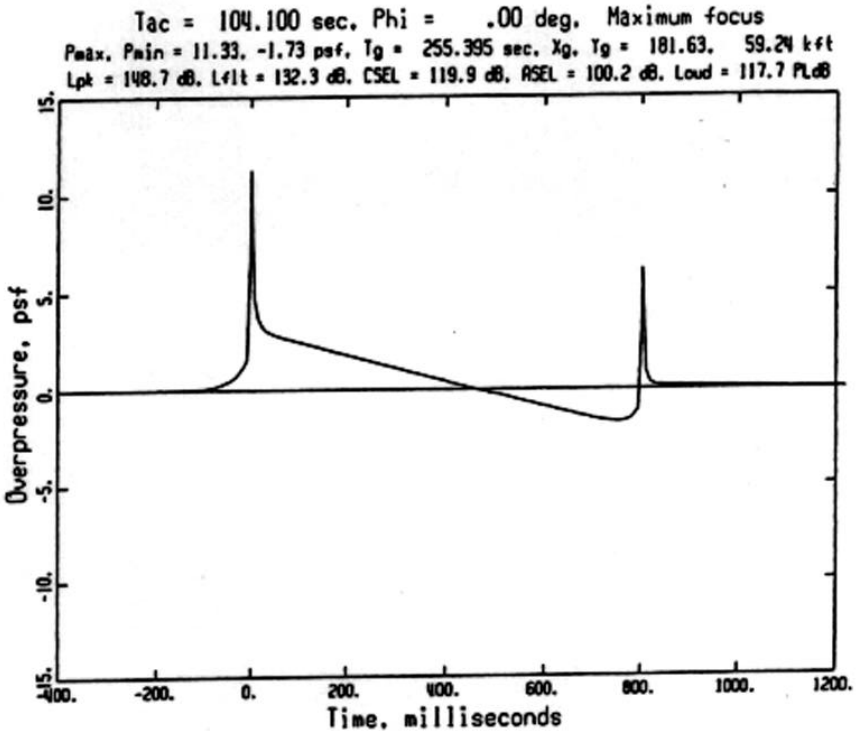

Fig. 5.1a

Carpet 1: PCBoom original plume model, carpet

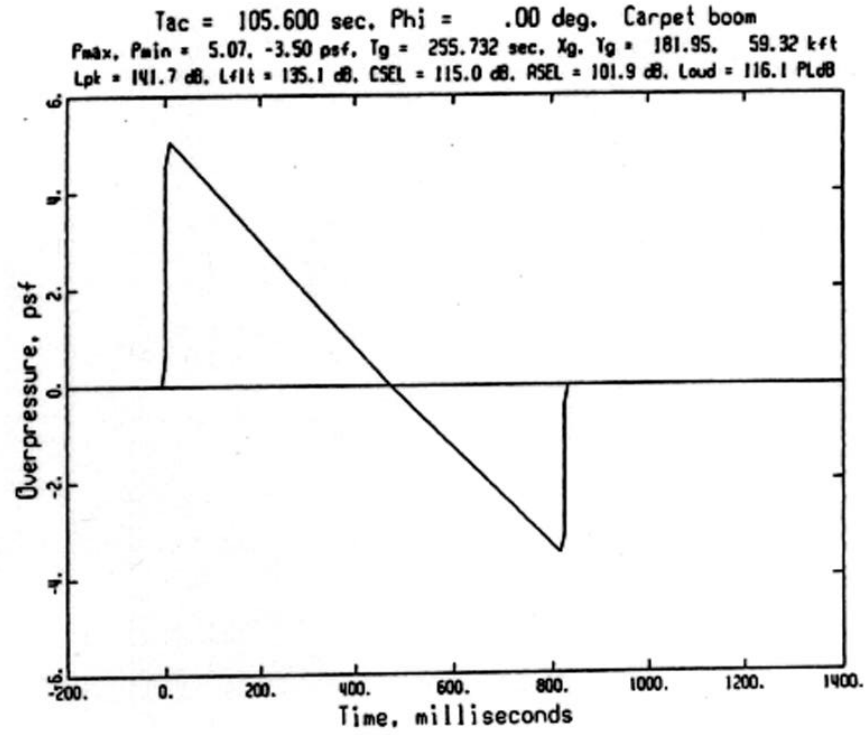

Fig. 5.1b

Focus 2: Thomas mode, wind tunnel source, focus:

Fig. 5.2a

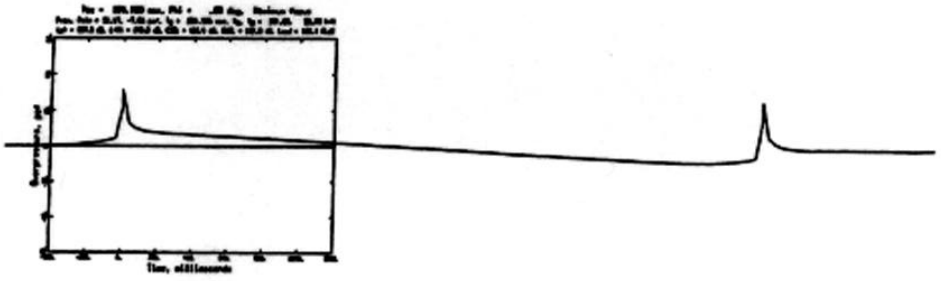

Carpet 2: Thomas mode, wind tunnel source, carpet:

Fig. 5.2b

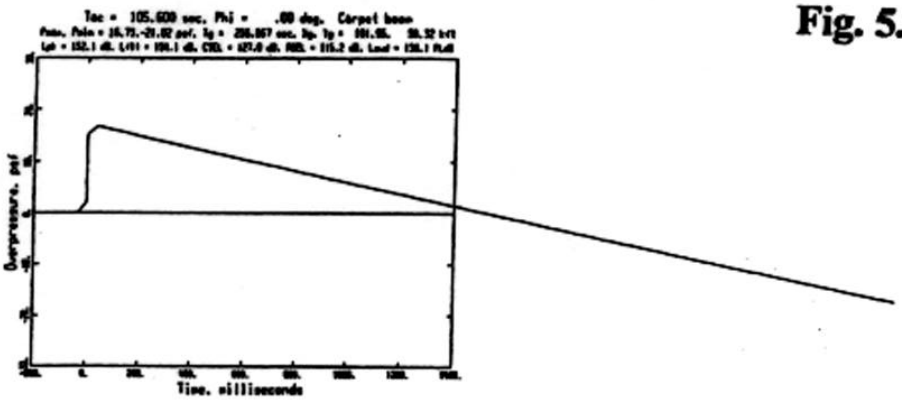

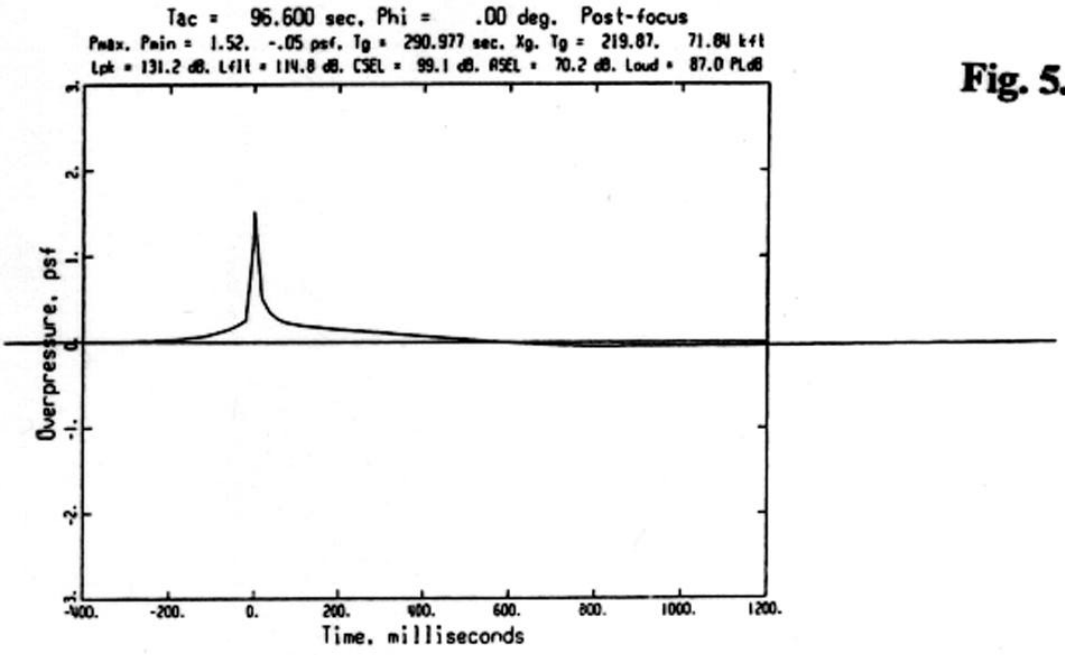

Fig. 5.4

Focus 3: PCBoom revised plume model, focus

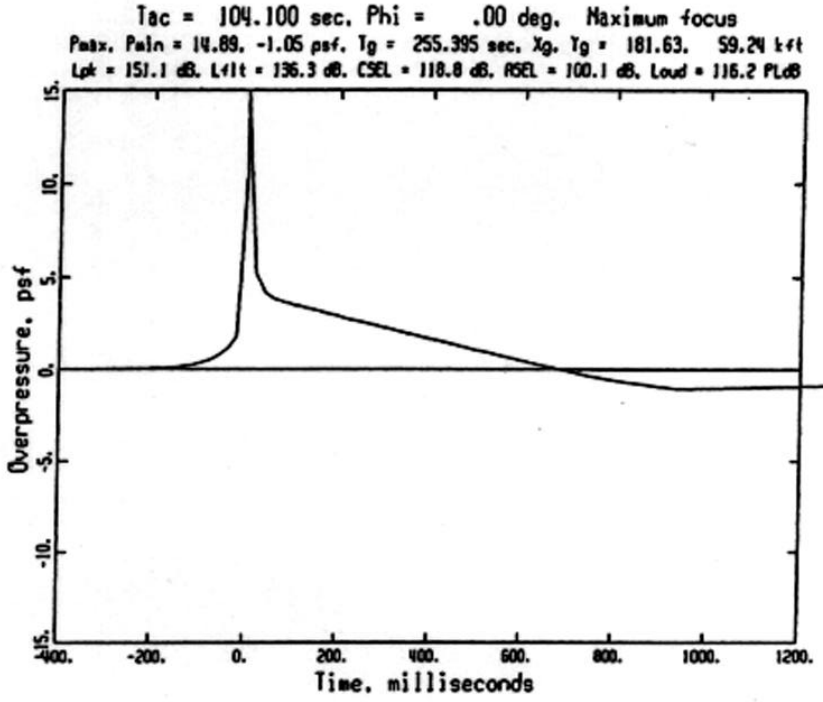

Fig. 5.3a

Carpet 3: PCBoom revised plume model, carpet

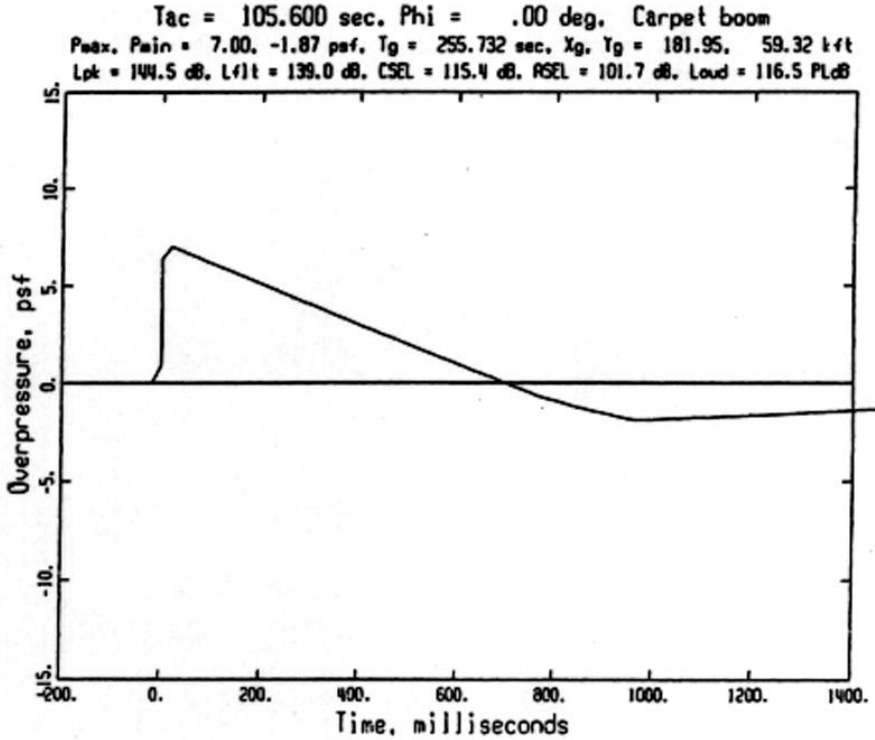

Fig. 5.3b

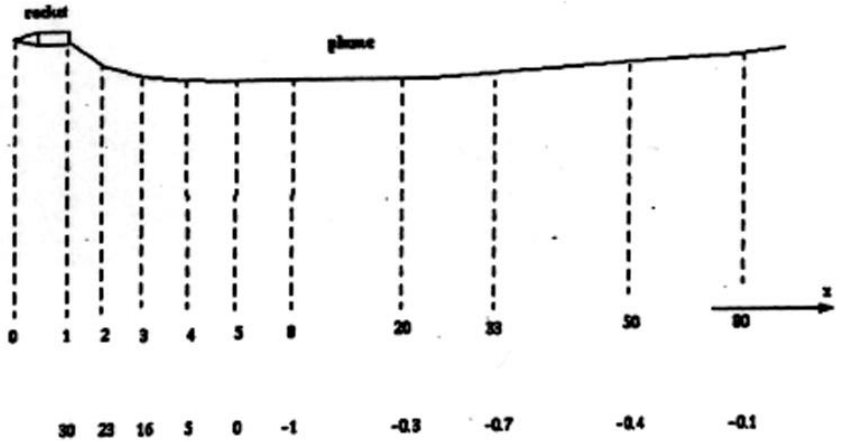

Fig. 5.5a

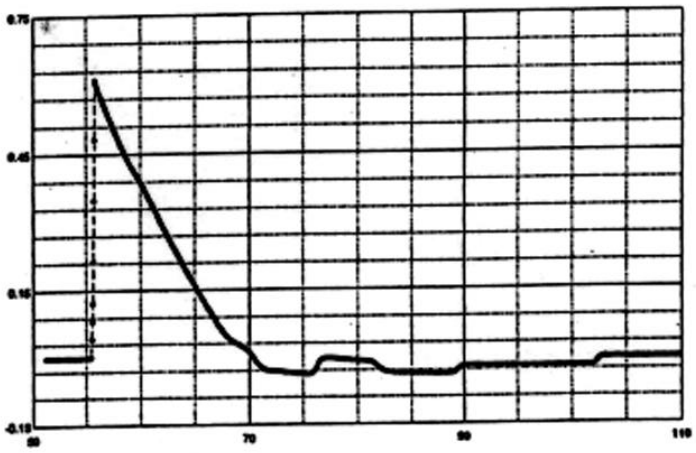

Fig. 5.5b

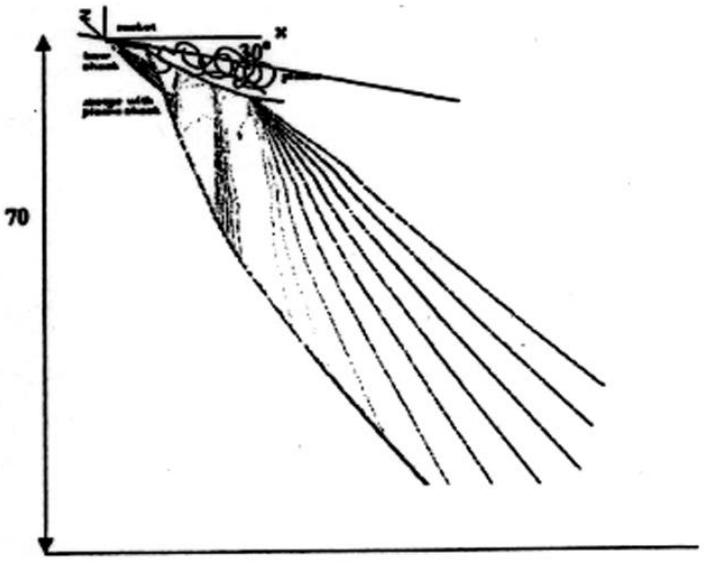

Fig. 5.5c

The signature is captured at the incidence that Mach number is 2.5, inclination angle is 30 degrees, and the rocket is 70 body length units above the ground.

Fig.5.6

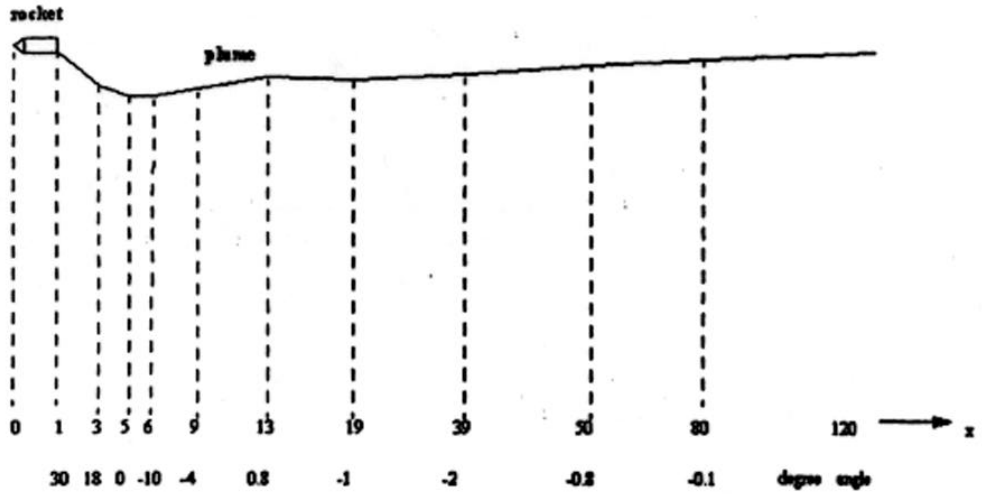

(a)

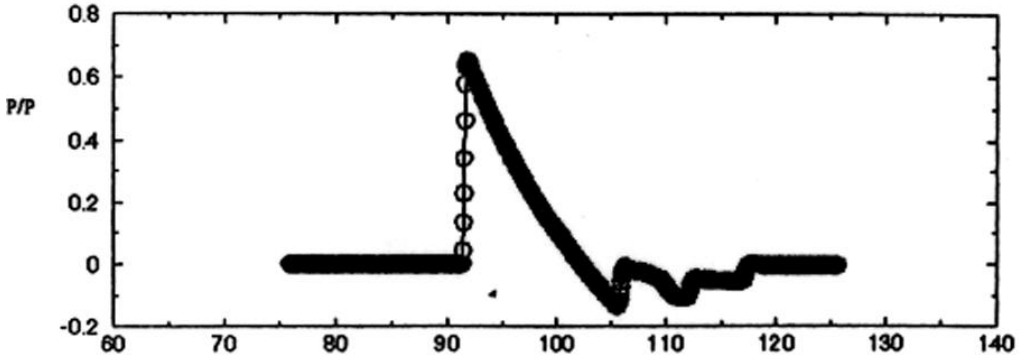

(b)

Fig. 5.7

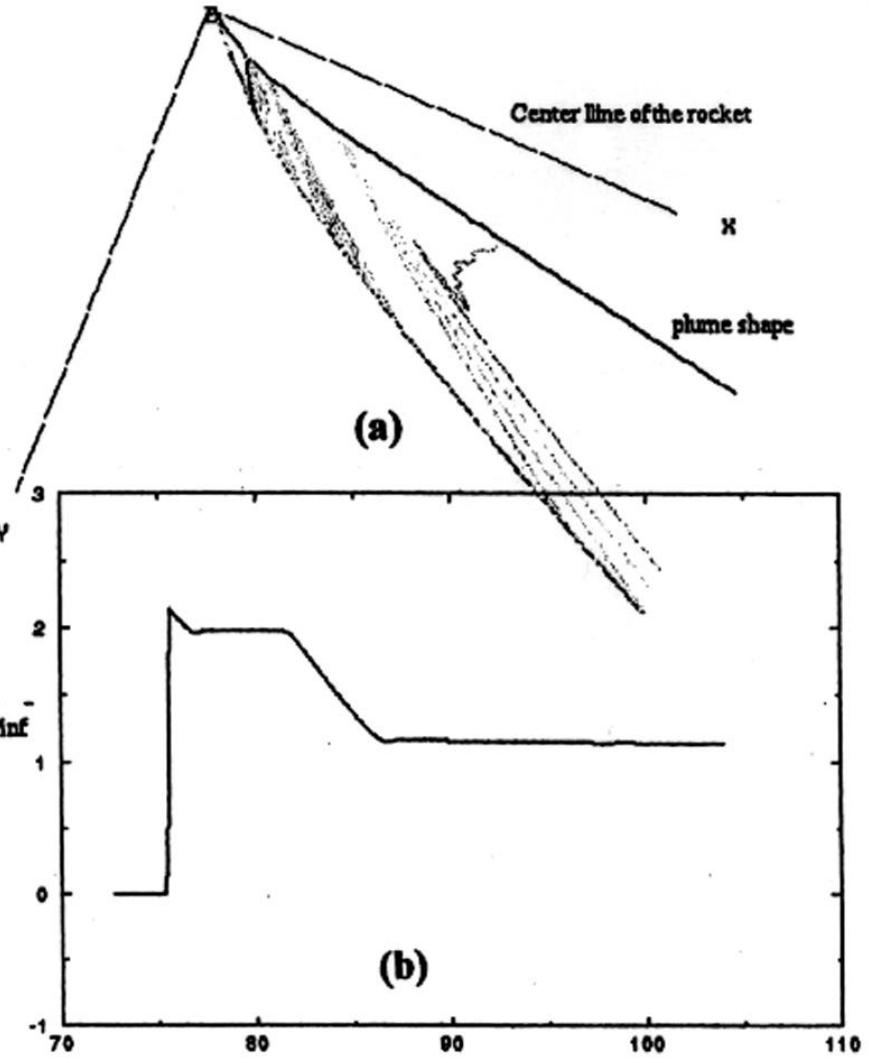

The flight path is 45 degrees. In this scale, you can't see the rocket, all you can see is the plume shape. This plume just expanses and doesn't contract come back to the center line as you wanted on the phone. The boom shape doesn't go to zero.

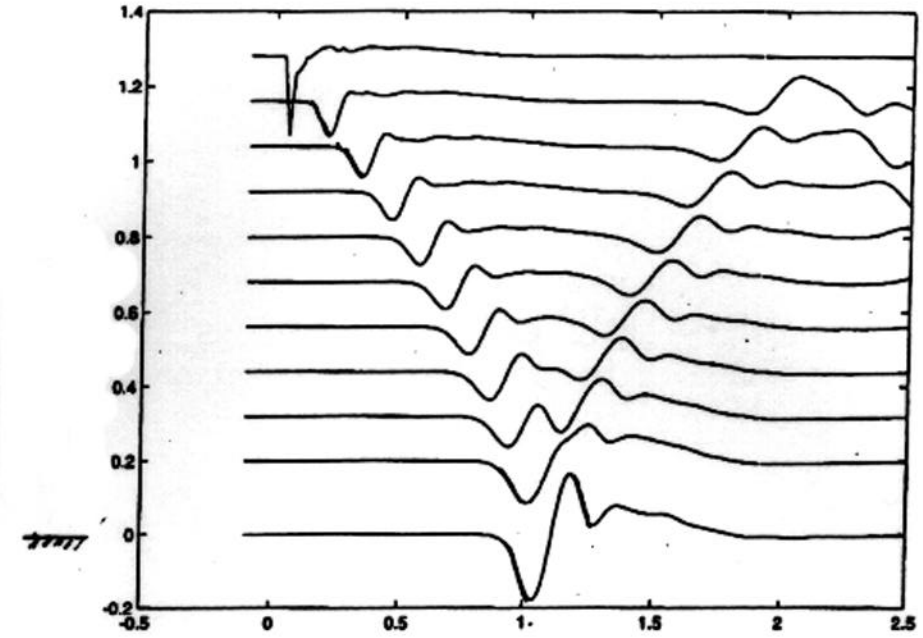

Fig. 5.8a

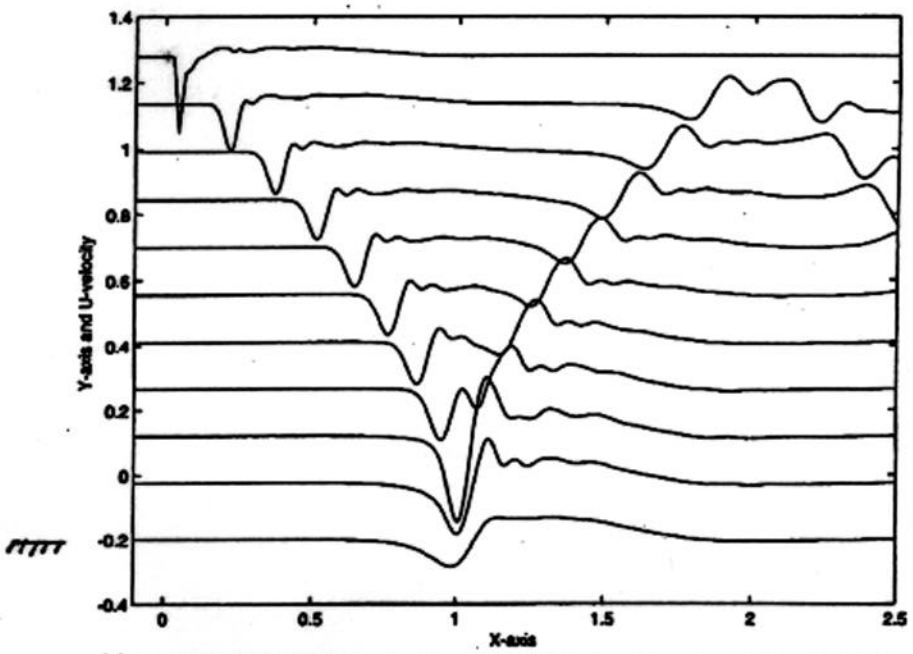

Fig. 5.8b

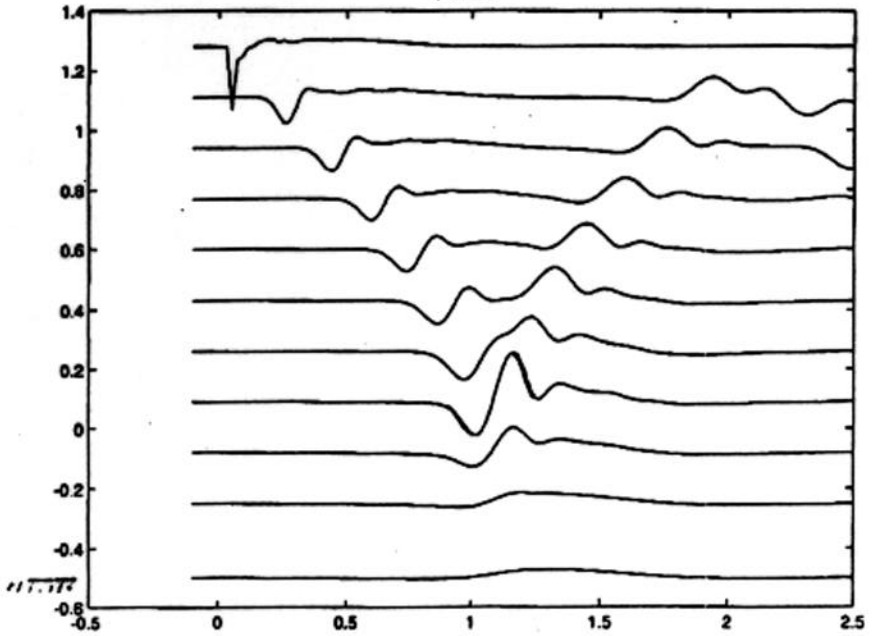

Fig. 5.8c

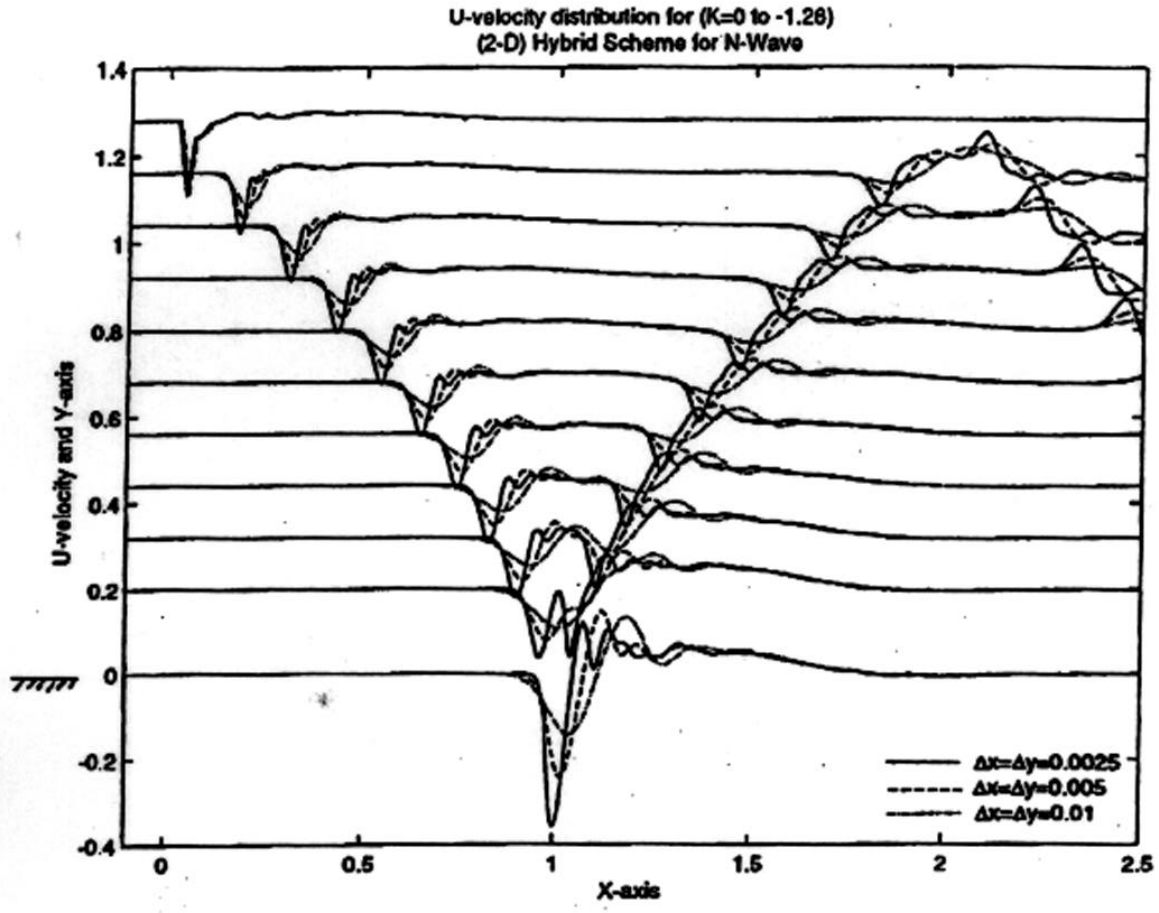

Fig.5.9

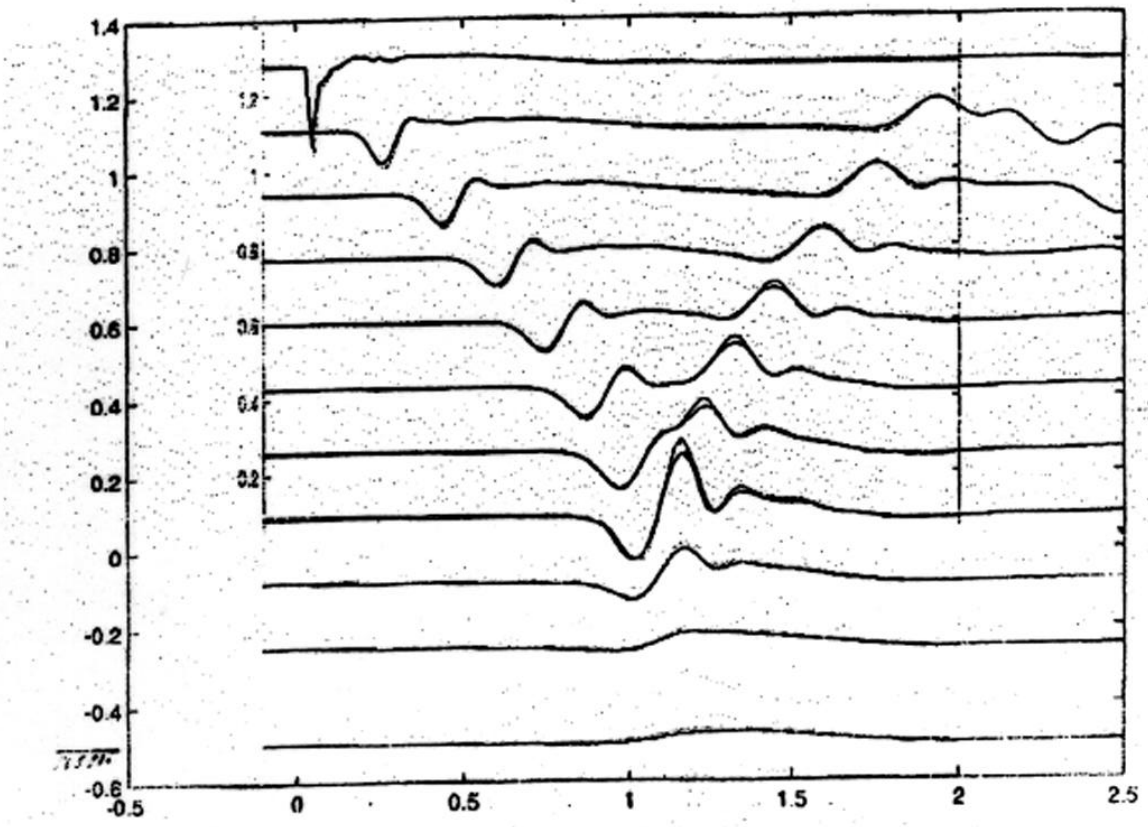

Fig. 5.10

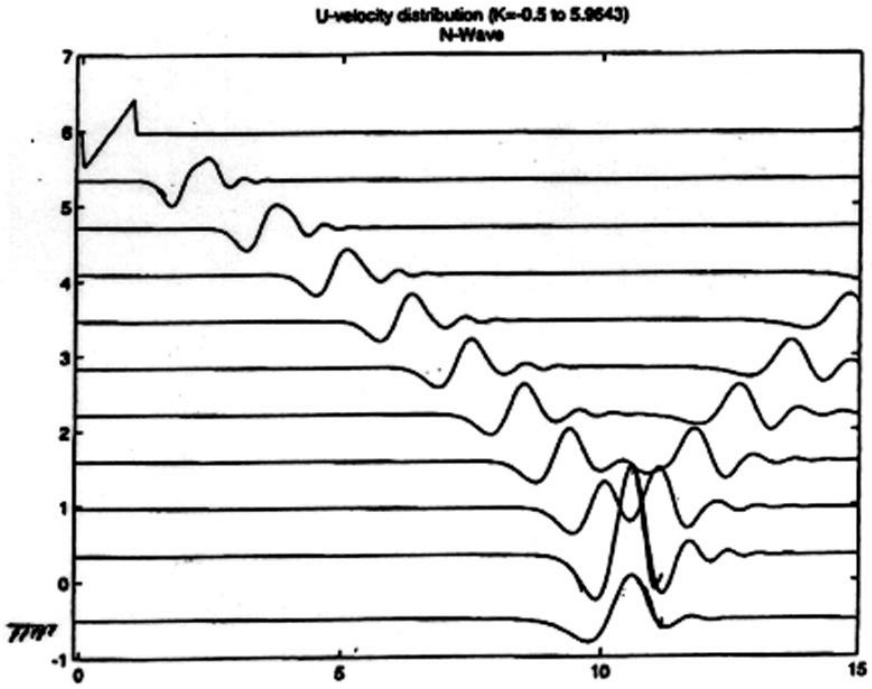

Fig. 5.11a

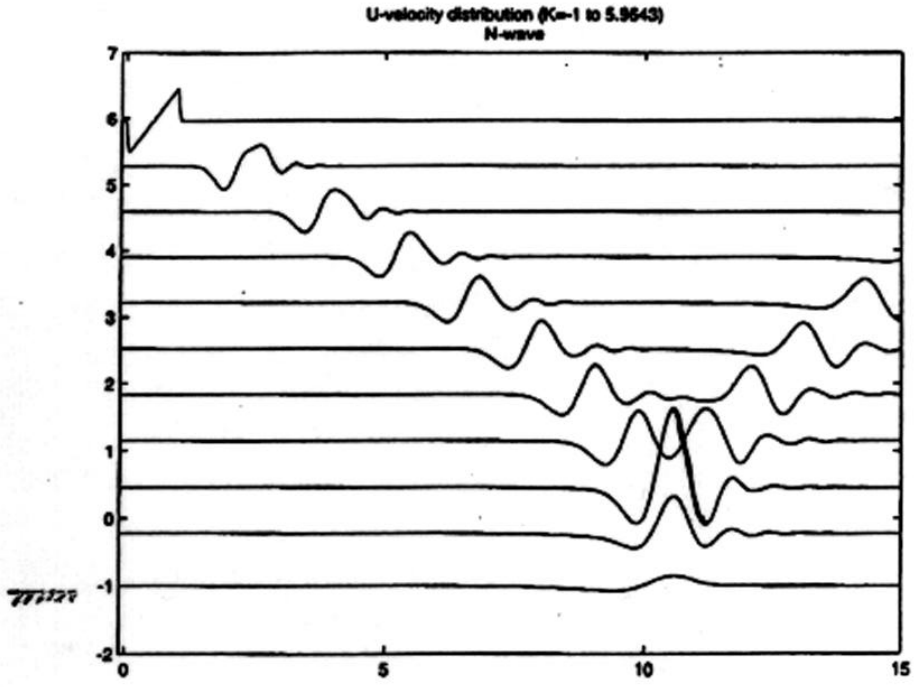

Fig. 5.11b

Appendix I Computer program files: Major wavy-ocean codes used in Sec. 3

```
c    General 2D Sawyers Solution

c    same as 2d_gen1.for, but with the Po input in function

          parameter (nmax=50000)
          implicit real *8(a-h,o-z)
          character *80 name
          real *8 M

          print *,'output file name='
          read(*,2) name
 2        format(a80)

          open(unit=2,status='unknown',file=name)

          pi  =4.0*atan(1.0d0)

          print *,'M='
          read(*,*) M

          print *,'xbegin='
          read(*,*) xbegin
          print *,'xend='
          read(*,*) xend
          print *,'dx='
          read(*,*) dx

          nx=(xend-xbegin)/dx
          print *,'nx='
          read(*,*) nx
          dx=(xend-xbegin)/nx

          print *,'Z/L='
          read(*,*) zo_p

          do 12 j=1,nx
             x  =(xbegin+dx/2.0)+(j-1.0)*dx

             call s2d_gen1(M,x,zo_p,Uo_p)

             write(2,100) x,Uo_p
100          format(1x,2(1x,e13.6))
   12     continue

          stop
          end


c    function of dfdx
c    pressure at the air side surface
c    normalize to x=0-1,Pmax=1
c
         function df(x)
         implicit real *8(a-h,o-z)
         real *8 a,b,c,d,e,f,g
            a=     1.0141
            b=   -11.3424
            c=  -119.3780
            d=   128.4828
            e=   124.3188
            f=    64.4171
```

```
            g=  2337.9188
            if(x .lt. 0.0000)                          df=0.0
            if(x .ge. 0.0000 .and. x .lt. 0.0001) df=10000.0*x
            if(x .gt. 0.0001 .and. x .le. 1.0000) then
               df=(a+b*x+c*x*x+d*x*x*x)/(1.0+e*x+f*x*x+g*x*x*x)
            end if
            if(x .gt. 1.0) df=0.0

c     change from P to U
            df=-df

C           b=0.0001
C           if(x .lt. 0.0) df=0.0
C           if(x .gt. 0.0 .and. x .le. b) df=-x/b
C           if(x .gt. b  .and. x .le. (1.0-b)) df=(1.0-2.0*x)/(2.0*b-1.0)
C           if(x .gt. (1.0-b) .and. x .le. 1.0) df=(1.0-x)/b
C           if(x .gt. 1.0) df=0.0

         return
         end


         subroutine s2d_gen1(M,xx,zo,u2d)
c     same as under-2d-gen.f, but with add and subtract

c
c     general 2-D problem, the pressure is given in input.dat
c     program for under water sonic boom with infinit depth
c
          implicit real *8(a-h,o-z)
          parameter (nx=10001)
          complex *16 z2d,sum,ci,clog1
          real *8 M0,M
          real *8 x(nx),u0(nx)
          common pi

          pi=4.0d0*datan(1.0d0)
          ci=(0.0d0,1.0d0)

c     M0: Mach number at the air side
c
          n=2000
          dx1=1.0/n
          do 10 i=1,n
             x(i)=dx1*(i-0.5)
             u0(i)=df(x(i))
 10       continue

          M0=M/4.530d0
          beta=dsqrt(1.0d0-M0*M0)
c     change to under-water variables
          z=-zo*beta

          z2d=xx-(0.0d0,1.0d0)*z
c     find u0 at xx
          if(xx .lt. x(1)) u0xx=0.0
          if(xx .gt. x(n)) u0xx=0.0

         if(xx .ge. x(1) .and. xx .le. x(n)) then
            do 100 i1=2,n
               if(xx .ge. x(i1-1) .and. xx .lt. x(i1)) then
```

```
                  u0xx=u0(i1)
     1                 -((u0(i1)-u0(i1-1))/(x(i1)-x(i1-1)))
     2                  *(x(i1)-xx)
                  go to 110
               end if
 100        continue
         end if
 110     continue

         sum=(0.0,0.0)
         do 200 i1=1,n
            u00=u0(i1)
            x10= x(i1)
            sum=sum+(u00-u0xx)*dx1/(z2d-x10)
 200     continue
         sum=sum-u0xx*(clog1(z2d-1.0)-clog1(z2d))
         sum=sum*(0.0d0,1.0d0)/pi

         u2d= real(sum)

         return
         end

         function clog1(z)
c      good for y>0
          implicit real *8(a-h,o-z)
          complex *16 z,clog1
          common pi
             x= real(z)
             y=dimag(z)
             r=dsqrt(x*x+y*y)
             if(x .gt. 0.0d0) tha=datan(dabs(y/x))
             if(x .eq. 0.0d0) tha=pi/2.0d0
             if(x .lt. 0.0d0) tha=pi-datan(dabs(y/x))
             clog1=dlog(r)+(0.0d0,1.0d0)*tha
          return
          end
```

```
c     Calculation of Phi

c     with Phi sign change, 04-01-2001
c
c     modifed from st1.for, with non-aligned effect
c     with the integration limis: from 0 to 1
c
c     Stright calculation
c
         implicit real *8(a-h,o-z)
         real *8 k,k1,k2,alpha,M,Mn,betan
         complex *16 phi,sum,fy
         complex *16 ci

         ci=(0.0,1.0)

         print *,'k='
         read(*,*) k
         print *,'M='
         read(*,*) M
         print *,'Swap angle R_Lambda='
         read(*,*) Rlam
         print *,'Align angle Psi='
         read(*,*) Psi

         print *,'xstop, xstep='
         read(*,*) xstop,xstep

         open(unit=1, status='unknown',file='phi_dat'
     1              ,form='unformatted')

         pi  =4.0*atan(1.0d0)
         Rlam=Rlam*pi/180.0
         Psi = Psi*pi/180.0
         Mn  =M*cos(Rlam)
         k1  =k*cos(Rlam+Psi)
         k2  =k*sin(Rlam+Psi)
         P   =2.0*k*Mn*Mn*cos(Rlam+Psi)
         Q   =k*k*(Mn*Mn-(1.0+Mn*Mn)*sin(Rlam+Psi)
     1                              *sin(Rlam+Psi))

         betan=dsqrt(Mn*Mn-1.0)
         alpha=sqrt(P*P-4.0*betan*betan*Q)
     1        /2.0/betan/betan

         rmu=P/2.0/betan/betan/alpha
10       continue

         nstep=xstop/xstep
         xstep=xstop/nstep
         write(1) nstep,xstep,k,M,(Rlam*180.0/pi),(Psi*180.0/pi)

         open(unit=11,status='unknown',file='phi_st.txt')

         do 500 i=1,nstep
            x=xstep*(i-0.5)

            sum=(0.0,0.0)
            dx1=0.0001
            x1beg=0.0
            x1end=x
```

```
            if(x .gt. (1.0+b)) x1end=1.0+b
            nx1=(x1end-x1beg)/dx1
            dx1=(x1end-x1beg)/nx1
            do 450 ii=1,nx1
               x1=x1beg+dx1*(ii-0.5)
               fy=cdexp(-ci*(k1-rmu*alpha)*(x-x1))*Rj0(alpha*(x-x1))
     1           *(ci*k1*df(x1)+betan*betan*ddf(x1))
               sum=sum+fy*dx1
450         continue

            phi=2.0*cdexp(ci*k1*x)*sum/betan

c   change Phi sign, 04-01-2001

            phi=-phi

            write(1) phi
            write(11,490) x,real(phi),aimag(phi)
 500      continue

 490     format(3(1x,e12.5))

         stop
         end

c   function of dfdx
c   pressure at the air side surface
c   normalize to x=0-1,Pmax=1
c
        function df(x)
        implicit real *8(a-h,o-z)
        real *8 a,b,c,d,e,f,g
           a=     1.0141
           b=   -11.3424
           c=  -119.3780
           d=   128.4828
           e=   124.3188
           f=    64.4171
           g=  2337.9188
           if(x .lt. 0.0000)                          df=0.0
           if(x .ge. 0.0000 .and. x .lt. 0.0001) df=10000.0*x
           if(x .gt. 0.0001 .and. x .le. 1.0000) then
              df=(a+b*x+c*x*x+d*x*x*x)/(1.0+e*x+f*x*x+g*x*x*x)
           end if
           if(x .gt. 1.0) df=0.0
c   change from P to U
           df=-df

        return
        end
c
        function ddf(x)
        implicit real *8(a-h,o-z)
           dx=0.0001
           xp=x+dx/2.0
           xm=x-dx/2.0
           if(x .le. 0.0) ddf=0.0
           if(x .ge. 1.0) ddf=0.0
           if(x .gt. 0.0 .and. x .lt. 1.0) then
              ddf=(df(xp)-df(xm))/dx
           end if
```

```
      return
      end

c     calculation of Bessel function J0
      function RJ0(x)
      implicit real *8(a-h,o-z)

      if(x .gt. 3.0) go to 100

c     x < 3
      z  =x/3.0
      z2 =z*z
      z4 =z2*z2
      z6 =z4*z2
      z8 =z4*z4
      z10=z8*z2
      z12=z6*z6
      RJ0=1.0-2.2499997*z2+1.2656208*z4 -0.3163866*z6
     1          +0.0444479*z8-0.0039444*z10+0.0002100*z12

      go to 200
c     x>3
 100  continue
      z =3.0/x
      z2=z*z
      z3=z2*z
      z4=z2*z2
      z5=z2*z3
      z6=z3*z3
      f0=0.79788456-0.00000077*z -0.00552740*z2
     1              -0.00009512*z3+0.00137237*z4
     2              -0.00072805*z5+0.00014476*z6
      T0=x-0.78539816-0.04166397*z -0.00003954*z2
     1                +0.00262573*z3-0.00054125*z4
     2                -0.00029333*z5+0.00013558*z6
      RJ0=f0*dcos(T0)/dsqrt(x)

 200  continue

      return
      end
```

```
c   Calculation of A(xi)

c     with Phi Sign Change, 04-01-2001
c          (1) no need to change for Phi
c
c
c     modified from st2.for, with non-aligned effect
c
c     changed from n_dint2a.for    3-19-2000
c     w/o add & subtract
c
c     with new correction, 4-1-1999
c         change from dint2_3.for
c     Dr. Cheng's one term expansion
c
c     2nd. intergal
c
          parameter (nmax=50000)
          implicit real *8(a-h,o-z)
          character *80 name
          real *8 k,k1,k2,alpha,M,Mn,betan,Mw,betaW
          real *8 Lambda
          complex *16 phi(nmax),fta,dfta,ci
          complex *16 phi_dp(nmax)
          complex *16 fy,sum,fta_ex,fta_bc,sqR1,sqR2

          print *,'input Phi file name='
          read(*,2) name
 2        format(a80)

          open(unit=1,status='unknown',file=name
     1                 ,form='unformatted')
          open(unit=2,status='unknown',file='fta_dat'
     1                 ,form='unformatted')

c     n : the total step used in 2nd integration, i.e.,
c                 the integration is from 0 to n*dx
c     dx: the integration step in 2nd integration and is given from
c                 1st integration as xstep
c     k : the wave number and is given from the output of
c                the first integration
c
c     M: the Mach number in the air side
c
c     the input file contains n,dx,k,M and complex phi(x), and
c                is provided by 1st integration
c

          read(1) n,dx,k,M,dRlam,dPsi
          print *,'n,dx,k,M,Rlambda,Psi',n,dx,k,M,dRlam,dPsi
          do 10 i=1,n
             read(1) phi(i)
 10       continue
          ci  =(0.0,1.0d0)
          pi  =4.0*atan(1.0d0)
          Rlam=dRlam*pi/180.0
          Psi = dPsi*pi/180.0
          Mn  =M*cos(Rlam)
          k1  =k*cos(Rlam+Psi)
          k2  =k*sin(Rlam+Psi)
          P   =2.0*k*Mn*Mn*cos(Rlam+Psi)
```

```
      Q    =k*k*(Mn*Mn-(1.0+Mn*Mn)*sin(Rlam+Psi)
     1                            *sin(Rlam+Psi))

      betan=dsqrt(Mn*Mn-1.0)
      alpha=sqrt(P*P-4.0*betan*betan*Q)
     1      /2.0/betan/betan
      rmu  =P/2.0/betan/betan/alpha

      Lambda=2.0*pi/k1
      Mw=Mn/4.530
      betaW=sqrt(1.0-Mw*Mw)
c
c     dxi: the step size in xi, to be used in 3rd. integration as
c                                                integration step
c     xibegin: the lower limit of A(xi), to be used as lower bound
c              in 3rd. integration
c     xistop: the upper limt of A(xi), xistop=-sibegin, to be used
c              as upper bound in 3rd. integration
c
c     the output file fta.dat contains nstep,dxi,k,M,xibegin,
c              xistop and complex A(xi)
c
c     note that old file did not output k,M,xibegin and xsistop
c

      print *,'dxi, xibegin, xistop='
      read(*,*) dxi,xibegin,xistop

      print *,'xend='
      read(*,*) xend

      xxbe=-xend
      xxen= xend
      dxx =0.01
      nxx =(xxen-xxbe)/dxx
      do 12 j=1,nxx
         xx  =(xxbe+dxx/2.0)+(j-1.0)*dxx
         Uo_0=df(xx)
         Zo_p=0.0001

         call s2d_gen1(Mn,xx,zo_p,Uo_p)

         Phi_dp(j)=(Uo_p-Uo_0)/0.0001
   12    continue

      nstop =(xistop-xibegin)/dxi
      dxi=(xistop-xibegin)/nstop

      open(unit=21,status='unknown',file='fta_st.txt')

      write(2) nstop,dxi,k,M,xibegin,xistop,dRlam,dPsi

      print *,'xibegin,xistop',xibegin,xistop

      Tk1=-Mn*alpha-alpha
      Tk2=-Mn*alpha+alpha

      print *,'TK1=',TK1
      print *,'TK2=',TK2

      do 100 i=1,nstop
```

```
            xi=xibegin+dxi*(i-0.5)
c            print *,xi
            fta=(0.0,0.0)
            sum=(0.0,0.0)
            ii=0
c   Phi contribution
 20         continue
               ii=ii+1
               x=dx*(ii-0.5)
               if(x .gt. xend) go to 30

               dfta=cdexp(ci*xi*x)*phi(ii)
               fta=fta+dfta*dx

               go to 20
 30            continue
c   Boundary-Transform Term
               do 50 j=1,nxx
               xx=(xxbe+dxx/2.0)+(j-1.0)*dxx
               fy=phi_dp(j)

               fy=fy*2.0*Lambda
               fy=fy*cdexp(ci*k1*xx)
               fy=fy*cdexp(ci*xi*xx)

               sum=sum+fy*dxx
50             continue

c   ouput in fta_dat
            sum=sum/dsqrt(2.0*pi)
            fta=fta*ci*(xi+k1)*(2.0*pi/k1)/dsqrt(2.0*pi)
            fta=fta+sum
            write(2) fta
            write(21,200) xi,real(fta),aimag(fta)
200         format(3(1x,e12.5))

 100     continue

         stop
         end


c   function of dfdx
c   pressure at the air side surface
c   normalize to x=0-1,Pmax=1
c
        function df(x)
        implicit real *8(a-h,o-z)
        real *8 a,b,c,d,e,f,g
           a=     1.0141
           b=   -11.3424
           c=  -119.3780
           d=   128.4828
           e=   124.3188
           f=    64.4171
           g=  2337.9188
           if(x .lt. 0.0000)                          df=0.0
           if(x .ge. 0.0000 .and. x .lt. 0.0001) df=10000.0*x
           if(x .gt. 0.0001 .and. x .le. 1.0000) then
              df=(a+b*x+c*x*x+d*x*x*x)/(1.0+e*x+f*x*x+g*x*x*x)
           end if
```

```
            if(x .gt. 1.0) df=0.0

c    change from P to U
            df=-df

          return
          end


          subroutine s2d_gen1(M,xx,zo,u2d)
c       same as under-2d-gen.f, but with add and subtract

c
c       general 2-D problem, the pressure is given in input.dat
c       program for under water sonic boom with infinit depth
c
           implicit real *8(a-h,o-z)
           parameter (nx=10001)
           complex *16 z2d,sum,ci,clog1
           real *8 M0,M
           real *8 x(nx),u0(nx)
           common pi

           pi=4.0d0*datan(1.0d0)
           ci=(0.0d0,1.0d0)

c       M0: Mach number at the air side
c
           n=2000
           dx1=1.0/n
           do 10 i=1,n
              x(i)=dx1*(i-0.5)
              u0(i)=df(x(i))
 10        continue

           M0=M/4.530d0
           beta=dsqrt(1.0d0-M0*M0)
c       change to under-water variables
           z=-zo*beta

           z2d=xx-(0.0d0,1.0d0)*z
c       find u0 at xx
           if(xx .lt. x(1)) u0xx=0.0
           if(xx .gt. x(n)) u0xx=0.0

          if(xx .ge. x(1) .and. xx .le. x(n)) then
             do 100 i1=2,n
                if(xx .ge. x(i1-1) .and. xx .lt. x(i1)) then
                   u0xx=u0(i1)
     1                  -((u0(i1)-u0(i1-1))/(x(i1)-x(i1-1)))
     2                   *(x(i1)-xx)
                   go to 110
                end if
 100         continue
          end if
 110      continue

          sum=(0.0,0.0)
          do 200 i1=1,n
             u00=u0(i1)
             x10= x(i1)
```

```
            sum=sum+(u00-u0xx)*dx1/(z2d-x10)
  200       continue
            sum=sum-u0xx*(clog1(z2d-1.0)-clog1(z2d))
            sum=sum*(0.0d0,1.0d0)/pi

            u2d= real(sum)

            return
            end

            function clog1(z)
c       good for y>0
             implicit real *8(a-h,o-z)
             complex *16 z,clog1
             common pi
                x= real(z)
                y=dimag(z)
                r=dsqrt(x*x+y*y)
                if(x .gt. 0.0d0) tha=datan(dabs(y/x))
                if(x .eq. 0.0d0) tha=pi/2.0d0
                if(x .lt. 0.0d0) tha=pi-datan(dabs(y/x))
                clog1=dlog(r)+(0.0d0,1.0d0)*tha
             return
             end
```

```
c   Calculation of P2
c
c   no need to chang Phi Sign, 01-04-2001
c
c   modified from st3.for, with non-aligned effect
c
c   need to correct the sign of P
c   corrected according to n_dint3a.for 9-10-2000
c
c       changed from n_dint3a.for
c
c       with the most recently correction, 4-1-1999
c       sigma(xi) is in exp. form
c
c     with the boundary-transform correation
c     3rd intergal
c
c
        implicit real *8(a-h,o-z)
        parameter (nmax=100000)
        character *80 name
        real *8 k,k1,k2,alpha,M,Mn,betan,MW

        real *8 xi(nmax)
        complex *16 A(nmax)
        complex *16 sum,ci
        complex *16 sig

        common k,M,dx,xbegin,nstop,n,Rlam,Psi

        print *,'input A(Xi) file name='
        read(*,2) name
2       FORMAT(A80)

        open(unit=2,status='unknown',file=name,form='unformatted')

        read(2) n,dxi,k,M,xibegin,xistop,dRlam,dPsi
        print *,'n,dxi,k,M,xibegin,xistop  '
        print *,'dxi,xibegin,xistop',dxi,xibegin,xistop,dRlam,dPsi

        ci  =(0.0,1.0d0)
        pi  =4.0d0*datan(1.0d0)
        Rlam=dRlam*pi/180.0
        Psi = dPsi*pi/180.0
        Mn  =M*cos(Rlam)
        k1  =k*cos(Rlam+Psi)
        k2  =k*sin(Rlam+Psi)
        P   =2.0*k*Mn*Mn*cos(Rlam+Psi)
        Q   =k*k*(Mn*Mn-(1.0+Mn*Mn)*sin(Rlam+Psi)
     1                              *sin(Rlam+Psi))

        betan=dsqrt(Mn*Mn-1.0)
        alpha=sqrt(P*P-4.0*betan*betan*Q)
     1       /2.0/betan/betan
        rmu  =P/2.0/betan/betan/alpha
c   read in A(Xi)
        do 10 i=1,n
           xi(i)=xibegin+dxi*(i-0.5)
           read(2) A(i)
10      continue
```

```
      print *,'z='
      read(*,*) z

      Mw   =Mn/4.530
      betaw=sqrt(1.0-Mw*Mw)
      Pw   =2.0*k*Mw*Mw*cos(Rlam+Psi)
      Qw   =k*k*(Mw*Mw-(1.0+Mw*Mw)*sin(Rlam+Psi)
     1                              *sin(Rlam+Psi))
      print *,'Pw,Qw=',Pw,Qw

      print *,'dx,xbegin,xstop='
      read(*,*) dx,xbegin,xstop

      nstop =(xstop-xbegin)/dx
      print *,'nstop=',nstop
      read(*,*) nstop
      dx=(xstop-xbegin)/nstop

      open(unit=11,status='unknown',file='p2_st.txt')

      do 100 i=1,nstop
         x=xbegin+dx*(i-0.5)
c     finite part
         sum=(0.0,0.0)

c     loop over xi
         do 20 ii=1,n
            xii=xi(ii)
c
c             rsig=betaw*betaw*xii*xii+Pw*xii-Qw
c   sign change according to n_dint3a.for
c
            rsig=betaw*betaw*xii*xii-Pw*xii-Qw
            if(rsig .lt. 0.0) then
               rsig=dsqrt(abs(rsig))
               sig=cdexp(ci*rsig*z)
            else
               rsig=dsqrt(abs(rsig))
               sig=dexp(-rsig*z)
            end if

            sum=sum+cdexp(-ci*xii*x)*A(ii)*sig
 20      continue

         sum=sum*dxi
         sum=sum/dsqrt(2.0*pi)

         write(11,*) x,real(sum),aimag(sum)

 100   continue
c     far field behavior
       call far(A,z,xi)

       stop
       end

c   far-field behavior
       subroutine far(A,z,xi)
       implicit real *8(a-h,o-z)
       parameter (nmax=100000)
       real *8 k,k1,k2,alpha,M,Mn,beta,Mw
```

```
      real *8 xi(nmax)
      complex *16 A(nmax),p2far,ci,Axis1

      common k,M,dx,xbegin,nstop,n,Rlam,Psi

      open(unit=41,status='unknown',file='P2_far.txt')
      print *,'dx,xbegin,nstop',dx,xbegin,nstop
      print *,'k,M,Rlam,Psi',k,M,Rlam,Psi

         ci  =(0.0,1.0d0)
         pi  =4.0d0*datan(1.0d0)
         Mn  =M*cos(Rlam)
         k1  =k*cos(Rlam+Psi)
         k2  =k*sin(Rlam+Psi)
         P   =2.0*k*Mn*Mn*cos(Rlam+Psi)
         Q   =k*k*(Mn*Mn-(1.0+Mn*Mn)*sin(Rlam+Psi)
     1                                *sin(Rlam+Psi))

         betan=dsqrt(Mn*Mn-1.0)
         print *,'betan=',betan
         alpha=sqrt(P*P-4.0*betan*betan*Q)
     1     /2.0/betan/betan
         rmu  =P/2.0/betan/betan/alpha

         Mw=Mn/4.530
         Pw=2.0*k*Mw*Mw*cos(Rlam+Psi)
         Qw=k*k*(Mw*Mw-(1.0+Mw*Mw)*sin(Rlam+Psi)
     1                             *sin(Rlam+Psi))
         print *,'Pw,Qw=',Pw,Qw
         betaw=dsqrt(1.0d0-Mw*Mw)
         print *,'betaw=',betaw
         Sw_2=Pw*Pw+4.0*betaw*betaw*Qw
         if(Sw_2 .le. 0.0) return
         Sw   =dsqrt(Pw*Pw+4.0*betaw*betaw*Qw)
         do 1000 i=1,nstop
            x=xbegin+dx*(i-0.5)

            eta =x/betaW/z
            zbar=betaW*z
c
c             xis1=(-Pw-Sw*eta/dsqrt(1.0+eta*eta))/2.0/betaW/betaW
c   sign change 5-22-2000
c
            xis1=(Pw-Sw*eta/dsqrt(1.0+eta*eta))/2.0/betaw/betaw

c     calculate A(xi) at xis1
            do 200 ii=1,n
               if(xis1 .ge. xi(ii) .and.
     1            xis1 .lt. xi(ii+1)) then
               Axis1=A(ii)
     1               +(A(ii+1)-A(ii))/(xi(ii+1)-xi(ii))
     2                *(xis1-xi(ii))
               go to 250
               end if
 200        continue
 250        continue

c
c             dummy=(Sw/2.0/betaW/betaW)
c     1            *(dsqrt(1.0+eta*eta)+Pw*eta/Sw)*zbar-pi/4.0
```

```
c    sign change 5-22-2000
c
                dummy=(Sw/2.0/betaw/betaw)
     1                *(dsqrt(1.0+eta*eta)-Pw*eta/Sw)*zbar-pi/4.0

                p2far=sqrt(Sw)*Axis1/dsqrt(2.0d0)/betaw/sqrt(zbar)
     1                                 /((1.0+eta*eta)**0.75)
                p2far=p2far*cdexp(ci*dummy)

                write(41,2000)x,real(p2far),aimag(p2far)

 1000         continue
2000         format(3(1x,e15.6))

           return
           end
```

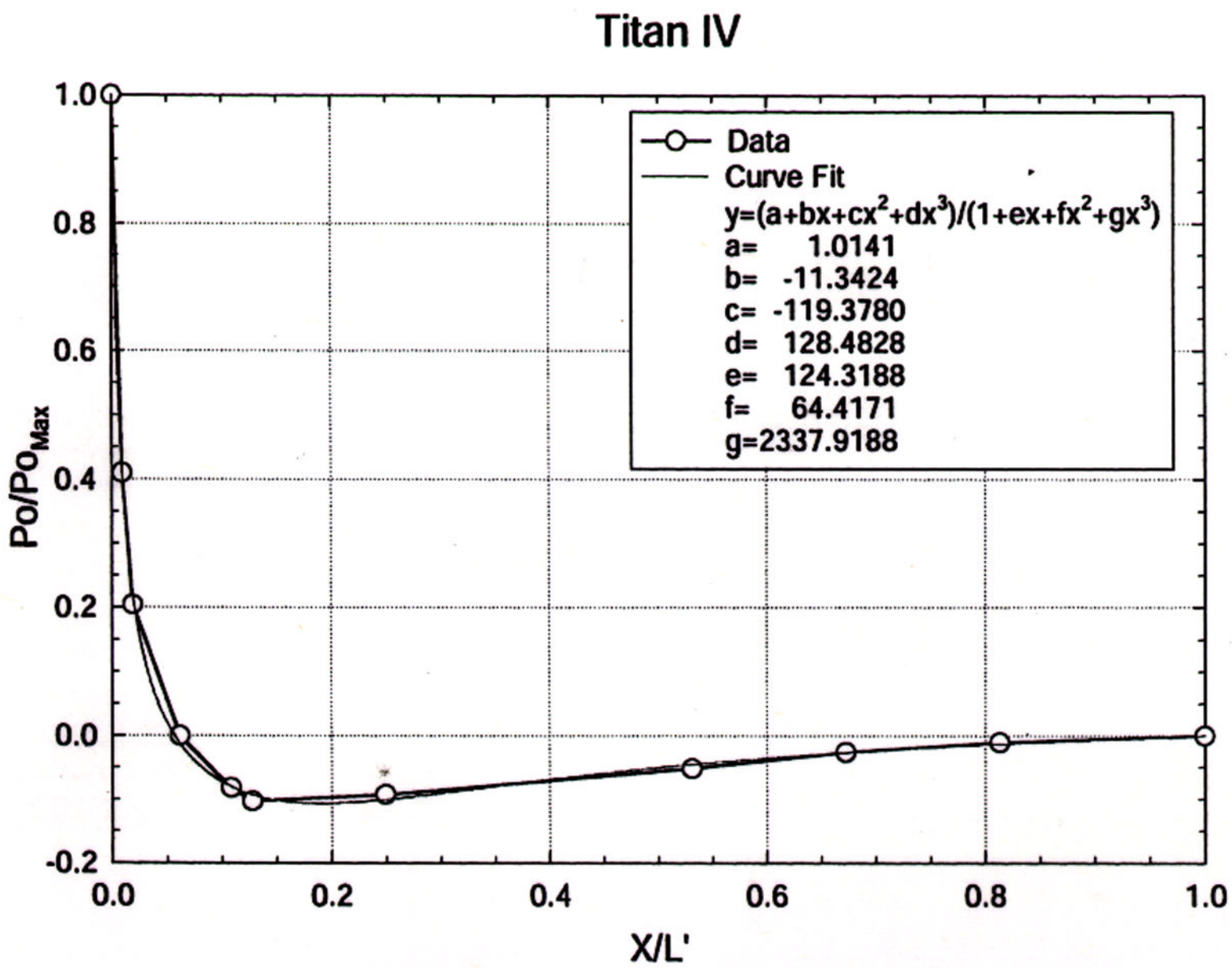
Titan IV
Data
Curve Fit
y=(a+bx+cx²+dx³)/(1+ex+fx²+gx³)
a= 1.0141
b= -11.3424
c= -119.3780
d= 128.4828
e= 124.3188
f= 64.4171
g=2337.9188
Po/Po_Max
X/L'
1.0
0.8
0.6
0.4
0.2
0.0
-0.2
0.0
0.2
0.4
0.6
0.8
1.0

Appendix II Computer program files: CFD super boom codes used in Sec. 5

```
PROGRAM TRANSONIC2D3
  IMPLICIT NONE
DOUBLE PRECISION, DIMENSION (200) :: CCC,DDD,AAA,BBB
DOUBLE PRECISION, DIMENSION (350,200) :: PHI
DOUBLE PRECISION, DIMENSION (350,200) :: CK
  REAL, DIMENSION (350,200) :: UVEL,XLEN,YLEN
  INTEGER, DIMENSION (350) :: SWP
DOUBLE PRECISION :: DX,DY,F1,F2,F3,PHIYY
DOUBLE PRECISION :: RZZ,PHIX,RESMX,ARES,XTL,YTL
  INTEGER :: SWPNO,SWPLINE,SWPROW
  INTEGER :: I,J,X,Y,A,IRES,JRES

X=262
Y=97
ARES=1E-8
XTL=8.15625
YTL=3

SWPROW=0

  SWPNO=50000
  SWPLINE=4

DX=XTL/(X-1)
DY=YTL/(Y-1)

DO I=1,X
DO J=1,Y
XLEN(I,J)=(I-1)*DX-0.15625
YLEN(I,J)=(J-1)*DY
  CK(I,J)=-3
  END DO
END DO

DO I=1, X
DO J=1, Y
PHI(I,J)=0
  END DO
END DO

DO J=1, Y
DDD(J)=1
END DO

DO J=2, Y
BBB(J)=0
END DO
```

```
      DO J=1, Y-1
      AAA(J)=0
      END DO

      DO J=1, Y
      CCC(J)=0
      END DO

      A=1
      CALL THOMAS (A, Y, BBB, DDD, AAA, CCC)
      DO J=1, Y
      PHI(1,J)=CCC(J)
      END DO

      DO J=1, Y
      DDD(J)=1
      END DO

      DO J=2, Y
      BBB(J)=0
      END DO

      DO J=1, Y-1
      AAA(J)=0
      END DO

      DO J=1, Y
      CCC(J)=PHI(1,J)
      END DO

      A=1
      CALL THOMAS (A, Y, BBB, DDD, AAA, CCC)
      DO J=1, Y
      PHI(2,J)=CCC(J)
      END DO



      OPEN (UNIT=2, FILE="d:\usr\ewahba\residual_2d5_first_order.
dat")
30    SWPROW=SWPROW+1
      WRITE (6,*) SWPROW,RESMX,IRES
      WRITE (2,*) SWPROW,RESMX

      DO I=3, X

10    DDD(1)=1
      DO J=2, Y-1
```

```
      DDD(J)=(PHI(I+1,J)-PHI(I-1,J))/(DX**3)-2*CK(I,J)/(DX**2)


      PHIX=(PHI(I,J)-PHI(I-1,J))/DX
      IF (PHIX.GE.CK(I,J)) THEN
      DDD(J)=DDD(J)+2*CK(I,J)/(DX**2)-2*(PHI(I,J)-PHI(I-1,J))/(DX
**3)
      ELSE
      END IF

      PHIX=(PHI(I+1,J)-PHI(I,J))/DX
      IF (PHIX.GE.CK(I,J)) THEN
      DDD(J)=DDD(J)+CK(I,J)/(DX**2)-(PHI(I+1,J)-PHI(I,J))/(DX**3)
      ELSE
      END IF

      DDD(J)=DDD(J)-2/(DY**2)

      IF (I.EQ.X) THEN
      DDD(J)=(CK(I,J)/DX**2)-(PHI(I,J)-PHI(I-1,J))/(DX**3)
      DDD(J)=DDD(J)-2/(DY**2)
      PHIX=(PHI(I,J)-PHI(I-1,J))/DX
      IF (PHIX.LT.CK(I,J)) DDD(J)=1
      ELSE
        END IF

      END DO
      IF (XLEN(I,Y).GE.0 .AND. XLEN(I,Y).LE.1) DDD(Y)=1
      IF (XLEN(I,Y).LT.0 .OR. XLEN(I,Y).GT.1) DDD(Y)=1

      DO J=2, Y-1
      BBB(J)=1/(DY**2)
      PHIX=(PHI(I,J)-PHI(I-1,J))/DX
      IF (I.EQ.X .AND. PHIX.LT.CK(I,J)) BBB(J)=0
      END DO
      IF (XLEN(I,Y).GE.0 .AND. XLEN(I,Y).LE.1) BBB(Y)=0
      IF (XLEN(I,Y).LT.0 .OR. XLEN(I,Y).GT.1) BBB(Y)=0

      AAA(1)=-1
      PHIX=(PHI(I,1)-PHI(I-1,1))/DX
      IF (I.EQ.X .AND. PHIX.LT.CK(I,1)) AAA(1)=0
      DO J=2, Y-1
      AAA(J)=1/(DY**2)
      PHIX=(PHI(I,J)-PHI(I-1,J))/DX
      IF (I.EQ.X .AND. PHIX.LT.CK(I,J)) AAA(J)=0
      END DO

      CCC(1)=0
```

```
PHIX=(PHI(I,1)-PHI(I-1,1))/DX
IF (I.EQ.X .AND. PHIX.LT.CK(I,1)) CCC(1)=PHI(I-1,1)
DO J=2, Y-1

CCC(J)=PHI(I+1,J)*(PHI(I+1,J)-PHI(I,J))/(DX**3)
CCC(J)=CCC(J)-CK(I,J)*PHI(I+1,J)/(DX**2)
CCC(J)=CCC(J)+PHI(I-1,J)*(PHI(I,J)-PHI(I-1,J))/(DX**3)
CCC(J)=CCC(J)-CK(I,J)*PHI(I-1,J)/(DX**2)
PHIX=(PHI(I,J)-PHI(I-1,J))/DX
CCC(J)=CCC(J)+0.5*(PHIX**2)/DX
PHIX=(PHI(I+1,J)-PHI(I,J))/DX
CCC(J)=CCC(J)-0.5*(PHIX**2)/DX

PHIX=(PHI(I,J)-PHI(I-1,J))/DX
IF (PHIX.GE.CK(I,J)) THEN
CCC(J)=CCC(J)+2*CK(I,J)*PHI(I-1,J)/(DX**2)
CCC(J)=CCC(J)-2*PHI(I-1,J)*(PHI(I,J)-PHI(I-1,J))/(DX**3)
CCC(J)=CCC(J)-(PHIX**2)/DX
ELSE
CCC(J)=CCC(J)-(CK(I,J)**2)/DX
END IF

PHIX=(PHI(I+1,J)-PHI(I,J))/DX
IF (PHIX.GE.CK(I,J)) THEN
CCC(J)=CCC(J)+CK(I,J)*PHI(I+1,J)/(DX**2)
CCC(J)=CCC(J)-PHI(I+1,J)*(PHI(I+1,J)-PHI(I,J))/(DX**3)
CCC(J)=CCC(J)+0.5*(PHIX**2)/DX
ELSE
CCC(J)=CCC(J)+0.5*(CK(I,J)**2)/DX
END IF

PHIX=(PHI(I-1,J)-PHI(I-2,J))/DX
IF (PHIX.GE.CK(I,J)) THEN
CCC(J)=CCC(J)+(PHI(I-1,J)-PHI(I-2,J))*CK(I,J)/(DX**2)
CCC(J)=CCC(J)-0.5*PHI(I-1,J)*(PHI(I-1,J)-PHI(I-2,J))/(DX**3

CCC(J)=CCC(J)+0.5*PHI(I-2,J)*(PHI(I-1,J)-PHI(I-2,J))/(DX**3

ELSE
CCC(J)=CCC(J)+0.5*(CK(I,J)**2)/DX
END IF


IF (I.EQ.X) THEN
CCC(J)=CK(I,J)*(2*PHI(I-1,J)-PHI(I-2,J))/(DX**2)
CCC(J)=CCC(J)-PHI(I-1,J)*(PHI(I,J)-PHI(I-1,J))/(DX**3)
CCC(J)=CCC(J)-0.5*PHI(I-1,J)*(PHI(I-1,J)-PHI(I-2,J))/(DX**3
```

```
      CCC(J)=CCC(J)+0.5*PHI(I-2,J)*(PHI(I-1,J)-PHI(I-2,J))/(DX**3
)
      PHIX=(PHI(I,J)-PHI(I-1,J))/DX
      CCC(J)=CCC(J)-0.5*(PHIX**2)/DX

      PHIX=(PHI(I,J)-PHI(I-1,J))/DX
      IF (PHIX.LT.CK(I,J)) CCC(J)=PHI(I-1,J)
      ELSE
        END IF

      END DO

      RZZ=XLEN(I,Y)*(XLEN(I,Y)-1)
      IF (XLEN(I,Y).GE.0 .AND. XLEN(I,Y).LE.1) CCC(Y)=RZZ
      IF (XLEN(I,Y).LT.0 .OR. XLEN(I,Y).GT.1) CCC(Y)=0

      A=1
      CALL THOMAS (A, Y, BBB, DDD, AAA, CCC)
      DO J=1, Y
      PHI(I,J)=CCC(J)
      END DO


      SWP(I)=SWP(I)+1
      IF (SWP(I).GE.SWPLINE) GOTO 20
      GOTO 10

20    CONTINUE
      END DO

      CALL RESIDUAL (X,Y,CK,PHI,XLEN,DX,DY,IRES,JRES,RESMX)

        IF (RESMX.LT.ARES) GOTO 70

        IF (SWPROW.LT.SWPNO) THEN
        DO I=3,X
        SWP(I)=0
        END DO
      GOTO 30
        ELSE
        END IF

70    WRITE (2,*) SWPROW,RESMX
      CLOSE (UNIT=2)

      OPEN (UNIT=1, FILE="d:\usr\ewahba\x_2d5.dat")
      DO I=1, X
      WRITE(1,1000) (XLEN(I,J), J=1,Y)
```

```
      END DO
      CLOSE (UNIT=1)

      OPEN (UNIT=1, FILE="d:\usr\ewahba\y_2d5.dat")
      DO I=1, X
      WRITE(1,1000) (YLEN(I,J), J=1, Y)
      END DO
      CLOSE (UNIT=1)

      DO I=3, X
      DO J=1, Y
        UVEL(I,J)=(PHI(I,J)-PHI(I-1,J))/DX
        END DO
        END DO
      OPEN (UNIT=1, FILE="d:\usr\ewahba\uvel_2d5_first_order.dat"
)
      DO I=1, X
      WRITE(1,1000) (UVEL(I,J), J=1,Y)
      END DO
      CLOSE (UNIT=1)

      OPEN (UNIT=1, FILE="d:\usr\ewahba\u.dat")
      DO I=1, X
      DO J=1, Y
      WRITE(1,*) PHI(I,J)
      END DO
      END DO

1000  FORMAT (4000(1X,E20.8))

      END PROGRAM


      SUBROUTINE RESIDUAL (X,Y,CK,PHI,XLEN,DX,DY,IRES,JRES,RESMX)
      IMPLICIT NONE
      INTEGER :: I,J,X,Y,IRES,JRES
        DOUBLE PRECISION,DIMENSION(350,200) :: PHI,CK,RES
        REAL,DIMENSION(350,200) :: XLEN
      DOUBLE PRECISION :: DX,DY,F1,F2,F3,PHIX,PHIYY,RESMX

      RESMX=0
      DO I=3,X
      RES(I,1)=(PHI(I,2)-PHI(I,1))/DY
      PHIX=(PHI(I,1)-PHI(I-1,1))/DX
      IF (I.EQ.X .AND. PHIX.LT.CK(I,1)) RES(I,1)=PHIX
      RES(I,1)=ABS(RES(I,1))
      IF (RES(I,1).GT.RESMX) IRES=I
      IF (RES(I,1).GT.RESMX) JRES=1
```

```
IF (RES(I,1).GT.RESMX) RESMX=RES(I,1)

DO J=2, Y-1
PHIX=(PHI(I,J)-PHI(I-1,J))/DX
IF (I.EQ.X .AND. PHIX.LT.CK(I,J)) THEN
RES(I,J)=(PHI(I,J)-PHI(I-1,J))/DX
GOTO 100
ELSE
END IF

PHIX=(PHI(I+1,J)-PHI(I,J))/DX
F1=PHIX*(CK(I,J)-0.5*PHIX)
PHIX=(PHI(I,J)-PHI(I-1,J))/DX
F2=PHIX*(CK(I,J)-0.5*PHIX)
PHIYY=(PHI(I,J+1)-2*PHI(I,J)+PHI(I,J-1))/(DY**2)
RES(I,J)=(F1-F2)/DX+PHIYY

PHIX=(PHI(I,J)-PHI(I-1,J))/DX
F2=PHIX*(CK(I,J)-0.5*PHIX)
IF (PHIX.GE.CK(I,J)) THEN
RES(I,J)=RES(I,J)+2*F2/DX
ELSE
RES(I,J)=RES(I,J)+(CK(I,J)**2)/DX
END IF

PHIX=(PHI(I+1,J)-PHI(I,J))/DX
F1=PHIX*(CK(I,J)-0.5*PHIX)
IF (PHIX.GE.CK(I,J)) THEN
RES(I,J)=RES(I,J)-F1/DX
ELSE
RES(I,J)=RES(I,J)-0.5*(CK(I,J)**2)/DX
END IF

PHIX=(PHI(I-1,J)-PHI(I-2,J))/DX
F3=CK(I,J)*PHIX-0.5*(PHIX**2)
IF (PHIX.GE.CK(I,J)) THEN
RES(I,J)=RES(I,J)-F3/DX
ELSE
RES(I,J)=RES(I,J)-0.5*(CK(I,J)**2)/DX
END IF

IF (I.EQ.X) THEN
PHIX=(PHI(I,J)-PHI(I-1,J))/DX
F2=PHIX*(CK(I,J)-0.5*PHIX)
PHIX=(PHI(I-1,J)-PHI(I-2,J))/DX
F3=CK(I,J)*PHIX-0.5*(PHIX**2)
PHIYY=(PHI(I,J+1)-2*PHI(I,J)+PHI(I,J-1))/(DY**2)
RES(I,J)=(F2-F3)/DX+PHIYY
```

```
        ELSE
        END IF


100     RES(I,J)=ABS(RES(I,J))
        IF (RES(I,J).GT.RESMX) IRES=I
        IF (RES(I,J).GT.RESMX) JRES=J
        IF (RES(I,J).GT.RESMX) RESMX=RES(I,J)
        END DO

        IF (XLEN(I,Y).GE.0 .AND. XLEN(I,Y).LE.1) THEN
        RES(I,Y)=PHI(I,Y)-XLEN(I,Y)*(XLEN(I,Y)-1)
        ELSE
        RES(I,Y)=PHI(I,Y)
        END IF
        RES(I,Y)=ABS(RES(I,Y))
        IF (RES(I,Y).GT.RESMX) IRES=I
        IF (RES(I,Y).GT.RESMX) JRES=Y
        IF (RES(I,Y).GT.RESMX) RESMX=RES(I,Y)

        END DO
        RETURN
          END SUBROUTINE
```